



SAPIENZA
UNIVERSITÀ DI ROMA

Experimental Investigation on Fluid Mechanics of Different Micro Heat Transfer Devices

Year 2019/2020

XXXII PhD Course of

Theoretical and Applied Mechanics

Supervisor: Prof. Giovanni Paolo Romano

PhD student: Michela Spizzichino

Summary

Summary	2
Index of Figures	3
Index of Tables	7
Abstract	8
Chapter 1 - Introduction and Problem Statement	9
Chapter 2 - Background and definitions	16
2.1 Friction factor and micro-cell efficiency	24
2.2 Entropy analysis	26
Chapter 3 - Materials and experimental methods	28
3.1 Micro Devices	29
3.1.1 Straight channel micro-cell.....	33
3.1.2 Straight parallel channels micro-cell type-I.....	34
3.1.3 Straight parallel channels micro-cell type-II.....	37
3.1.4 Standard serpentine micro-cell	39
3.1.5 Wavy-sinusoidal serpentine micro-cell	42
3.2 Syringe Pump	44
3.2.1 Flow rate studied	45
3.3 Hot Plate.....	47
3.4 Infrared Thermometer	49
3.5 Thermocouples Reader	50
3.6 Tracer	51
3.7 Fast-Cam.....	52
3.8 Pressure Sensor	55
3.9 Determination of Reynolds number.....	55
3.10 Determination of Nusselt number.....	59
Chapter 4 - Results: Thermal Measurements.....	64
4.1 Temperature experimental data	65
4.2 Temperature extrapolated data.....	71
4.3 Thermal measurements results.....	75
4.4 Error analysis results	81
Chapter 5 – Fanning Friction Factors and Efficiencies	85
5.1 Efficiency parameter	91
Chapter 6 - μ PIV Results	94
6.1 Configurations selection for analysis.....	95
6.2 Mean velocity vectors and magnitude fields.....	98

6.3	Mean Standard deviation and vorticity fields	102
6.4	Mean velocity vectors, magnitude and vorticity fields at 90 ml/min	108
6.5	Vertical Profiles of standard serpentine cells	111
6.6	Mean Entropy fields	114
Chapter 7 – Conclusions		118
Appendix		121
A.1	Interpolation and extrapolation method	121
A.2	Error analysis: Reynolds and Nusselt numbers	124
A.3	Particle Image Velocimetry analysis and post-processing	127
A.4	Measured temperatures of outlet fluid and wall	131
A.5	Extrapolated temperatures of outlet fluid and wall	134
A.6	Prandtl Number	137
A.7	Efficiency parameters	140
Acknowledgements		144
References		145

Index of Figures

<i>Figure 1: Interferograms of square ducts with radii at the corners, Compact Heat Exchangers, F.Mayingier, J. Klas (1993) [7].</i>	10
<i>Figure 2: Example of corrugated walls (a), cylindrical ribs (b) and channel side grooving (c); [8], [9], [10].</i>	10
<i>Figure 3: Development of a micro-heat exchanger with stacked plates using LTCC technology, E. Vásquez-Alvarez, F. T. Degasperi, L. G. Morita, M. R. Gongora-Rubio, R. Giudici (2010) [11].</i>	11
<i>Figure 4: Micro-PIV visualization and numerical simulation of flow and heat transfer in three micro pin-fin heat sinks, G. Xia, Z. Chen, L. Cheng, D. Ma, Y. Zhai, Y. Yang (2017) [16].</i>	13
<i>Figure 5: Hydrodynamic and thermal boundary layers for flow over a heated flat plate - Engineering Thermofluids - M. Massoud [2].</i>	19
<i>Figure 6: Example of comparison of the Average Nusselt numbers as a function of the Reynolds number obtained for three tested micro-cells at 50 °C.</i>	23
<i>Figure 7: Sketch of the experimental setup.</i>	28
<i>Figure 8: Geometrical configurations studied.</i>	30
<i>Figure 9: Example of a sealing frame manufactured on the straight parallel channels cell type-I.</i>	31
<i>Figure 10: Straight channel cell with aluminum gap-pad.</i>	31
<i>Figure 11: Inlet and exit tubes.</i>	32
<i>Figure 12: Top view and CAD drawing of the straight channel micro-cell.</i>	33
<i>Figure 13: View of the aluminum bottom side and CAD drawing of the thermocouples venues.</i>	34
<i>Figure 14: Top view and CAD drawing of the straight parallel channels micro-cell type-I.</i>	36
<i>Figure 15: Fluid guide profiles and the placement scheme with flow rate percentages.</i>	36
<i>Figure 16: Top view of the aluminum straight parallel channels micro-cell type-I.</i>	37
<i>Figure 17: Top view and CAD drawing of the straight parallel channels micro-cell type-II.</i>	38
<i>Figure 18: View of the aluminum bottom side and CAD drawing of the thermocouples venues.</i>	39

Figure 19: Top view and CAD drawing of the standard serpentine cell.	40
Figure 20: View of the aluminum bottom side and CAD drawing of the thermocouples venues.	41
Figure 21: Standard serpentine micro-cell with ribs. (a) Top view of the test section; (b) View in the cross-section with rib.	42
Figure 22: Top view and CAD drawing of the wavy-sinusoidal serpentine.	43
Figure 23: Hll Landgraf LA-800 Syringe Pump.	44
Figure 24: Modified 140 ml aluminum syringe. Lateral view (left image) and front view (right image).	45
Figure 25: Hot plate Stuart US-150.	48
Figure 26: Infrared thermometer PCE 779N.	49
Figure 27: K, J, E, T, N and R-type thermocouple reader SE521.	50
Figure 28: Sample of hollow glass spherical particles.	52
Figure 29: Fast-cam Mini AX100 and Nikon objectives.	53
Figure 30: Flowplus16-ViscoTec pressure sensor, on the left. Elveflow OB1-MK3, on the right.	55
Figure 31: Water temperatures as a function of time [s] and flow rate [ml/min] for the standard serpentine cell at 50 °C.	66
Figure 32: Wall temperatures as a function of time [s] and flow rate [ml/min] for the standard serpentine cell at 50 °C.	66
Figure 33: Water temperatures as a function of time [s] and flow rate [ml/min] for the standard serpentine cell at 70 °C.	67
Figure 34: Wall temperatures as a function of time [s] and flow rate [ml/min] for the standard serpentine cell at 70 °C.	67
Figure 35: Water temperatures as a function of time [s] and flow rate [ml/min] for the straight channel cell at 50 °C.	69
Figure 36: Outlet water temperatures as a function of flow rate [ml/min] for the parallel channels cell realized in plexiglass and aluminum at 50 °C.	70
Figure 37: Extrapolated water temperatures as a function of time [s] and flow rate [ml/min] for the standard serpentine cell at 50 °C.	71
Figure 38: Extrapolated wall temperatures as a function of time [s] and flow rate [ml/min] for the standard serpentine cell at 50 °C.	72
Figure 39: Extrapolated water temperatures as a function of time [s] and flow rate [ml/min] for the standard serpentine cell at 70 °C.	72
Figure 40: Extrapolated wall temperatures as a function of time [s] and flow rate [ml/min] for the standard serpentine cell at 70 °C.	73
Figure 41: New extrapolation of wall temperatures as a function of time [s] and flow rate [ml/min] for the standard serpentine cell at 50 °C.	75
Figure 42: Comparison of the Average Nusselt numbers as a function of the Reynolds number obtained for straight channel cell at 50 °C with the results proposed by Lee and Garimella [41], [42].	76
Figure 43: Comparison of the Average Nusselt numbers as a function of the Reynolds number obtained for the three tested micro-cells at 50 °C with the classical correlation proposed by Sieder & Tate [39].	77
Figure 44: Comparison of the Average Nusselt numbers as a function of the Reynolds number obtained for the three tested micro-cells at 70 °C with the classical correlation proposed by Sieder & Tate [39].	77
Figure 45: Comparison of the Average Nusselt numbers as a function of the Reynolds number obtained for the four tested micro-cells at 50 °C with the classical correlation proposed by Sieder & Tate [39].	79
Figure 46: Comparison of the Average Nusselt numbers as a function of the Reynolds number obtained for the four tested micro-cells at 70 °C with the classical correlation proposed by Sieder & Tate [39].	80
Figure 47: Error on Nusselt number (ΔNu) as a function of Reynolds number for all micro-cells at 50 °C.	82
Figure 48: Error on Nusselt number (ΔNu) as a function of Reynolds number for all micro-cells at 70 °C.	83
Figure 49: Relative pressure-drop as a function of flow rate [ml/min] for the tested micro-channels.	86

Figure 50: Fanning friction factor as a function of Reynolds number for the tested micro-channels at 70 °C: parallel channels, standard serpentine with and without ribs, wavy-sinusoidal serpentine, with the classical correlation proposed by J.T. Fanning [46].	87
Figure 51: Fanning friction factor as a function of Reynolds number for the tested micro-channels at 70 °C: standard serpentine tested with water and water-glycerin solutions, with the classical correlation proposed by J.T. Fanning [46].	88
Figure 52: Comparison of the efficiency parameters as a function of Reynolds number for the three tested micro-cells at 50 °C.	91
Figure 53: Comparison of the efficiency parameters as a function of Reynolds number for the three tested micro-cells at 70 °C.	91
Figure 54: Flow distribution in the parallel channels cell type-I vs parallel channels cell type-II (inner and outer sections of the six first channels, figure 55).	96
Figure 55: Flow rate of 30 ml/min. Acquisition areas delimited in blue with main technical features (left column) and picture (right column) of the top view of the micro-cells. A) straight parallel channels type-II, B) standard serpentine, C) wavy-synusoidal serpentine. In red the area whose technical details are shown in the lower left panel.	97
Figure 56: Flow rate of 90 ml/min. Acquisition areas delimited in blue with main technical features (left column) and picture (right column) of the top view of the micro-cells. A) straight parallel channels type-II, B) standard serpentine, C) wavy-synusoidal serpentine. In red the area whose technical details are shown in the lower left panel.	98
Figure 57: Mean velocity vectors fields at 30 ml/min. (a) straight parallel channels, (b) standard serpentine, (c) wavy serpentine, d) std. serpentine with 70 % water & 30 % glycerin, e) std. serpentine with 30 % water & 70 % glycerin.	100
Figure 58: Mean velocity magnitude color maps at 30 ml/min. (a) straight parallel channels, (b) standard serpentine, (c) wavy serpentine, d) std. serpentine with 70 % water & 30 % glycerin, e) std. serpentine with 30 % water & 70 % glycerin.	101
Figure 59: Standard Deviation of u component at 30 ml/min. a) straight parallel channels type-II, b) standard serpentine, c) wavy-synusoidal serpentine, d) std. serpentine with 70 % water & 30 % glycerin, e) std. serpentine with 30 % water & 70 % glycerin.	103
Figure 60: Standard Deviation of v component at 30 ml/min. a) straight parallel channels type-II, b) standard serpentine, c) wavy-synusoidal serpentine, d) std. serpentine with 70 % water & 30 % glycerin, e) std. serpentine with 30 % water & 70 % glycerin.	104
Figure 61: Standard Deviation of u component at 90 ml/min. a) straight parallel channels type-II, b) standard serpentine, c) wavy-synusoidal serpentine, d) std. serpentine with 70 % water & 30 % glycerin, e) std. serpentine with 30 % water & 70 % glycerin.	105
Figure 62: Standard Deviation of v component at 90 ml/min. a) straight parallel channels type-II, b) standard serpentine, c) wavy-synusoidal serpentine, d) std. serpentine with 70 % water & 30 % glycerin, e) std. serpentine with 30 % water & 70 % glycerin.	106
Figure 63: Mean vorticity color maps at 30 ml/min. (a) straight parallel channels, (b) standard serpentine, (c) wavy serpentine, d) std. serpentine with 70 % water & 30 % glycerin, e) std. serpentine with 30 % water & 70 % glycerin.	107
Figure 64: Mean velocity vectors fields at 90 ml/min. (a) straight parallel channels, (b) standard serpentine, (c) wavy serpentine, d) std. serpentine with 70 % water & 30 % glycerin, e) std. serpentine with 30 % water & 70 % glycerin.	109
Figure 65: Mean velocity magnitude color maps at 90 ml/min. (a) straight parallel channels, (b) standard serpentine, (c) wavy serpentine, d) std. serpentine with 70 % water & 30 % glycerin, e) std. serpentine with 30 % water & 70 % glycerin.	110

Figure 66: Mean vorticity color maps at 90 ml/min. (a) straight parallel channels, (b) standard serpentine, (c) wavy serpentine, d) std. serpentine with 70 % water & 30 % glycerin, e) std. serpentine with 30 % water & 70 % glycerin.	111
Figure 67: Standard serpentine geometry. Sections for the analysis of vertical profiles.	112
Figure 68: Comparison of vertical profiles extracted at position 1. Std. serpentine tested with water (red curve), std. serpentine tested with 70 % water and 30 % glycerin (blue curve) and std. serpentine tested with 30 % water and 70 % glycerin.	112
Figure 69: Comparison of vertical profiles extracted at position 2. Std. serpentine tested with water (red curve), std. serpentine tested with 70 % water and 30 % glycerin (blue curve) and std. serpentine tested with 30 % water and 70 % glycerin.	113
Figure 70: Comparison of vertical profiles extracted at position 3. Std. serpentine tested with water (red curve), std. serpentine tested with 70 % water and 30 % glycerin (blue curve) and std. serpentine tested with 30 % water and 70 % glycerin.	113
Figure 71: Mean entropy fields at 30 ml/min. (a) straight parallel channels, (b) standard serpentine, (c) wavy serpentine, d) std. serpentine with 70 % water & 30 % glycerin, e) std. serpentine with 30 % water & 70 % glycerin.	115
Figure 72: Mean entropy fields at 90 ml/min. (a) straight parallel channels, (b) standard serpentine, (c) wavy serpentine, d) std. serpentine with 70 % water & 30 % glycerin, e) std. serpentine with 30 % water & 70 % glycerin.	116
Figure 73: Wavy-sinusoidal serpentine cell, before (left) and after (right) the minimum subtraction.	127
Figure 74: Wavy-sinusoidal serpentine cell raw image (top left), application of the exclusion mask (red area) with evidence of analysis windows (top right), instantaneous velocity vector fields (lower center).	128
Figure 75: Comparison of the average Nusselt numbers as a function of the Prandtl number obtained for the four micro-cells tested with water together with the reference law for a laminar flow over a flat isothermal plate [2]. Hot source temperature equal to 50 °C.	1287
Figure 76: Comparison of the average Nusselt numbers as a function of the Prandtl number obtained for the two micro-cells tested with water/glycerin solutions together with the reference law for a laminar flow over a flat isothermal plate [2]. Hot source temperature equal to 50 °C.	1288
Figure 77: Comparison of the average Nusselt numbers as a function of the Prandtl number obtained for the four micro-cells tested with water together with the reference law for a laminar flow over a flat isothermal plate [2]. Hot source temperature equal to 70 °C.	1288
Figure 78: Comparison of the average Nusselt numbers as a function of the Prandtl number obtained for the two micro-cells tested with water/glycerin solutions together with the reference law for a laminar flow over a flat isothermal plate [2]. Hot source temperature equal to 70 °C.	139
Figure 79: Comparison of the efficiency parameters ϵ' as a function of Reynolds number for the tested cells at 50 °C.	141
Figure 80: Comparison of the efficiency parameters ϵ'' as a function of Reynolds number for the tested cells at 50 °C.	142
Figure 81: Comparison of the efficiency parameters ϵ' as a function of Reynolds number for the tested cells at 70 °C.	142
Figure 82: Comparison of the efficiency parameters ϵ'' as a function of Reynolds number for the tested cells at 70 °C.	143

Index of Tables

Table 1: D_h , L and D_h/L values for each micro-cell .	25
Table 2: Conversion factors from pixel to meter and from frame to second.	27
Table 3: Main features of the straight channel micro-cell.	33
Table 4: Main features of the straight parallel channels micro-cell type-I.	35
Table 5: Main features of the straight parallel channels micro-cell type-I.	38
Table 6: Main features of the standard serpentine cell.	40
Table 7: Main features of the wavy-sinusoidal serpentine cell.	43
Table 8: Listing of flow rates, Reynolds numbers and speed values analyzed for each micro-cell.	46
Table 9: Amount of values recorded as a function of flow rate starting by a fixed volume of 140 ml.	51
Table 10: Micro-cell type with indication of the correct dosage of tracer in grams.	52
Table 11: Summary of the set conditions.	54
Table 12: Reynolds number parameters. Cooling fluid: distilled water.	56
Table 13: Reynolds numbers and bulk velocity values. Cooling fluid: distilled water.	57
Table 14: Reynolds number parameters. Solution with 30 % glycerin & 70 % water.	58
Table 15: Reynolds number parameters. Solution with 70 % glycerin & 30 % water.	58
Table 16: Reynolds numbers and bulk velocity values obtained for the two tested solutions.	58
Table 17: Geometrical parameters of the tested micro-cells.	60
Table 18: Mass flow rate values corresponding to set flow rates for each working fluid.	61
Table 19: Glycerin and Ethylene glycol properties table.	63
Table 20: Geometrical parameters of the tested micro-cells.	88
Table 21: Bulk Velocities, Reynolds numbers and Fanning factors at 70 °C.	90
Table 22: Measurement time vs extrapolation time.	122
Table 23: PIVlab processing and vector validation times for different configurations.	129
Table 24: Final measured temperatures of outlet fluid for each flow rate [ml/min] and configuration at 50 °C.	131
Table 25: Final measured temperatures of wall for each flow rate [ml/min] and configuration at 50 °C.	132
Table 26: Final measured temperatures of outlet fluid for each flow rate [ml/min] and configuration at 70 °C.	132
Table 27: Final measured temperatures of wall for each flow rate [ml/min] and configuration at 70 °C.	133
Table 28: Final extrapolated temperatures of outlet fluid for each flow rate [ml/min] and configuration at 50 °C, with indication in red of anomalous values provided by analytical model.	134
Table 29: Final extrapolated temperatures of wall for each flow rate [ml/min] and configuration at 50 °C, with indication in red of anomalous values provided by analytical model.	135
Table 30: Final extrapolated temperatures of outlet fluid for each flow rate [ml/min] and configuration at 70 °C, with indication in red of anomalous values provided by analytical model.	135
Table 31: Final extrapolated temperatures of wall for each flow rate [ml/min] and configuration at 70 °C, with indication in red of anomalous values provided by analytical model.	136

Abstract

The future technological horizons for engineering applications (Automotive, Energy, Bio-engineering) will require the use of small size heat exchangers with high heat exchange efficiency. In the present work, the thermo-hydrodynamic behaviour of eight different micro-heat exchangers is investigated experimentally using thermal measurements and μ PIV (micro Particle Image Velocimetry), in order to detail and improve the thermal performance of micro-devices. To test the heat transfer properties and the detailed fluid flow behaviour, this research was extended from typical range of *Reynolds number* in the laminar regime, from 50 to 1500, to the turbulent regime with *Reynolds number* up to 4000. Moreover, different cooling fluids are employed to analyse the heat transfer capability of micro-devices under different working conditions. Results are evaluated first in term of the *Nusselt-Reynolds* diagram and then through the efficiency of the cells performed by relating the average *Nusselt number* to the *Fanning factor*. On the base of the thermal analysis, the μ PIV measurements were employed to detail the observed global heat exchange performances of each micro-cell configuration. In order to make a link with results highlighted by the thermal measurements the attention was focused on local fluid recirculation and acceleration as related to the specific geometry and to the different flow rates. The main result of this investigation is that the standard serpentine micro cell attains the highest efficiency regardless of flow regime, getting high *Nusselt numbers* combined with low pressure losses, as derived by the observation of quite high local velocities and few recirculation regions. In fact, PIV results highlighted that the main reason for the increasing *Nusselt number* is only dependent on local high intensity accelerations and not on recirculation regions, that appear to contribute only to pressure loss increments. Also in case of working fluids with high glycerin contents, *e.g.* 30 % water and 70 % glycerin, the results suggested high thermal exchange properties, mainly related to the glycerin physical properties and not only to local high intensity fluid accelerations.

Chapter 1 - Introduction and Problem Statement

The use of high efficiency heat exchangers is the basis of several technological developments required in different engineering applications, *e.g.* automotive, energy and bioengineering [1]. Since the heat transfer coefficient is inversely proportional to the characteristic dimension of the system, $h = \frac{\dot{Q}_{conv}}{A \cdot \Delta T} \left[\frac{W}{m^2 \cdot K} \right]$ [2], a valid solution to optimize the cooling process is to use a system of multiple micro heat exchangers instead of a single macro counterpart. Until now, the main features usually investigated to enhance the heat transfer efficiency of micro-devices are related to the materials of the microchannel, the channel geometry, the cooling fluid and the flow regime ([3],[4]). To this aim, the heat transfer performances of a small-device are commonly assessed by the ratio between the heat transfer rate, usually expressed in terms of the average *Nusselt number*, based on the difference between inlet and outlet temperature of the working fluid, and the pressure losses induced by the geometry, which can be directly measured or analytically determined on the base of boundary conditions [5] (in section 2 exact definitions are given).

From the 90s up to today, several studies have been carried out to optimize the channel geometry and the flow regime ([6],[7],[8],[9]). In particular, heat exchangers with channels having a serpentine shape have received considerable attention given the high heat transfer properties and the compactness requirement typical of such micro-devices. The first work introducing a periodical deflection of the flow in a meandering arrangement of a straight channel is due to Asako *et al.* (1988) [6]. The use of such a meandering micro-channel, of which an example is given in Figure 1, leads to an increase of heat transfer in comparison to the straight channel of 77 % for a *Reynolds number* (*Re*) around 1000. This is related to enhancements of local turbulence levels in meanders, at the cost of a large increase in pressure drop, *i.e.* around 95 %.

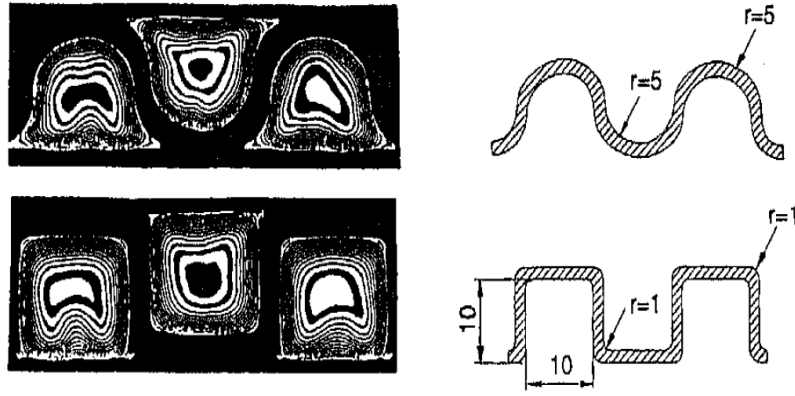


Figure 1: Interferograms of square ducts with radii at the corners, *Compact Heat Exchangers*, F. Mayinger, J. Klas (1993) [7].

From this first study, it was clear how transition to turbulent regime increases the thermal diffusion from a molecular to a macroscopic level. As a consequence, other studies have increasingly focused on the research of new geometrical solutions to promote turbulence motions within straight channels. The main proposals concern corrugated walls [8], channel side grooving [9] and cylindrical ribs fixed in a staggered or in line arrangements [10]. However, all these solutions, while promoting large deflections and velocity changes in the fluid flow, were characterized by moderate increase in the average *Nusselt number* compared with a large increase in pressure drop.

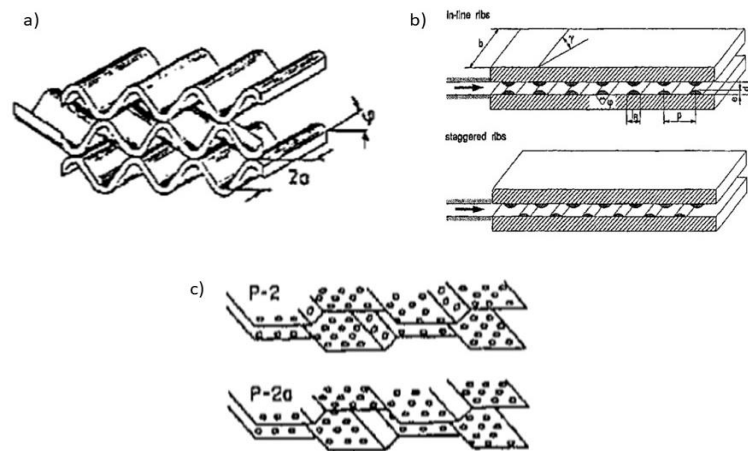


Figure 2: Example of corrugated walls (a), cylindrical ribs (b) and channel side grooving (c); [8], [9], [10].

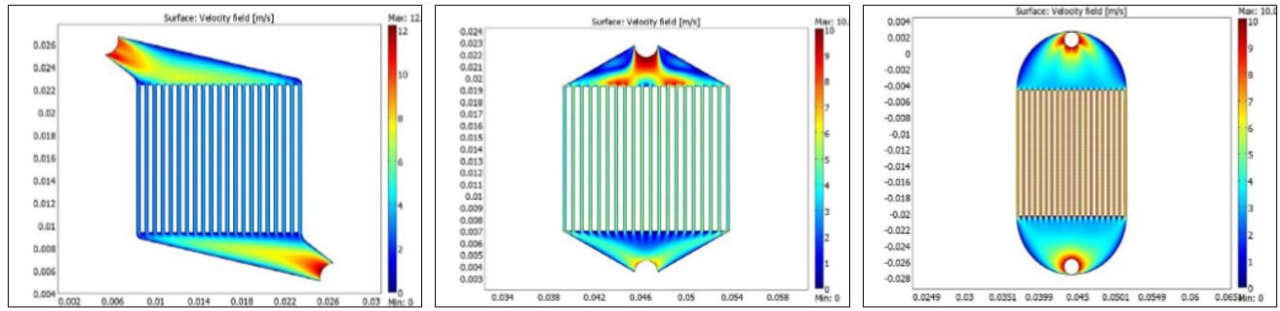


Figure 3: Development of a micro-heat exchanger with stacked plates using LTCC technology, E. Vásquez-Alvarez, F. T. Degasper, L. G. Morita, M. R. Gongora-Rubio, R. Giudici (2010) [11].

Then, starting from the 2000s, geometries have been designed to obtain high increases in *Nusselt number* by keeping low pressure losses. Specifically, different studies focused on Parallel channels micro-cells and U-shaped serpentine micro-channels, both characterized by very low pressure losses. With regard the parallel channels cells, despite a geometry that guarantees very low pressure losses and a high heat exchange surface, this configuration has the great disadvantage of having a non-homogeneous flow distribution inside the channels, which considerably reduces its heat exchange performance, as shown in the work of E. Vásquez-Alvarez *et al.* (2010) [11]. In this experimental work, different geometries of the inlet and outlet sections have been proposed to show how geometric details directly affect the distribution of velocity in the micro-heat exchanger channels (Figure 3). However, even if some proposals has presented improvements, none lead to a homogeneous distribution, so far showing high coefficients heat exchange only in correspondence of the central channels. More complex are the heat transfer properties observed for the U-shaped serpentine micro-channels, as in Rosaguti *et al.* (2005) [12]. In this study a detailed analysis of convective heat transfer phenomena was carried out for *Reynolds numbers* up to 200 and Dean vortices were observed in the bending regions of the U-shaped sections, as expected to occur when the working fluid flows along curved pipes or channels [13]. The centripetal forces at bend sections cause a pressure and velocity gradient imbalance, with a consequent generation of vortices and secondary flows

(Dean instability), superposed on the primary flow, thus providing high fluid mixing and improvements in the heat transfer process. Despite the good thermal properties attainable by the U-shaped serpentine micro-channels, Al-Neama *et al.* (2017) [5] proposed an experimental and numerical work showing how this configuration, as also more complicated options, are affected by a high temperature gradient, between the inlet and the outlet of the fluid flow, leading to a consequent large inhomogeneity in the heat exchange process. Indeed, Sui *et al.*, already in 2011 [14], pointed out this problem and proposed a solution through an experimental investigation of three sinusoidal micro-channels with rectangular cross sections and different wavy amplitudes. More in detail, their experimental study revealed that under laminar flow regime ($300 < Re < 800$), in a straight channel or section, as for example in the standard serpentine microchannel, the heat transfer performances deteriorate along the flow direction because the flow becomes more regular and the boundary layers thicken, so that temperature gradients become increasingly small. However, by inserting periodic curvilinear sections, the generated secondary flows enhance fluid mixing, thus decreasing the temperature gradient between inlet and outlet. Based on these preliminary results, great interest has been given again to the study of wavy-sinusoidal configuration but with some differences compared to first studies. In particular, Lin *et al.* (2017) [15] improved the heat transfer properties through the design of a wavy microchannel with changing wavelength and amplitude along the flow direction. From the comparison between the new and the standard wavy-sinusoidal configuration, it is possible to notice a considerable increase in heat transfer and a lower inhomogeneity in the thermal field, due to the formation of vortices of different size in the channel cross sections. However, even with such a considerable improvement of the wavy-sinusoidal configuration performances, *i.e.* efficiency given by ratio between heat transfer rate and pressure losses around 52 % at $Re = 800$ [13], the efficiency is not yet comparable with that of the serpentine configuration, around 71 % at the same *Reynolds number* [5].

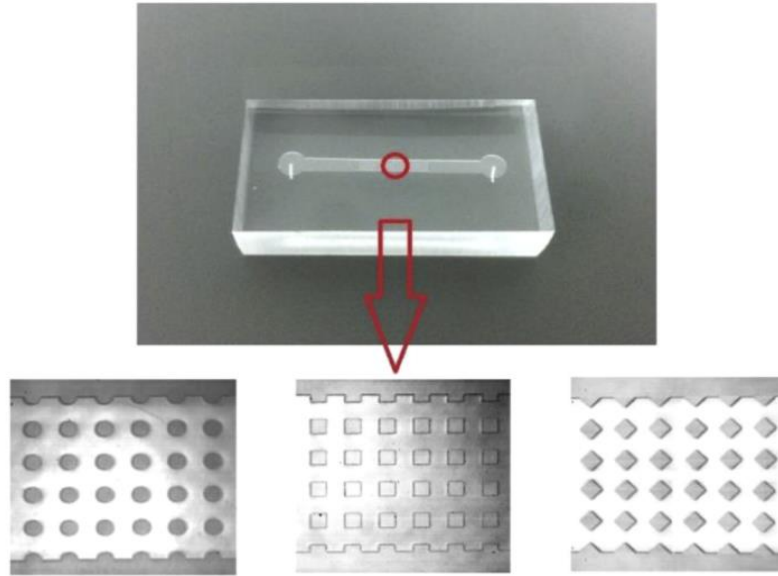


Figure 4: Micro-PIV visualization and numerical simulation of flow and heat transfer in three micro pin-fin heat sinks, G. Xia, Z. Chen, L. Cheng, D. Ma, Y. Zhai, Y. Yang (2017) [16].

For this reason, in last years, studies have been conducted for solutions to increase the micro-cells heat exchange properties, *e.g.* by acting on surface and fluid mixing rate, at the expense of a moderately high pressure drop. G. Xia *et al.* [16] proposed an interesting work concerning the insertion of micro pin-fin on the bottom of the micro-channel (Figure 4) and the evaluation of the best shape (circular, square and diamond shape) to increase the heat transfer and contain pressure losses due to formation of vortical structures behind the fins. Lastly, in recent time, also investigations on micro-channels with flow at considerably higher *Reynolds number* have been carried out. Among several works, Hao and Chen (2014) [17] investigated the heat transfer and pressure drop in eight serpentine aluminum channels of different widths (from 2 mm to 3.8 mm) and fixed height, covered with an adiabatic plate, for *Reynolds numbers* equal to 500, 1000 and 1500. For all investigated configurations, the turbulent regime led to a significant increase in heat exchange, even if with higher pressure losses compared with the laminar one, thus suggesting that the increase of *Reynolds number* and the transition to turbulence could be

another interesting solution to increase efficiency of micro heat exchangers, in addition to changes in geometry.

From the above mentioned literature, it is evident the importance of experimental investigations on new geometrical solutions, combining main results in terms of geometry, pressure losses and heat transfer behaviour of the U-shaped and wavy-sinusoidal serpentine channels, straight parallel micro-channels and micro pin-fin elements. Hence, in the present work, the thermo-hydrodynamic behaviour of different micro-channels is investigated: a straight parallel channels configuration with two novel proposals of the inlet and outlet geometry, a conventional serpentine path, a new wavy-sinusoidal serpentine path and a U-shaped channel with aluminium horizontal ribs. Also the classical straight channel configuration is investigated to validate the measurement system. All configurations are tested with distilled water except for the conventional serpentine in which a solution with two different percentages of glycerin and water, *i.e.* 70 % glycerin and 30 % water; 30 % glycerin and 70 % water is also implemented. Results are evaluated in terms of efficiency of the cell and compared with the classical straight parallel channels micro-cell, to be considered as a reference. In addition, to test the heat transfer properties and the detailed fluid flow behaviour, this research was extended from typical range of *Reynolds numbers* in the laminar regime, from 50 to 1500, up to *Reynolds number* of 4000, *i.e.* in the turbulent regime. The aim of the present work is to explore and compare the thermal performance of conventional and novel micro-channel geometries. The heat exchange capability is evaluated on the base of the *Nusselt-Reynolds* diagram, whereas efficiency is evaluated by means of the average *Nusselt numbers* compared to the *Fanning friction factors* obtained for each flow rates. Heat transfer properties are also supported by detailed velocity fields measured within the channels performed by particle image velocimetry (μ PIV). Moreover, the innovative choice to assemble micro-channels in an adiabatic material is developed in view of an easy

implementation of micro heat exchangers on existing engineering applications. To assess the influence of the channel material on the heat exchange rate, a comparison between the straight parallel channels micro-cell assembled in an adiabatic material and assembled in a conductive material was carried out.

Chapter 2 - Background and definitions

In the law of conservation of energy for incompressible flow (constant density ρ), obtained subtracting the conservation equation of momentum from the conservation equation of energy in its general form, three different type of heat transfer appear, as well as the terms related to effect of internal and external forces applied on a fixed control volume:

$$\rho \left(\frac{\partial U}{\partial t} + \vec{v} \cdot \vec{\nabla} U \right) = \rho \frac{DU}{Dt} = -\vec{\nabla} \cdot \vec{q}_{cond}^{II} - \vec{\nabla} \cdot \vec{q}_r^{II} + q^{III} + \varphi \quad (1)$$

where:

$\rho \frac{\partial U}{\partial t}$: local rate of change of the internal energy.

$\rho \vec{v} \cdot \vec{\nabla} U$: rate of heat transfer due to convection.

$-\vec{\nabla} \cdot \vec{q}_{cond}^{II}$: net rate of heat transfer due to conduction.

$-\vec{\nabla} \cdot \vec{q}_r^{II}$: net rate of heat transfer due to radiation.

q^{III} : rate of volumetric heat generation.

$\varphi = 2 \frac{\partial \mu}{\partial T} \left[\left(\frac{\partial v_x}{\partial x} \right)^2 + \left(\frac{\partial v_y}{\partial y} \right)^2 + \left(\frac{\partial v_z}{\partial z} \right)^2 \right] + \frac{\partial \mu}{\partial T} \left[\left(\frac{\partial v_y}{\partial x} + \frac{\partial v_x}{\partial y} \right)^2 + \left(\frac{\partial v_z}{\partial y} + \frac{\partial v_y}{\partial z} \right)^2 + \left(\frac{\partial v_x}{\partial z} + \frac{\partial v_z}{\partial x} \right)^2 \right]$: rate of work performed by viscous forces.

For system characterized by medium-low temperatures (for example in our case the max temperature is 70 °C) the net rate of heat transfer due to radiation can be neglected because there aren't relevant radiation phenomena. To define the net rate of heat transfer due to conduction the Fourier's law is applied:

$$\vec{q}_{cond}^{II} = -k_{fluid} \cdot \nabla T \quad \left[\frac{W}{m^2} \right] \quad (2)$$

where $k_{fluid} \left[\frac{W}{m \cdot K} \right]$ is the fluid thermal conductivity and $\nabla T \left[\frac{K}{m} \right]$ is the temperature gradient. By substituting the definition of conductive heat transfer, the law of conservation of energy becomes:

$$\rho \left(\frac{\partial U}{\partial t} + \vec{v} \cdot \vec{\nabla} U \right) = \rho \frac{DU}{Dt} = \vec{\nabla} \cdot (k \vec{\nabla} T) + q''' + \varphi \quad (3)$$

From the energy balance is possible to derive the governing equation of conduction heat transfer under conditions of inviscid fluid ($\varphi = 0$) and solid bodies or stagnant fluids ($\vec{v} = 0$).

$$\rho c_p \frac{\partial T}{\partial t} = \vec{\nabla} \cdot (k \vec{\nabla} T) + q''' \quad (4)$$

Convection is transferring energy between a solid surface and the adjacent liquid or gas that is in motion, involving the combined effects of conduction and fluid motion. So, starting by the governing equation of conduction heat transfer and introducing the substantial derivative to take into account fluid motion, it is possible to derive the governing equation of convection heat transfer:

$$\rho c_p \frac{DT}{Dt} = \vec{\nabla} \cdot (k \vec{\nabla} T) + q''' \quad (5)$$

By dimensional analysis is possible to derive its dimensionless expression function of *Reynolds number* (Re), *Prandtl number* (Pr) and *Brinkman number* (Br) define as:

$$Re = \frac{\rho \cdot v \cdot L}{\mu} = \frac{v \cdot L}{\nu} \quad (6)$$

$$Pr = \frac{\mu \cdot c_p}{k_{fluid}} \quad (7)$$

$$Br = \frac{\mu \cdot v^2}{k_{fluid} \cdot (T_f - T_0)} \quad (8)$$

where $\rho \left[\frac{\text{kg}}{\text{m}^3} \right]$ is the fluid density, $v \left[\frac{\text{m}}{\text{s}} \right]$ represents the bulk velocity and $L \text{ [m]}$ is the characteristic dimension of the system. $\nu \left[\frac{\text{m}^2}{\text{s}} \right]$ and $\mu \left[\frac{\text{Ns}}{\text{m}^2} \right]$ are the fluid cinematic and dynamic viscosity, respectively, $k_{fluid} \left[\frac{\text{W}}{\text{m} \cdot \text{K}} \right]$ is the fluid thermal conductivity and $c_p \left[\frac{\text{J}}{\text{kg} \cdot \text{K}} \right]$ is the fluid specific heat. Lastly, T_f is the fluid temperature and T_0 the reference system temperature. Introducing the non-dimensional group and including again the term of viscous forces we obtain:

$$\frac{DT^*}{Dt^*} = \frac{1}{RePr} \nabla^2 T^* + \frac{1}{t^*} q^{III*} + \frac{Br}{RePr} \varphi^* \quad (9)$$

Since the governing equation of convection heat transfer is a second-order, coupled partial differential equation, to find an analytical solution by integration is not possible except for very simple cases far from real applications. For this reason the Newton empirical law is commonly used to solve problems of convection heat transfer ([2], [18], [19]):

$$\dot{q}_{Conv} = h \cdot (T_w - T_f) \left[\frac{\text{W}}{\text{m}^2} \right] \quad (10)$$

where \dot{q}_{Conv} is the convective heat flux, $T_w \text{ [}^\circ\text{C]}$ is the wall temperature, $T_f \text{ [}^\circ\text{C]}$ is the fluid temperature and the parameter h is the convection heat transfer coefficient defined as:

$$h = \frac{-k_{fluid} \cdot \left(\frac{\partial T}{\partial y} \right)_{y=0}}{(T_w - T_\infty)} \left[\frac{\text{W}}{\text{m}^2 \cdot \text{K}} \right] \quad (11)$$

where $k_{fluid} \left[\frac{W}{m \cdot K} \right]$ is fluid thermal conductivity and $\left(\frac{\partial T}{\partial y} \right)_{y=0}$ denotes the temperature gradient along y axis in the boundary layer. By the ratio between convection heat transfer (Eq. 10) and conduction heat transfer (Eq. 2) it is possible to express the convection heat transfer coefficient (unknown of convection problems) as a function of *Nusselt number* (Nu), dimensionless number measure of heat flux due to convection:

$$Nu = \frac{\dot{q}_{Conv}}{\dot{q}_{Cond}} = \frac{h \cdot L}{k_{fluid}} \quad (12)$$

The convection heat transfer from a surface is function of the fluid motion over that, which is described by hydrodynamic boundary layer and thermal boundary layer. The development of the hydrodynamic boundary layer and the thermal boundary layer are related phenomena, described by the dimensionless *Prandtl number* (Pr) [2] (Eq. 7), whose simultaneous development greatly influences the temperature profile and thus the heat transfer by convection. Starting from the solution of the mass, momentum and energy transfer processes equations it is found that the *Nusselt number* can be express as a function of *Reynolds number*, that describes the hydrodynamic boundary layer and *Prandtl number*, link between the two boundary layers.

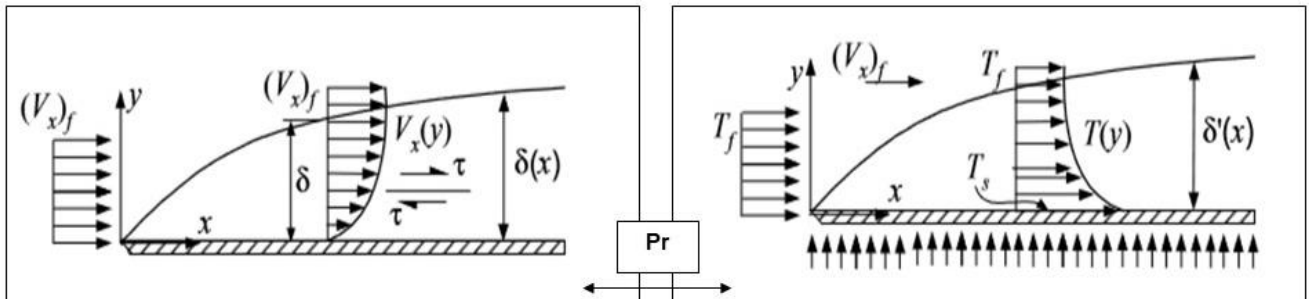


Figure 5: Hydrodynamic and thermal boundary layers for flow over a heated flat plate - Engineering Thermofluids - M. Massoud [2].

To demonstrate this relation between dimensionless numbers we consider a laminar flow over a flat isothermal plate and recall the definition of the convective heat transfer coefficient:

$$h = \frac{-k_{fluid} \cdot \left(\frac{\partial T}{\partial y}\right)_{y=0}}{(T_w - T_\infty)} \quad \left[\frac{W}{m^2 \cdot K} \right] \quad (13)$$

To explicitly express the term $\left(\frac{\partial T}{\partial y}\right)_{y=0}$, let's start recalling the governing equation for the hydrodynamic boundary layer obtained from the conservation equation of momentum:

$$V_x \frac{\partial V_x}{\partial x} + V_y \frac{\partial V_x}{\partial y} = \nu \frac{\partial^2 V_x}{\partial y^2} \quad (14)$$

and the governing equation for the temperature boundary layer obtained from the conservation equation of energy:

$$V_x \frac{\partial T}{\partial x} + V_y \frac{\partial T}{\partial y} = \alpha \frac{\partial^2 T}{\partial y^2} \quad (15)$$

where $\alpha = \frac{k}{\rho \cdot c_p} \left[\frac{m^2}{s} \right]$ is the thermal diffusivity. To find the analytical solutions of these second-order, coupled partial differential equations we have to resolve them as a third order polynomials with the following boundary conditions. For the hydrodynamic boundary layer:

$$\text{at } y=0: v_x=0 \text{ and } \frac{\partial^2 V_x}{\partial y^2} = 0;$$

$$\text{at } y=\delta: v_x = v_f \text{ and } \frac{\partial V_x}{\partial y} = 0.$$

for the thermal boundary layer:

$$\text{at } y=0: T=T_s \text{ and } \frac{\partial^2 T}{\partial y^2} = 0;$$

$$\text{at } y=\delta': T=T_f \text{ and } \frac{\partial T}{\partial y} = 0.$$

where δ is the hydrodynamic boundary layer and δ' is the thermal boundary layer, v_f is the fluid velocity, T_f is the fluid temperature and T_s is the surface temperature. Solving the third order polynomials applying these boundary conditions the velocity and temperature profile become:

$$\frac{V_x}{V_f} = \frac{3}{2} \frac{y}{\delta} - \frac{1}{2} \left(\frac{y}{\delta} \right)^3 \quad (16)$$

and

$$\frac{T - T_s}{T_f - T_s} = \frac{3}{2} \frac{y}{\delta'} - \frac{1}{2} \left(\frac{y}{\delta'} \right)^3 \quad (17)$$

From the derivation of the conservation equations of mass, momentum and energy of the fluid entering and leaving a differential control volume by an integral approach, it is possible to find the relation between the hydrodynamic and thermal boundary layer function of *Prandtl number* (for the complete calculation see [2], chapter IVb, page 525-527):

$$\frac{\delta'}{\delta} = \left(\frac{Pr^{-1/3}}{1.026} \right) \quad (18)$$

Substituting Eq. 17 and Eq. 18 in the definition of the convective heat transfer coefficient, we find:

$$h = \frac{-k_{fluid} \cdot \left(\frac{\partial T}{\partial y}\right)_{y=0}}{(T_w - T_\infty)} = \frac{3}{2} \frac{k}{\delta'} = \frac{3}{2} \frac{k}{\delta} \left(1.026 Pr^{\frac{1}{3}}\right) \quad (19)$$

where we substituted for the thermal boundary layer thickness, δ' in terms of the hydrodynamic boundary layer thickness, δ . To show the relation also with the *Reynolds number* we have to remember that in case of flow over a flat plate in laminar conditions the hydrodynamic boundary layer is found to be (for the complete calculation see [2], chapter IVb, page 524-525):

$$\delta = \frac{5x}{Re_x^{\frac{1}{2}}} \quad (20)$$

Therefore:

$$h = \frac{-k_{fluid} \cdot \left(\frac{\partial T}{\partial y}\right)_{y=0}}{(T_w - T_\infty)} = \frac{3}{2} \frac{k}{\delta} \left(1.026 Pr^{\frac{1}{3}}\right) = \frac{3}{2} \cdot \frac{k}{5x} Re_x^{\frac{1}{2}} \left(1.026 Pr^{\frac{1}{3}}\right) = 0.3 \frac{k}{x} Re_x^{\frac{1}{2}} \left(Pr^{\frac{1}{3}}\right) \quad (21)$$

Using the definition of the *Nusselt number* we find:

$$Nu = 0.3 \cdot Re_x^{\frac{1}{2}} \cdot Pr^{\frac{1}{3}} \quad \text{with } 0.6 \leq Pr \leq 50 \quad (22)$$

This last expression demonstrate the dependency of the *Nu* number on *Re* and *Pr* numbers for laminar flow over a flat plate. A similar functional relationship for the *Nu* number is found also for a turbulent flow over a flat heated plate:

$$Nu = 0.0296 \cdot Re_x^{\frac{4}{5}} \cdot Pr^{\frac{1}{3}} \quad \text{with } 0.6 \leq Pr \leq 60 \quad (23)$$

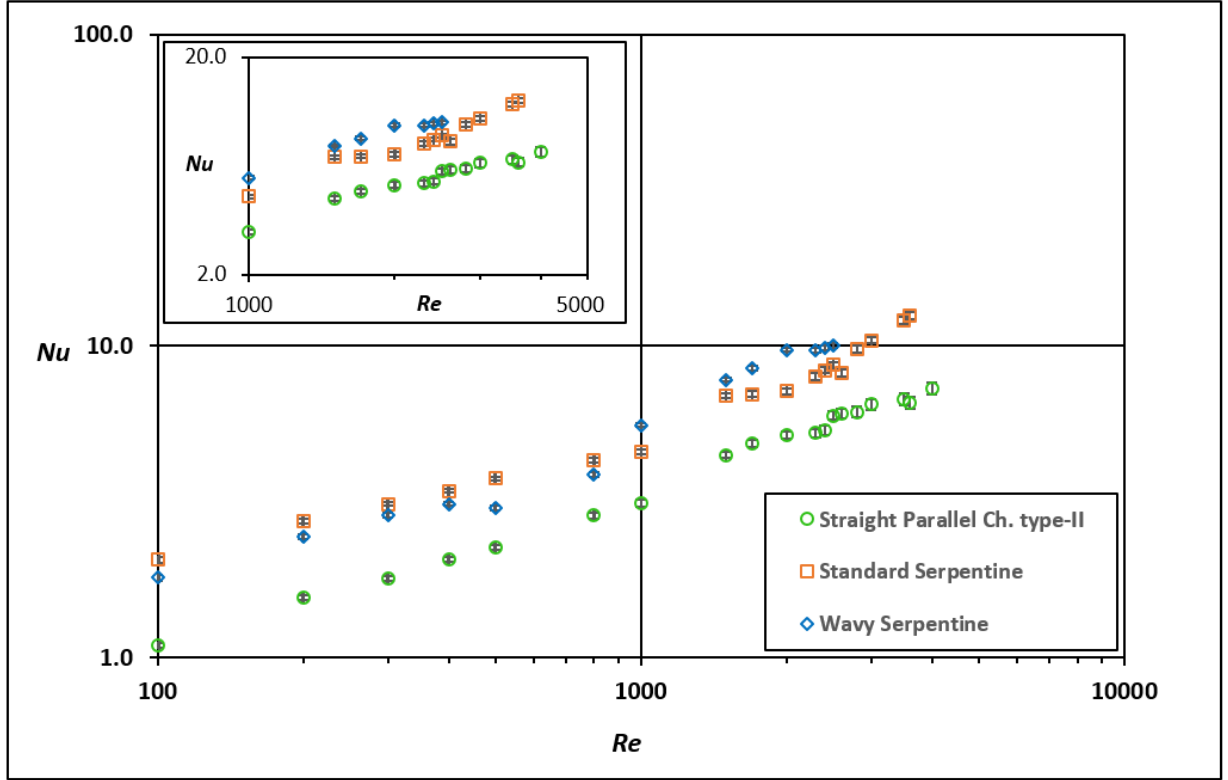


Figure 6: Example of comparison of the Average Nusselt numbers as a function of the Reynolds number obtained for three tested micro-cells at 50 °C.

Therefore, in general we could express this relation as:

$$Nu = C \cdot Re^m \cdot Pr^n \quad (24)$$

where constants C , m , and n depend on a specific case. In conclusion, being *Nusselt number* a measure of heat flux due to convection, the link with *Reynolds number* allows in first analysis to evaluate and compare the heat transfer properties of micro-cells at different flow rate conditions by means of the *Nusselt-Reynolds* diagram, as shown in Figure 6.

2.1 Friction factor and micro-cell efficiency

Being *Nusselt* number a measure of heat flux due to convection, the preliminary comparison of the micro-cells on the *Nu-Re* diagram allows to determine the geometry with higher heat exchange due to convective motions. However this does not take into account an important factor: the pressure losses along the channel. Thus, aiming to define an effective heat exchange efficiency parameter for each micro-device, pressure losses are evaluated in terms of the *Fanning factor* (f). The *Fanning friction factor* is commonly assessed from experimental data as ([14],[20],[21]):

$$f = -\left(\frac{D_h}{0.5\rho U^2}\right) \times \frac{\Delta P}{L} \quad (25)$$

the geometrical parameter D_h [m] and L [m] are the hydraulic diameter and the channel length, respectively. The hydraulic diameter is defined as:

$$D_h = \frac{4A_c}{p} \quad (26)$$

with A_c [m²] the channel cross-section area and p [m] the wetted perimeter. While, the length L is calculated for each geometry considering the channel middle line. ΔP [bar] is the inlet fluid relative pressure measured along the channel axial direction, measured by a pressure sensor on fluid delivery pipe. The ratio D_h/L , shown in Table 1 for all geometries, together with the measured pressure values (ΔP) are the most influential parameters on the value assumed by f .

Channel Type	Channel length L [mm]	Dh [mm]	Dh/L
Straight Channel	101	1	0.0099
Straight Parallel Channels type-II	101	2	0.0198
Standard Serpentine (without and with ribs)	296.5	1	0.0034
Wavy-Sin. Serpentine	354	1	0.0028

Table 1: D_h , L and D_h/L values for each micro-cell.

The term $U^2 \left[\frac{m}{s} \right]$ is the square flow bulk velocity determined as:

$$U = \frac{\dot{Q}}{S} \quad \left[\frac{m}{s} \right] \quad (27)$$

Where $\dot{Q} \left[\frac{ml}{min} \right]$ is the volumetric flow rate and $S [m^2]$ is the channel section equal to $1 \times 10^{-6} m^2$.

The density, $\rho \left[\frac{kg}{m^3} \right]$, here function of fluid average bulk temperature, for water is calculated by means of the physical model describing the density trend as a function of temperature [22]:

$$\rho = -0.003 \cdot T_b^2 - 0.042 \cdot T_b + 1000 \quad (28)$$

While for the two water-glycerin solutions the density values are calculated by online platform based on the formula of A. Volk and C.J. Kähler [23]. Once the pressure-drop losses are established on the base of the *Fanning factor*, f , the heat exchange efficiency of the micro devices, ε , is evaluated by dividing the mean *Nusselt number* by the *Fanning friction factor*, both dependent on *Reynolds number*, in accordance with Y. Sui et al. [14], W.M. Abed et al. [20], Z. Dai et al. [24]. Differently from mentioned literature, in our case the *Nusselt* and friction terms have not been normalized on a reference geometry, *i.e.* the straight channel.

$$\varepsilon = \frac{\overline{Nu}(Re, Pr)}{f(Re)} \quad (29)$$

2.2 Entropy analysis

Following previous works on the argument ([25],[26]), another indicator of the local contribution to mixing and heat exchange is given by the local rate of entropy production, assuming convective motions without internal heat generation. Since any non-equilibrium process is an irreversible process, due to the second law of thermodynamics, it is possible to define the entropy production, S , as a function of temperature and velocity gradients. For this reason the third and last phase of the post-processing consist of to evaluate for each geometry the mean entropy production defined as:

$$S = \frac{k}{T_0^2} \left[\left(\frac{\partial T}{\partial x} \right)^2 + \left(\frac{\partial T}{\partial y} \right)^2 \right] + \frac{\mu(T)}{T_0^2} \left[2 \left\{ \left(\frac{\partial u}{\partial x} \right)^2 + \left(\frac{\partial v}{\partial y} \right)^2 \right\} + \left(\frac{\partial u}{\partial y} + \frac{\partial v}{\partial x} \right)^2 \right] \quad (30)$$

where T_0 is the reference temperature of the system. In this study only the kinetic contribution is considered (second term right side of the equation).

In order to compare the micro-channels by mean fields (velocity magnitude, vorticity and entropy) and better appreciate the fluid motions differences induced along the channel paths, the velocity and entropy fields are normalized on bulk velocity, while the vorticity field is normalized on the inverse of a single frame acquisition time. For a better comparison, also the reference axes have been normalized on the size of a single pixel, function of images resolution. The conversion factors from meter to pixel and from second to frame are determined starting by

the resolution and fps (frame/s) values set during the acquisitions. Examples are shown in the following table:

Micro-cell	Resolution [pixel]	<i>fps</i>	$\frac{\text{n}^\circ \text{ pixel}}{\text{mm}}$	$\frac{1}{\text{fps}}$ [s]	$\left[\frac{\text{pixel}}{\text{frame}}\right] = x \cdot \left[\frac{\text{mm}}{\text{s}}\right]$
Parallel Channels type-II	1024x880	5000	78	2×10^{-4}	$x = 0.0156$
Standard Serpentine	1024x512	8500	81	1.2×10^{-4}	$x = 0.00972$
Wavy-Sin. Serpentine	768x528	10000	92	1×10^{-4}	$x = 0.0092$

Table 2: Conversion factors from pixel to meter and from frame to second.

Chapter 3 - Materials and experimental methods

The setup, sketched in Figure 7, is designed to carry out temperature measurements and micro Particle Image Velocimetry (μ PIV) measurements in order to investigate the thermal aspects and the fluid dynamics of the different micro-cell geometries and conditions tested in this work. The experimental setup is composed by:

- **Thermal analysis**
 - Hot Plate
 - Thermocouple reader (accuracy: ± 0.05 °C)
 - K-type thermocouples (accuracy: ± 1 °C)
 - Infrared thermometer (accuracy: ± 0.05 °C)
 - Syringe pump (accuracy: ± 0.05 ml/min)
- **μ PIV analysis**
 - Tracer (mean size $15\text{ }\mu\text{m}$)
 - Fastcam (pixel size $20\text{ }\mu\text{m} \times 20\text{ }\mu\text{m}$)
- **Pressure analysis**
 - Relative pressure sensor (accuracy: ± 0.002 bar)

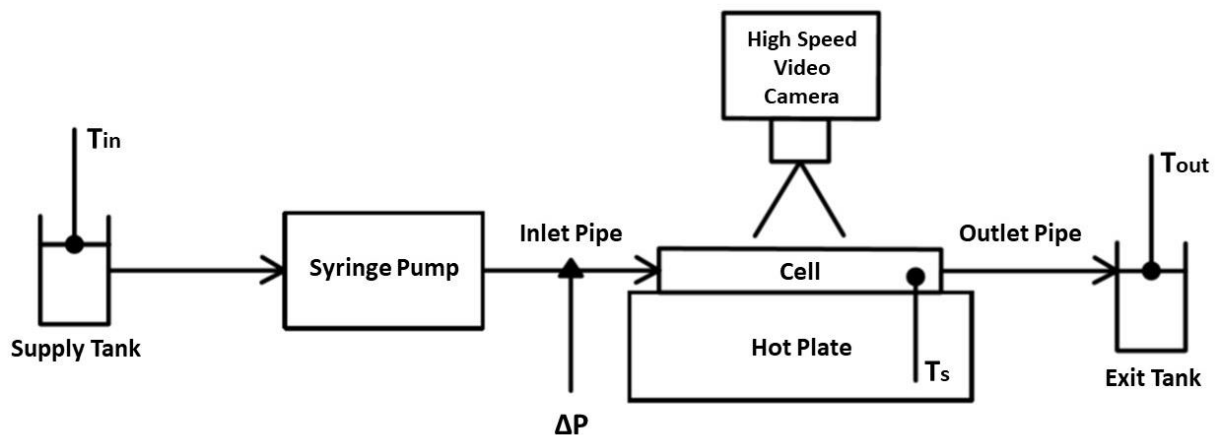


Figure 7: Sketch of the experimental setup.

Starting from the first component to the left side of the scheme in Figure 7, the syringe Pump, Landgraff LA-800 (working range: 1.74 $\mu\text{L/hr}$ to 340 ml/min, accuracy: ± 0.05 ml/min), provided with a 140 ml syringe, introduces the cooling fluid into the micro-channel at different set flow rates. Distilled Water is used as the working fluid, but for the conventional serpentine path is also implemented a solution with two different percentages of glycerin and water (70 % glycerin and 30 % water; 30 % glycerin and 70 % water). The hot plate Stuart US-150 (working range: 0 $^{\circ}\text{C}$ to 325 $^{\circ}\text{C}$), in direct contact with the micro-cell bottom side, is used to maintain the system under a constant heat flux setting up two temperature values equal to 50 and 70 $^{\circ}\text{C}$, while four K-type thermocouples (working range: ± 200 $^{\circ}\text{C}$ to +1372 $^{\circ}\text{C}$, accuracy: ± 1 $^{\circ}\text{C}$) are used to measure the inlet/outlet water and the micro-cell surface temperatures. To carry out μPIV measurements the micro-cell is placed under a high-speed camera Photron Mini AX100 (working range: 5000 fps (frames/s) at resolution of 1024×880 pixel, up to 12500 fps at 640×480 pixel, accuracy: pixel size $20\mu\text{m} \times 20\mu\text{m}$) to acquire high resolution images of the region of interest and the working fluid is seeded by hollow glass spherical tracers *Sphericel 110P8* with mean size equal to 15 μm provided by *Potters Industries LLC*. In order to evaluate the heat exchange efficiency for each geometry, the pressure drop (ΔP) along the axial direction of the microchannel is measured by a Flowplus16-ViscoTec relative pressure sensor (working range: 70 mbar to 7 bar, accuracy: ± 0.002 bar). For each instrument more details will be provided in the following paragraphs.

3.1 Micro Devices

Six different geometric configurations are used for laboratory testing: the classical straight channel configuration, the two configurations with parallel channels (named in Figure 8 as type-I and type-II), the conventional serpentine path, with and without ribs, and the wavy-sinusoidal serpentine path.

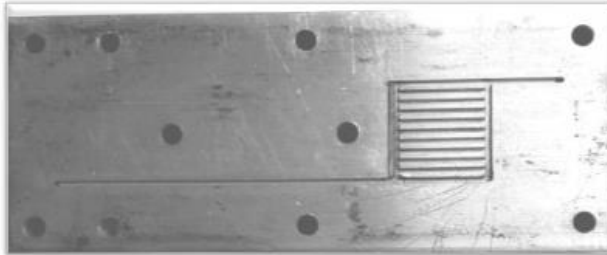
Rectilinear Channel



Parallel Channels type-I



Aluminium Parallel Channels type-I



Parallel Channels type-II



Serpentine Channel (with & without ribs)



Wavy Serpentine Channel



Figure 8: Geometrical configurations studied.

All micro-devices are composed of an aluminum bottom side and a plexiglass top side. The micro channel is milled on the adiabatic part of the micro-cell to help cooling by micro heat exchangers application on existing industrial devices. To assess the influence of the channel material on the heat exchange rate, a comparison between the straight parallel channels cell type-I assembled in an adiabatic material (plexiglass) and assembled in a conductive material (aluminum) was also carried out. The overall structure of the cells has a total length of 120 mm, a width of 50 mm and a height of 22 mm. In particular, for all the cells the plexiglass top side has a height of 10 mm, while the aluminium bottom side is slightly higher, *i.e.* equal to 12 mm to allow the insertion of the thermocouples. The upper and lower parts are tightened together by M4 type screws. The tested geometries are manufactured in the mechanical workshop of the Department of

Mechanical and Aerospace Engineering (DIMA) of University La Sapienza. The processes are performed by numerically controlled milling machine (CNC) on the base of detailed CAD drawings of the single parts to be realized. The use of a CNC milling machine allowed to obtain the channel path with a precision of about ± 0.01 mm. To avoid leakage of cooling fluid and to guarantee a pressure sealing, all configurations have three common elements. The first concerns the realization of a 2 mm wide frame around the channel path, as shown in Figure 9.



Figure 9: Example of a sealing frame manufactured on the straight parallel channels cell type-I.

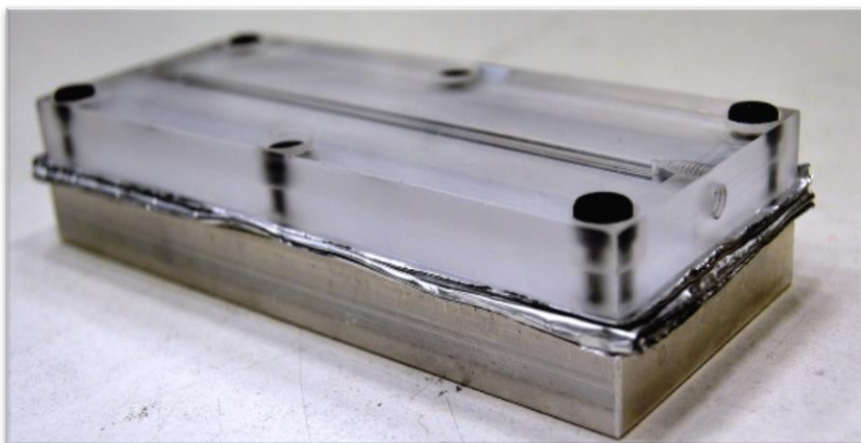


Figure 10: Straight channel cell with aluminum gap-pad.

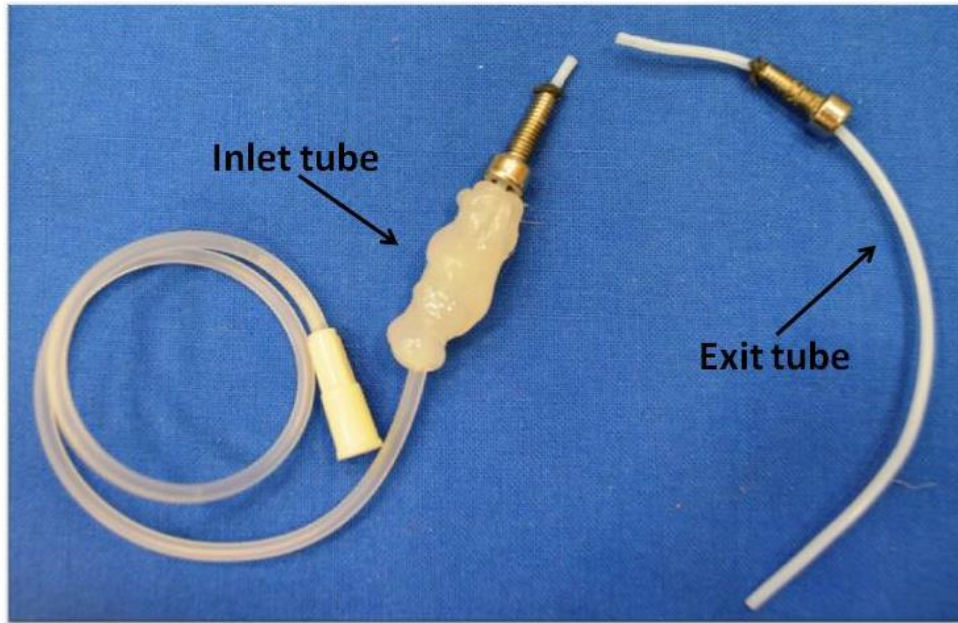


Figure 11: Inlet and exit tubes.

The second is the insertion of a black neoprene gap-pad (for PIV measurements, to enhance the particle tracer images over background) or an aluminum gap-pad (for thermal measurements, to guarantee heat transfer), with a thickness of about 1 mm, between the top and bottom side of the cell. An example of cell assembly with gap-pad is shown in Figure 10. Thirdly, to connect the micro-cell to the syringe pump, a PVC tube with an internal diameter of 1.2 mm and a special Luer-Lock connection is used. The PVC tube is joined to another PLA tube with an internal diameter of 1 mm that is inserted directly in the cell and fixed with a perforated screw. An additional rubber gasket located at the PLA tube outlet section prevents leaks at the inlet of the channel. For the exit tube, internal diameter 1 mm, seal is guaranteed only by rubber gasket located at the connection point between the outlet section of the channel and the tube inlet section. The 300 mm long inlet tube and the 100 mm long exit tube are shown in the following Figure 11.

3.1.1 Straight channel micro-cell

The cell used for the validation of the measurement system consists of a simple straight channel milled on the plexiglass top. The duct has a square cross-section $1 \times 1 \text{ mm}^2$, a length of about 101 mm and a heat exchange area equal to 101 mm^2 . The main features of the straight channel are reported in Table 3.

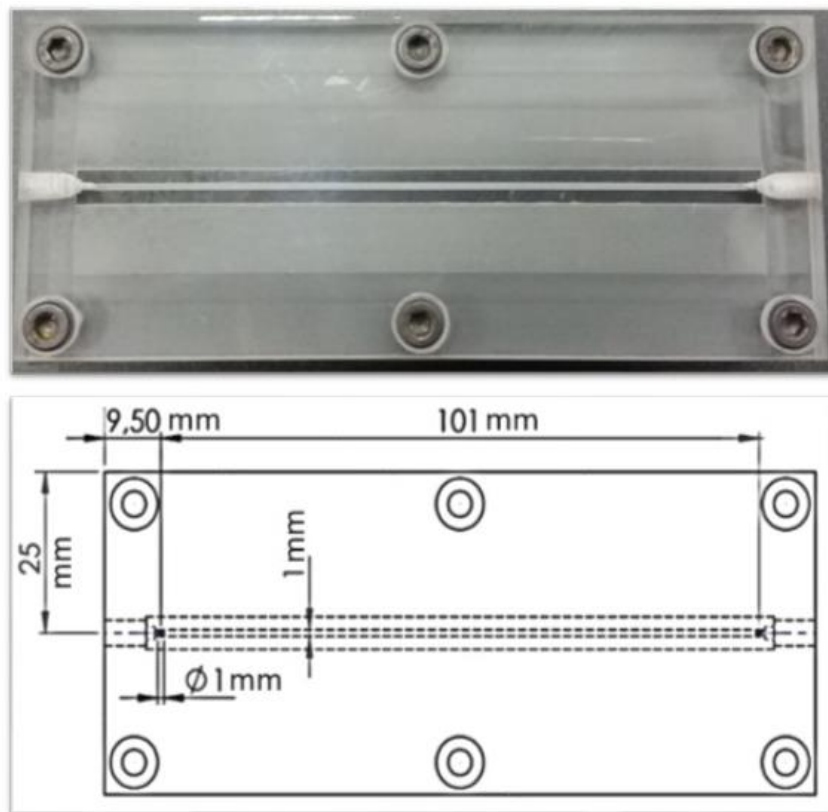


Figure 12: Top view and CAD drawing of the straight channel micro-cell.

Channel length [mm]	101
Hydraulic diameter [mm]	1
Heat exchange area [mm^2]	101
Plexiglass top thickness [mm]	10
Aluminium base thickness [mm]	12

Table 3: Main features of the straight channel micro-cell.

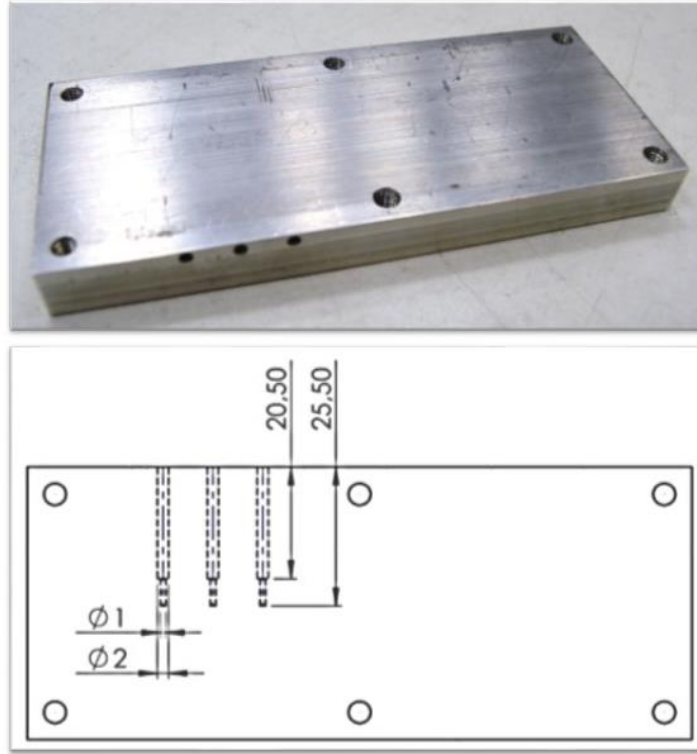


Figure 13: View of the aluminum bottom side and CAD drawing of the thermocouples venues.

As shown in Figure 13, the aluminum bottom side of the micro-cell presents in the sidewall three holes for the positioning of the thermocouples in order to measure the surface temperature. The three holes have a variable diameter of 2 mm up to a depth of 20.50 mm and of 1 mm in the last 5 mm (Figure 13). The three thermocouples are located at the middle of the channel, distant 9 mm one from each other and at a depth of 0.5 mm.

3.1.2 Straight parallel channels micro-cell type-I

The cell is made as a prototype of a parallel channels micro-heat exchanger to study the flow distribution in each (single) channel. Possible changes to be made to increase the homogeneity of the flow within all channels have been considered and applied in the straight parallel channels micro-cell type-II. The starting geometry, shown in Figure 14, is composed of 11 parallel channels with a square cross-section $1 \times 1 \text{ mm}^2$, an inlet aligned with the first channel and an

outlet duct aligned with the last one. Only the vertical manifold, downstream of the inlet channel, has a cross-section $2 \times 1 \text{ mm}^2$ in order to insert elements to guide the fluid in the channels (Figure 15). This configuration has a heat exchange area around 308 mm^2 and a distance between the entrance and exit hole of about 101 mm. As reported in Table 4 the inlet channel length is around 65.5 mm to allow a complete development of the velocity field in laminar regime. This length is established on the base of the following definition [2],[18]:

$$L_{inlet} = 0,05 \cdot D_h \cdot Re \quad (31)$$

Where D_h the hydraulic diameter. By considering a hydraulic diameter equal to 1 mm and a flow rate of 78 ml/min ($Re = 1300$) the inlet length needed for a complete development of the velocity field is equal to 65 mm.

Total Channel length [mm]	101
Single Channel length [mm]	17
Inlet Channel length [mm]	65.5
Outlet Channel length [mm]	13.5
Hydraulic diameter [mm]	1
Heat exchange area [mm ²]	308
Plexiglass top thickness [mm]	10
Aluminium base thickness [mm]	12

Table 4: Main features of the straight parallel channels micro-cell type-I.

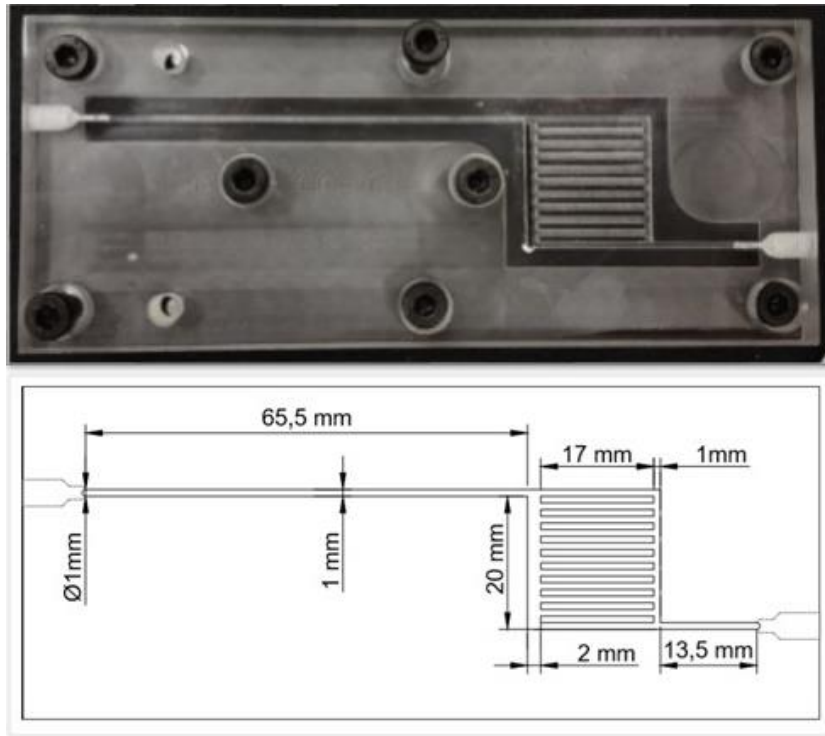


Figure 14: Top view and CAD drawing of the straight parallel channels micro-cell type-I.

The fluid guide elements, made by laser cutting technology due to the very small dimensions, were designed with well-studied shapes based on a preliminary study [27] able to better distribute the flow rate along the different channels. The Figure 15 shows the four profiles manufactured.

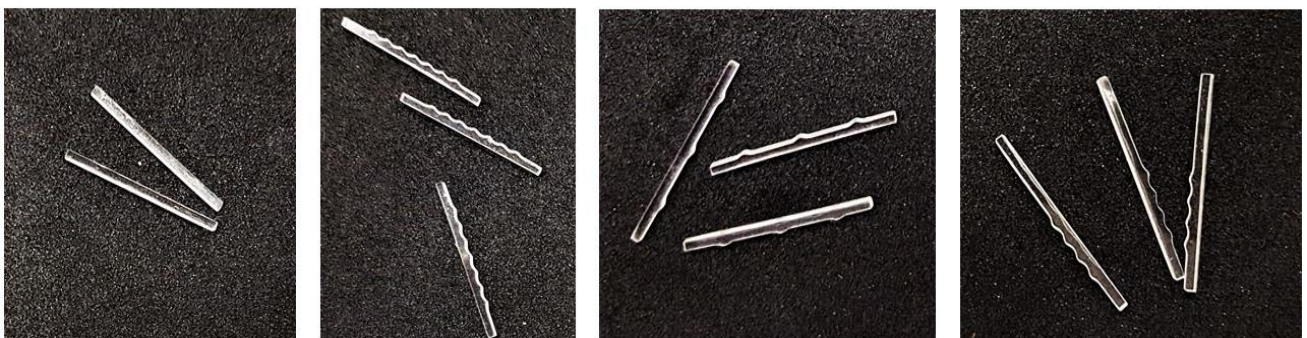


Figure 15: Fluid guide profiles and the placement scheme with flow rate percentages.

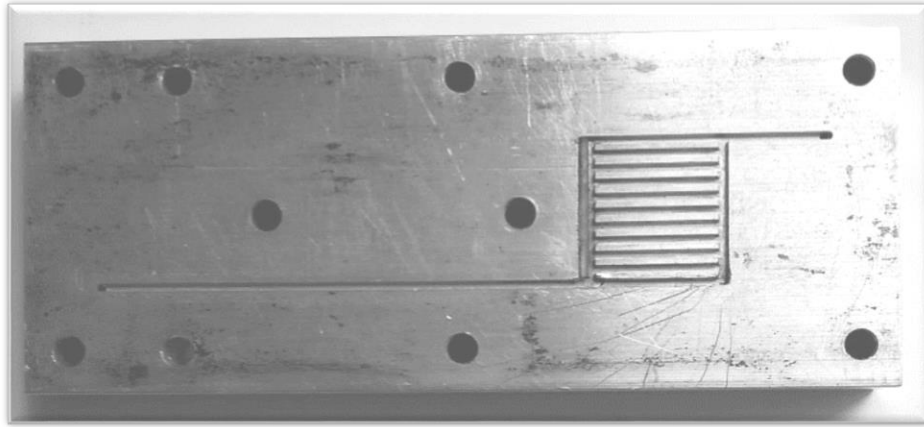


Figure 16: Top view of the aluminum straight parallel channels micro-cell type-I.

Unlike the other configurations, for this cell, the thermocouple holes in the aluminum bottom side have not been made, since the study was focused especially on the analysis of the flow distribution inside the channels. In addition, to evaluate the influence of the channel material on the heat exchange rate, this configuration is the only one that was assembled also in a conductive material (aluminum) and compared with the plexiglass one on the base of the fluid outlet temperature. In Figure 16 the aluminum straight parallel channels micro-cell type-I is shown, the geometric features are the same as the previous one, except for a major heat exchange area equal to 775 mm².

3.1.3 Straight parallel channels micro-cell type-II

The type-II parallel channels cell, to be considered as a reference for the study, is designed as an evolution of the previously described geometry. The study of the flow distribution in the cell type-I suggested the modification of the inlet and outlet ducts geometry from the parallel channels section and critical points such as leading edges between fluid and ribs. In detail, as shown in Figure 17, the inlet and outlet ducts have been transformed into flow collection areas, symmetrical with respect to the parallel channels section, with a curvilinear profile (angles equal

to 16° and 31°) and growing cross-section (from 1 mm to 21 mm). In order to prevent preferential flows in the central ducts, balance the inlet and outlet pressure gradient and guide the flow towards peripheral channels. The critical points as leading edges between fluid and ribs have been rounded to avoid flow separation and generation of three-dimensional motions. The test section is composed by 11 square cross-section $1 \times 1 \text{ mm}^2$ channels and has the same size of the previous one, $19 \text{ mm} \times 21 \text{ mm}$. The heat exchange area is around 947 mm^2 with a distance between the entrance and exit hole of about 101 mm.

Total Channel length [mm]	101
Single Channel length [mm]	19
Hydraulic diameter [mm]	2
Heat exchange area [mm^2]	947
Plexiglass top thickness [mm]	10
Aluminium base thickness [mm]	12

Table 5: Main features of the straight parallel channels micro-cell type-I.

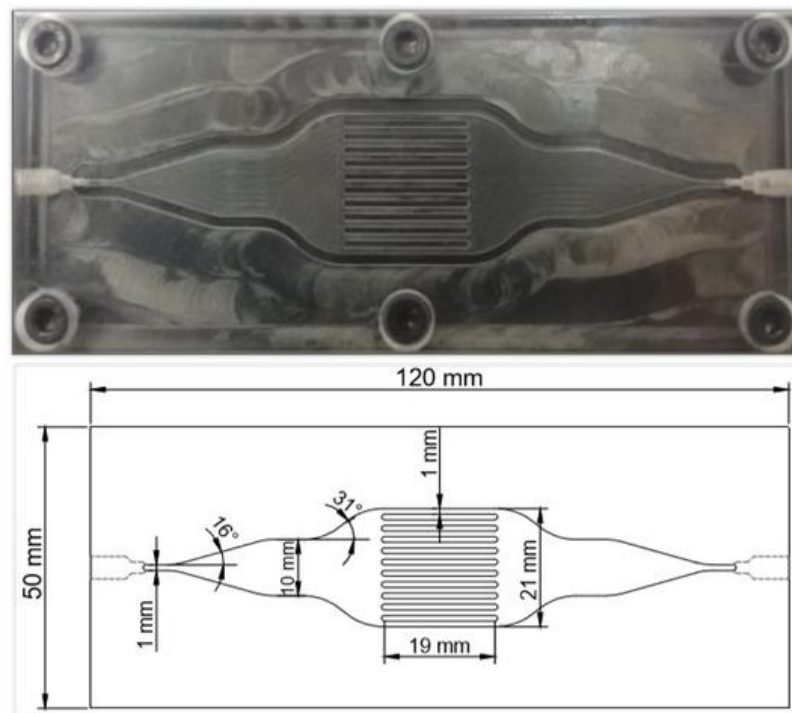


Figure 17: Top view and CAD drawing of the straight parallel channels micro-cell type-II.

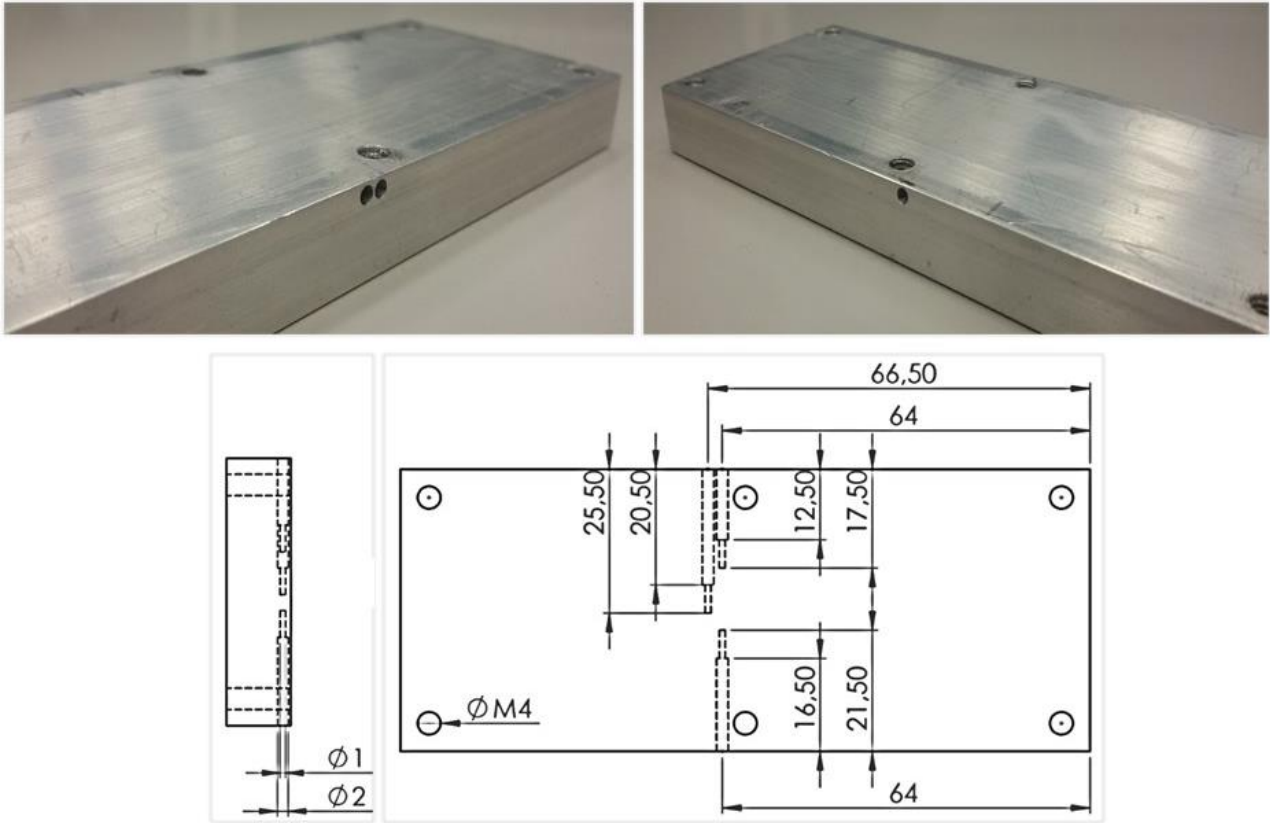


Figure 18: View of the aluminum bottom side and CAD drawing of the thermocouples venues.

Also in the aluminum bottom side of this geometry there are three thermocouples venues, but, differently by the straight channel, two venues are located in the right sidewall and one in the left wall in order to measure the surface temperature under the two most peripheral channels and under the central one. As shown in Figure 18, the three holes have different lengths and also in this case the diameter varies with depth.

3.1.4 Standard serpentine micro-cell

A standard serpentine cell is implemented to test this well-known configuration in a different adiabatic material, in view of an easy implementation on existing engineering devices. The channel of the standard serpentine configuration has a square cross-section $1 \times 1 \text{ mm}^2$, an equivalent length of 296.5 mm and an included angle equal to 90° . This configuration is

characterized by 11 U-elements. Each U-element of the geometry has two horizontal sections with a length of 19 mm and a vertical section with a length of 3 mm. The test section is 19 mm \times 21 mm, while the heat exchange area is 296.5 mm². The main features are reported in Table 6.

Total Channel length [mm]	296,5
Single Channel length [mm]	19
Inlet Channel length [mm]	67,5
Outlet Channel length [mm]	14,5
Hydraulic diameter [mm]	1
Heat exchange area [mm ²]	296,5
Plexiglass top thickness [mm]	10
Aluminium base thickness [mm]	12

Table 6: Main features of the standard serpentine cell.

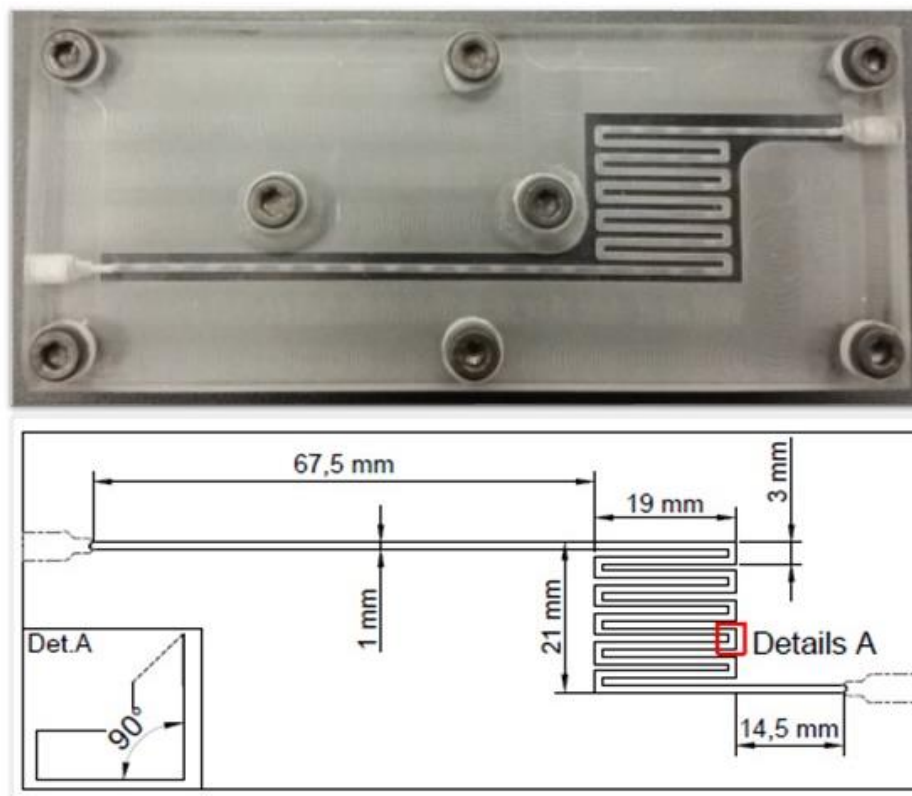


Figure 19: Top view and CAD drawing of the standard serpentine cell.

For the standard serpentine and wavy-sinusoidal serpentine cells the aluminum base has the same characteristics. Unlike the previous cells, in these last cases, the holes for thermocouples are located on the short side of the base so as to measure the surface temperature under the first channel, the last channel and the central one (Figure 20). The three venues have a variable diameter of 2 mm up to a depth of 27.50 mm and of 1 mm in the last 5 mm of depth (Figure 20). The three thermocouples are located at the middle of the channel, distant 10 mm from each and at a depth of 0.5 mm. This configuration is also tested with horizontal ribs, the goal being to increase the device efficiency by a higher heat exchange surface, without altering the main features of the geometry, using conductive elements inside the channel (ribs). The new heat exchange area is equal to 459.3 mm². The ribs are cylindrical steel elements with a diameter of 0.4 mm and a length of 17 mm equal to the single channel length; they are fixed on the gap-pad surface in alignment whit the duct axis and positioned in the middle of the channel, Figure 21a. The view of the cross-section in Figure 21b shows the reduction of flow passage in the U-element horizontal sections from a square cross-section 1 × 1 mm to two side aisles 0.3 mm × 1 mm and one upper section 1 mm × 0.6 mm.

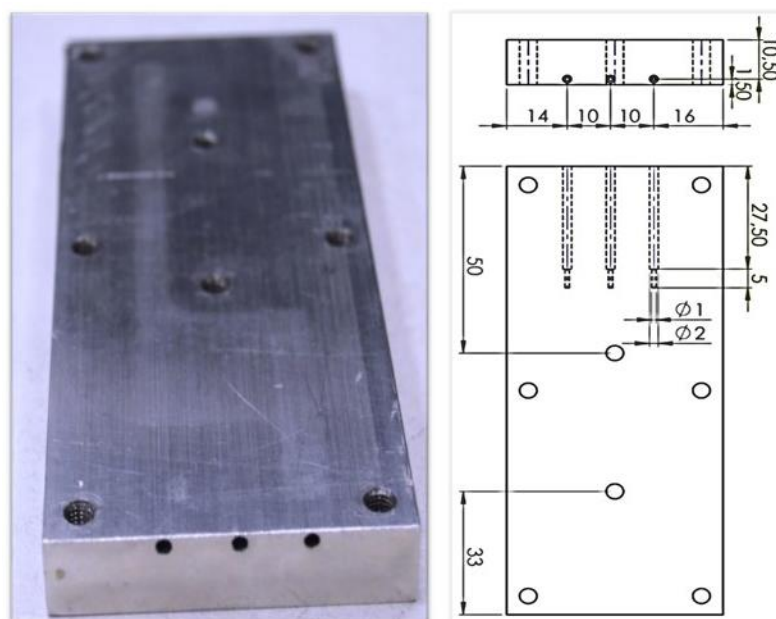


Figure 20: View of the aluminum bottom side and CAD drawing of the thermocouples venues.

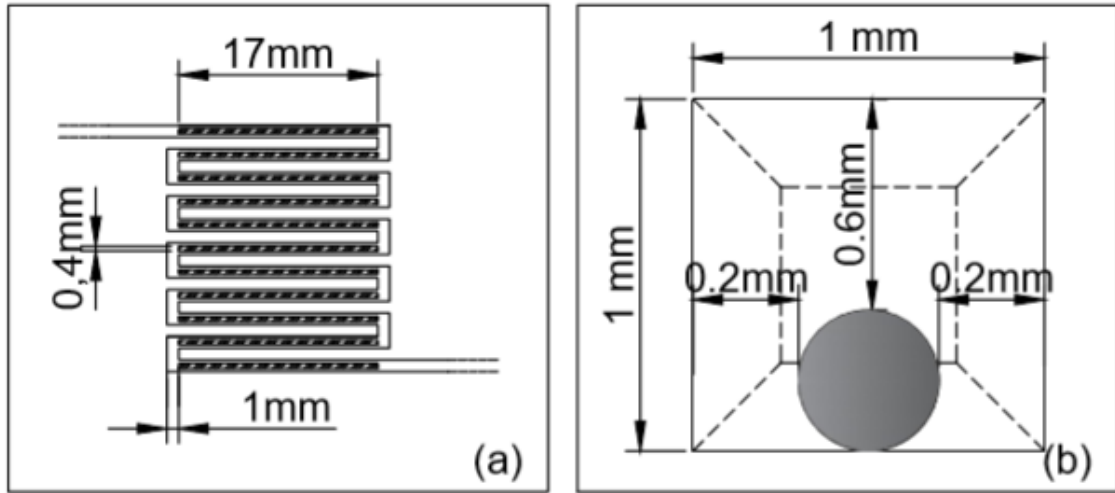


Figure 21: Standard serpentine micro-cell with ribs. (a) Top view of the test section; (b) View in the cross-section with rib.

3.1.5 Wavy-sinusoidal serpentine micro-cell

This geometry was designed to increase the thermal exchange efficiency without addition of elements inside the channel, *e.g.* ribs, due to possible limitations in the modification of mechanical or electrical components to be cooled and to large pressure losses. The aim is to obtain a higher heat exchange rate through a wavy geometry to increase the wetted surface and promoting the generation of three-dimensional motions. The idea is to combine the fluid mixing properties of the wavy path [24] with the heat transfer properties of the standard serpentine path [28], leading to the realization of a new wavy-sinusoidal serpentine micro-cell, shown in Figure 22.

The new proposed channel has a square cross-section $1 \times 1 \text{ mm}^2$ and an equivalent length of 354 mm. The test section has the same size of the standard serpentine and parallel channels configurations equal to $19 \text{ mm} \times 21 \text{ mm}$. As the previous cell, the inlet channel length of 67 mm allows a complete development of the thermal and velocity fields. Each wavy element has an

inner radius of 0.25 mm and an external radius of 1.25 mm. This configuration is characterized by 7 U-elements with two horizontal sections with a length of 19 mm and a vertical section with a length of 5.6 mm. The aluminium base is the same of the standard serpentine cell.

Total Channel length [mm]	354
Single Channel length [mm]	19
Inlet Channel length [mm]	67.5
Outlet Channel length [mm]	14.5
Hydraulic diameter [mm]	1
inner radius [mm]	0.25
external radius [mm]	1.25
Heat exchange area [mm ²]	354
Plexiglass top thickness [mm]	10
Aluminium base thickness [mm]	12

Table 7: Main features of the wavy-sinusoidal serpentine cell.

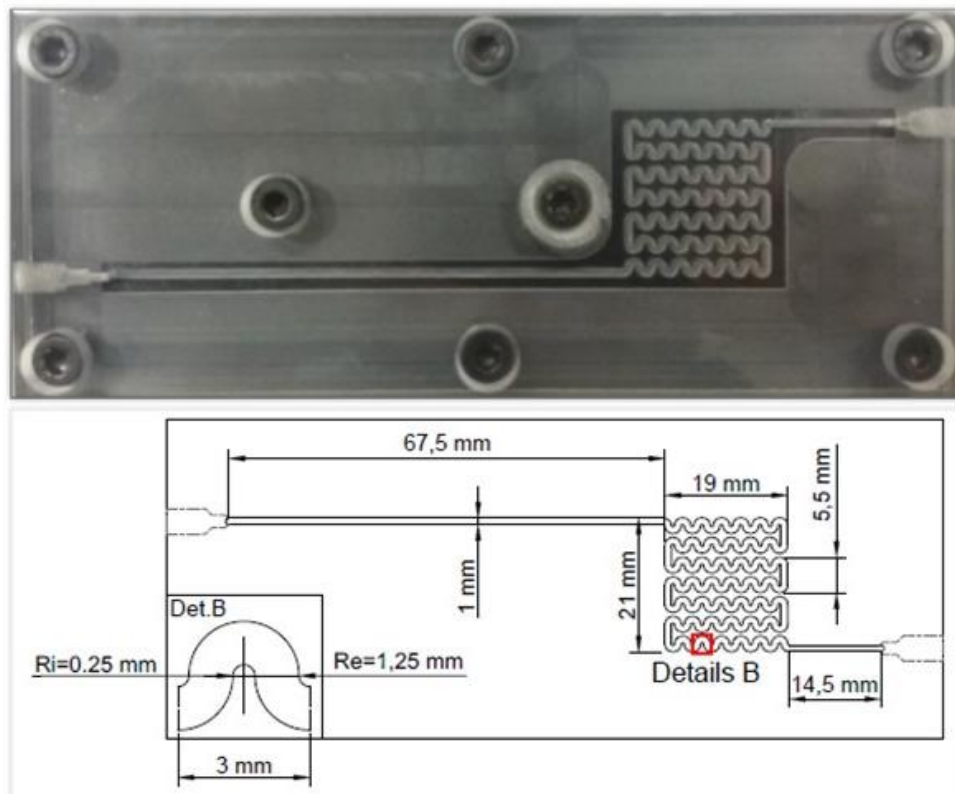


Figure 22: Top view and CAD drawing of the wavy-sinusoidal serpentine.

3.2 Syringe Pump



Figure 23: Hll Landgraf LA-800 Syringe Pump.

The syringe pump used is an Hll Landgraf LA-800. This analogue instrument allows to work with 140 ml syringes and up to a 12 bar pressure. From the LCD/LED display it is possible to set:

- The Rate: from a minimum of 1.74 $\mu\text{L}/\text{hr}$ to a maximum of 340 ml/min;
- the volume of the syringe: in our case equal to 140 ml;
- the diameter of the syringe: in our case equal to 40 mm.

Through the pump controls positioned below the display is possible to set a flow rate in ml/min with a single digit after the decimal point, which corresponds to an instrument absolute error on our flow rate settings equal to ± 0.05 ml/min. For the experimental tests it was necessary to modify the supplied plastic syringe and make another special one in aluminum. This was done to increase its structural resistance, in order to withstand the considerable stresses given by the thrust forces exerted by the pump on the syringe piston due to the high fluid entry pressure in the micro-cell. Especially in case of very complex geometries, *e.g.* wavy-sinusoidal serpentine, or

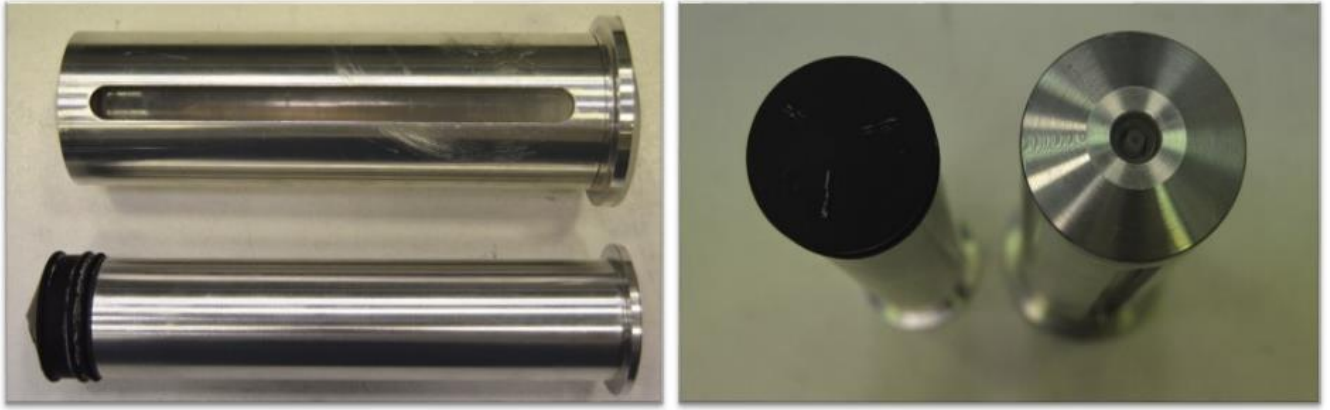


Figure 24: Modified 140 ml aluminum syringe. Lateral view (left image) and front view (right image).

very viscous cooling fluid, *i.e.* glycerin. The modified 140 ml syringe, shown in Figure 24, is reinforced with an outer extruded aluminum sleeve and the plastic piston is completely replaced by a solid aluminum cylinder on which the rubber sealing cover can be fixed.

3.2.1 Flow rate studied

As briefly said before, the micro-cell geometry and the type of fluid to be used greatly influence the thrust force that the syringe pump exerts on the fluid into the micro-device. The thrust also depends on the set flow rate and therefore on the flow regime in the channel, *e.g.* laminar, transient, turbulent. For this reason, it was not possible to define a number of equal flow rates for all configurations, since for some of these the thrust required to introduce the fluid into the channel far exceeded the mechanical limits of the instrument (Maximum operating pressure: 12 bar; maximum operating force: 100 kg). The flow rates considered to perform the thermal measurements are reported in the following table for all configurations. To carry out μ PIV measurements, the flow rates of 30 ml/min and 90 ml/min were considered for all cells.

Cooling Fluid: <u>Distilled Water</u>	Re	Speed [m/s]	Straight Channel [ml/min]	Parallel Channels type-II [ml/min]	Standard Serpentine [ml/min]	Standard Serpentine with ribs [ml/min]	Wavy Serpentine [ml/min]
Laminar Flow	100	0.1	6	6	6	6	6
	200	0.2	12	12	12	12	12
	300	0.3	18	18	18	18	18
	400	0.4	24	24	24	24	24
	500	0.5	30	30	30	30	30
	800	0.8	48	48	48	48	48
	1000	1.0	60	60	60	60	60
	1500	1.5	90	90	90	90	90
	1700	1.7	102	102	102	102	102
	2000	2.0	120	120	120	120	120
	2300	2.3	138	138	138	138	138
Transient	2400	2.4	144	144	144	144	144
	2500	2.5	150	150	150	150	150
	2600	2.6	156	156	156	156	-
	2800	2.8	168	168	168	168	-
	3000	3.0	180	180	180	180	-
Turbulent Flow	3500	3.5	210	210	210	-	-
	3600	3.6	216	216	216	-	-
	4000	4.0	240	240	-	-	-

Cooling Fluid: <u>30 % Glycerin – 70 % Water</u>	Re	Speed [m/s]	Standard Serpentine [ml/min]
Laminar Flow	37	0.1	6
	75	0.2	12
	112	0.3	18
	150	0.4	24
	187	0.5	30
	299	0.8	48
	374	1.0	60
	561	1.5	90
	636	1.7	102
	748	2.0	120
	860	2.3	138
	898	2.4	144
	935	2.5	150
	972	2.6	156
	1047	2.8	168
	1122	3.0	180

Cooling Fluid: <u>70 % Glycerin – 30 % Water</u>	Re	Speed [m/s]	Standard Serpentine [ml/min]
Laminar Flow	4	0.1	6
	7	0.2	12
	11	0.3	18
	14	0.4	24
	18	0.5	30
	29	0.8	48
	36	1.0	60
	54	1.5	90

Table 8: Listing of flow rates, Reynolds numbers and speed values analyzed for each micro-cell.

As can be seen from Table 8, the highest flow rates typical of the turbulent regime have been reached for the simpler and linear geometries, able to easily drain the inlet flow, with distilled water as cooling fluid characterized by a low viscosity ($\mu=0.00095743$ Ns/m² at 21 °C). For the straight channel and the parallel channels type-II cells, a maximum flow rate of 240 ml/min ($Re = 4000$) is achieved, while a slightly lower flow rate of 216 ml/min ($Re = 3600$) is reached for the standard serpentine cell due to slightly higher pressure losses given by bending zones. In the case of complex geometries such as the wavy-sinusoidal serpentine or with obstacles along the channel path (ribs), the maximum flow rate gotten is 150 ml/min ($Re = 2500$) and 180 ml/min ($Re = 3000$), respectively, due to higher loads.

In the same way, the use of a different cooling fluid much more viscous than pure distilled water leads to an important reduction in the achievable flow rate. For the standard serpentine cell tested with the 30 % glycerin – 70 % water solution ($\mu = 0.0029028$ Ns/m² at 21 °C) a maximum flow rate of 180 ml/min is reached ($Re = 1122$), while for the same cell tested with the 70 % glycerin – 30 % water solution ($\mu = 0.033236$ Ns/m² at 21 °C) a much lower maximum flow rate is reached equal to 90 ml/min ($Re = 54$), due to a higher viscosity. The method used to derive the thermo-chemical properties of the water-glycerin solution will be described in detail in chapter 2.

3.3 Hot Plate

For the performance of the thermal measurements the hot plate Stuart US-150, placed in direct contact with the micro-cell bottom side, is used to maintain the system under a constant heat flux. During the measurement campaign, the plate is set at two temperatures equal to 50 and 70 °C to allow a thermal comparison between cells at different boundary conditions. The temperature values of 50 °C and 70 °C chosen for the study are very close to the temperatures

reached by the real components in engineering applications [29], [30]. It hasn't been possible to study higher temperatures because plexiglass already exhibits ductile behavior at 90 °C. The Stuart US 150 is an analogue instrument with an operating range from 0 °C to 325 °C. The heating plate made of aluminum-silicon alloy has dimensions 172 × 248 × 12 mm (width, length, height) and the temperature surface is regulated by a knob with temperature steps of 50 °C. The error relating to this instrument can be considered null. The set temperature is the same reached by the hot plate after a transitional period, function of the selected value. For example for a temperature value of 50 °C the heating time is around 5 minutes and 8 minutes for a temperature of 70 °C.



Figure 25: Hot plate Stuart US-150.

3.4 Infrared Thermometer

The infrared thermometer is employed during the experimental tests to verify the hot plate temperature: in the plate heating phase, to check the achievement of the selected temperature, and in the testing phase to monitor the surface temperature. The infrared thermometer PCE 779N, shown in Figure 26, works in range from $\pm 60\text{ }^{\circ}\text{C}$ to $+760\text{ }^{\circ}\text{C}$ with a response time of 1 second. The temperature measured and showed on display have a single digit after the decimal point, therefore it is possible to define an absolute error of $\pm 0.05\text{ }^{\circ}\text{C}$. For a correct temperature measurement it is necessary to place the thermometer orthogonal to the surface at a distance of 100-150 mm.



Figure 26: Infrared thermometer PCE 779N.

3.5 Thermocouples Reader

Another instrument in support of the thermal measurements are K, J, E, T, N and R-type thermocouple readers. In this research work only K-type thermocouples (Chromel (Ni-Cr)/Alumel (Ni-Al)) are used because more suitable to work in the studied temperatures range ([31],[32]). The instrument is equipped with four outputs and works in a range from ± 200 °C to $+1372$ °C (K-type). The thermocouples data are collected and transferred to PC with a frequency of one data per second. The SE521 software supplied with the reader is used to download data. The absolute error of the instrument is ± 0.05 °C (the measured value is given with one digit after the decimal point).



Figure 27: K, J, E, T, N and R-type thermocouple reader SE521.

Four K-type thermocouples acquires water temperature at the outlet of the micro cell and of cooled surface. One of the thermocouples is dived in the outlet water flow, while the other three are positioned inside the bottom side, in the middle of the heat exchange area and at a depth of 0.5 mm, as described in the micro-cells section. The K-type thermocouples have a resolution of 0.1 °C and an accuracy of ± 1 °C. The total number of values recorded by thermocouples is dependent on the total time to void the syringe, which is a function of flow rate. The maximum records number equal to 1400 values is obtained at the minimum flow rate of 6 ml/min, while at the maximum flow rate of 240 ml/min the records fall to around 35 values.

Flow Rate [ml/min]	Records number/ Syringe time [s]
6	1400
12	700
24	350
90	93
180	47
240	35

Table 9: Amount of values recorded as a function of flow rate starting by a fixed volume of 140 ml.

3.6 Tracer

To apply Particle Image Velocimetry (μ PIV) technique is necessary to seed the working fluid with a tracer. By the determination of tracer displacements in fluid flow is possible to derive the velocity fields of the micro-cells. In detail, hollow glass spherical tracers are used, with a range size 5-25 μ m, density equal to 0.00105 g/mm³ and characterized by a Stokes time scale equal to $1.375 \cdot 10^{-5}$ s. In Figure 28 a sample of tracer is shown. The glass particles, provided by *Potters Industries PQ Corporation*, come in the form of a white powder, non-flammable and soluble in water. The softening-point is around 730 °C.



Figure 28: Sample of hollow glass spherical particles.

To make up the water-tracer mixture to be used in the PIV measurements, 140 ml of water are mixed through a manual mixing using a spoon with a quantity of particles which depends on type of geometry. So, for all geometries, an accurate weight of tracer was selected, as shown in Table 10.

Micro-cell type	Weight of Particles
Straight Channel	1.2 g
Parallel Channels	0.7 g
Standard Serpentine	0.6 g
Serpentine with Ribs	0.6 g
Wavy-Sin. Serpentine	0.4 g

Table 10: Micro-cell type with indication of the correct dosage of tracer in grams.

3.7 Fast-Cam

Whit aim to detect tracer displacements in fluid flow and then to perform μ PIV analysis, high resolution images are acquired with the high-speed camera Photron Mini AX100 starting from 5000 fps (frames/s) at resolution of 1024×880 pixel, up to 12500 fps at 640×480 pixel.



Figure 29: Fast-cam Mini AX100 and Nikon objectives.

The Fast-cam Mini AX100 can work in a range of 4000 fps at full resolution of 1024×1024 pixel, up to a maximum frame rate of 540.000 fps with a reduced resolution of 128×16 pixel. A global electronic shutter 1 ms to 1 μ s ensures several shutter options independent of frame rate and a selectable region of interest in steps of 128 pixel (horizontal direction) \times 16 pixel (vertical direction) allows the camera a more versatile use. The PFV software version 3.6.8.1 is used to manage the camera acquisition set up. Nikon objectives of various sizes are mounted on the camera to zoom in to channel details. As well as the resolution, also the acquisition time and the total images acquired are a function of the set frame rate:

- » Frame rate of 5000 fps - amount images acquired: 6350 frames - acquisition time: 1.27 sec.
- » Frame rate of 8500 fps - amount images acquired: 10914 frames - acquisition time: 1.28 sec.
- » Frame rate of 10000 fps - amount images acquired: 14111 frame - acquisition time: 1.41 sec.
- » Frame rate of 12500 fps - amount images acquired: 18627 frame - acquisition time: 1.49 sec.

However, these reduced acquisition times are not statistically significant. To increase the measurement time and reduce the statistical error the acquisition process is divided into 15 or

20 partitions. To better explain the argument we start for example from a frame rate of 5000 fps, with a total acquisition time of 1.27 sec without partitions and a total number of images equal to 6350 frames. Setting a subdivision into 20 partitions, the camera captures 317 frames in 0.064 sec for each partition, to which must be added the transition time from one partition to the other spent by operator, estimated equal to 2 sec. By summing up all seconds, you get a longer acquisition time equal to 39.27 sec.

$$t_{Acq.} = (N_{part.}) \cdot t_{part.} + (N_{tran.}) \cdot t_{tran.} = (20) \cdot 0.064 \text{ s} + (19) \cdot 2 \text{ s} = 39.27 \text{ s} \quad (32)$$

For each geometry and flow rate the optimal set-up was identified to acquire clear images of the region of interest. Below is a summary table of the set conditions for each micro-cell at fluid velocities of 0.5 m/s (flow rate of 30 ml/min) and 1.5 m/s (flow rate of 90 ml/min). For the flow rate of 90 ml/min the partitions number is reduced from 20 to 15 due to a minor exhaustion time of the 140 ml syringe. To acquire clear images a lights equipment is also required made of three LED lights bulbs 24 Watt each.

Micro-Cell	Flow Rate 30 ml/min				Flow Rate 90 ml/min			
	Partition	fps	Resolution	Shutter	Partition	fps	Resolution	Shutter
Straight Channel	20	10.000	768 × 512	1/14.000	15	10.000	768 × 512	1/30.000
Parallel Channels type-II	20	5.000	1024 × 880	1/frame	15	8.500	512 × 864	1/frame
Standard Serpentine Ch.	20	8.500	1024 × 512	1/frame	15	10.000	768 × 528	1/14.000
Serpentine Ch. with Ribs	20	8.500	1024 × 512	1/frame	15	12.500	640 × 480	1/14.000
Wavy-Sin. Serpentine Ch.	20	10.000	768 × 528	1/frame	15	10.000	768 × 528	1/14.000
Stand. Serpentine with 30%Glycerin-70%Water	20	8.500	1024 × 512	1/frame	15	10.000	768 × 528	1/14.000
Stand. Serpentine with 70%Glycerin-30%Water	20	8.500	1024 × 512	1/frame	15	10.000	768 × 528	1/14.000

Table 11: Summary of the set conditions.

3.8 Pressure Sensor



Figure 30: Flowplus16-ViscoTec pressure sensor, on the left. Elveflow OB1-MK3, on the right.

The pressure drop (ΔP) along the axial direction of the micro-channel is measured by a Flowplus16-ViscoTec relative pressure sensor shown in Figure 30. The operating range goes from 70 mbar to 7 bar with an accuracy down to $\pm 2\%$ of full scale. This sensor works in a temperature range from 15 °C to 45 °C. The provided voltage output, ranging from 0.1 V (≤ 70 mbar) to 10 V (7 bar), is transmitted and read directly on the OB1-MK3 display. The perfect seal is guaranteed by a double Luer-Lock connection. The OB1-MK3, shown in Figure 30, is a microfluidic flow control system produced by *Elveflow*. Due to the flow rate limit imposed by the technical features of the sensor of 100 ml, the pressure measurements have been carried out in a narrow range of flow rate from 6 ml/min (0.1 m/s) to 100 ml/min (1.7 m/s). The measure provided by sensor has two digit after the decimal point, so the error relating to this instrument is assumed equal to ± 0.005 bar.

3.9 Determination of Reynolds number

The dynamic effects due to the fluid flow are retained in the *Reynolds number*. For each flow rate the corresponding value of Re is calculated according to the definition given in previous section:

$$Re = \frac{\rho U l}{\mu} \quad (33)$$

For all geometries the side of the channel square cross-section, equal to 10^{-3} m, is chosen as the characteristic dimension of the system (l [m]) and the bulk velocities (U [$\frac{m}{s}$]) are calculated from the flow rate values:

$$U = \frac{\dot{Q}}{S} \quad \left[\frac{m}{s} \right] \quad (34)$$

Where \dot{Q} [$\frac{ml}{min}$] is the volumetric flow rate and S [m^2] is the channel section equal to $1 \times 10^{-6} m^2$.

For the parallel channels cell type-II the calculated Re are relative to the fluid flow within the single parallel channel. While, for the serpentine cell with ribs, the calculated values refer to the inlet channel flow condition. With reference to physical properties of distilled water, ρ [$\frac{kg}{m^3}$] and μ [$\frac{Ns}{m^2}$], are determined by means of water property tables by fixing a reference temperature of 21 °C; corresponding to the water inlet temperature in micro-cells kept constant for all the measures carried out. In the following table the parameters used to calculate Re numbers are presented.

Parameter	Value	Unit
Characteristic dimension (l)	0.001	[m]
Section (S)	$1 \cdot 10^{-6}$	[m^2]
Density (ρ)	1000	[kg/m^3]
Dynamic viscosity (μ)	0.00095743	[Ns/m^2]
Cinematic viscosity (ν)	$1 \cdot 10^{-6}$	[m^2/s]

Table 12: Reynolds number parameters. Cooling fluid: distilled water.

Unlike *Nusselt number*, whose calculation is shown in the following paragraph, the *Reynolds number* is calculated on the base of the initial conditions of the system, equal for all configurations, in order to compare the devices regardless of flow temperature variation along

the channel, function of geometry and type of fluid. In Table 13 the Re and bulk velocity values obtained are listed for each flow rate.

Flow rate [ml/min]	U [m/s]	Reynolds
6	0.1	100
12	0.2	200
18	0.3	300
24	0.4	400
30	0.5	500
48	0.8	800
60	1.0	1000
90	1.5	1500
102	1.7	1700
120	2.0	2000
138	2.3	2300
144	2.4	2400
150	2.5	2500
156	2.6	2600
168	2.8	2800
180	3.0	3000
210	3.5	3500
216	3.6	3600
240	4.0	4000

Table 13: Reynolds numbers and bulk velocity values. Cooling fluid: distilled water.

In the case of the standard serpentine cell tested with two different water-glycerin solutions, the characteristic dimension of the system and the bulk velocity values, function of flow rate, remain unchanged. To determine the density and dynamic viscosity values for the two solutions an online platform is used [23]. Starting from the syringe volume of 140 ml, the solutions proposed consist of:

- 30 % Glycerin & 70 % Water: 42 ml of glycerin and 98 ml of water;
- 70 % Glycerin & 30 % Water: 98 ml of glycerin and 42 ml of water.

In the following tables the parameters used to calculate the new Re numbers are presented.

Parameter	Value	Unit
Characteristic dimension (l)	0.001	[m]
Section (S)	$1 \cdot 10^{-6}$	[m ²]
Density (ρ)	1085.6	[kg/m ³]
Dynamic viscosity (μ)	0.0029028	[Ns/m ²]
Cinematic viscosity (ν)	$2.7 \cdot 10^{-6}$	[m ² /s]

Table 14: Reynolds number parameters. Solution with 30 % glycerin & 70 % water.

Parameter	Value	Unit
Characteristic dimension (l)	0.001	[m]
Section (S)	$1 \cdot 10^{-6}$	[m ²]
Density (ρ)	1192.8	[kg/m ³]
Dynamic viscosity (μ)	0.033236	[Ns/m ²]
Cinematic viscosity (ν)	$2.79 \cdot 10^{-5}$	[m ² /s]

Table 15: Reynolds number parameters. Solution with 70 % glycerin & 30 % water.

In Table 16 the Re and bulk velocity values obtained are listed for each flow rate.

Cooling Fluid: 30 % Glycerin – 70 % Water	Flow rate [ml/min]	U [m/s]	Reynolds
	6	0.1	37
	12	0.2	75
	18	0.3	112
	24	0.4	150
	30	0.5	187
	48	0.8	299
	60	1.0	374
	90	1.5	561
	102	1.7	636
	120	2.0	748
	138	2.3	860
	144	2.4	898
	150	2.5	935
	156	2.6	972
	168	2.8	1047
	180	3.0	1122

Cooling Fluid: 70 % Glycerin – 30 % Water	Flow rate [ml/min]	U [m/s]	Reynolds
	6	0.1	4
	12	0.2	7
	18	0.3	11
	24	0.4	14
	30	0.5	18
	48	0.8	29
	60	1.0	36
	90	1.5	54

Table 16: Reynolds numbers and bulk velocity values obtained for the two tested solutions.

3.10 Determination of Nusselt number

The mean *Nusselt number* accounts for the relative importance of convective to conductive heat transfer, both expressed at the surface. In a heated micro-channel under a constant heat flux condition it is generally obtained from the experimental data as ([33],[34],[35]):

$$\overline{Nu} = \left(\frac{D_h}{k_{fluid}} \right) \times \frac{\dot{m} \cdot c_p \cdot (T_{b,out} - T_{b,in})}{A_s(T_w - T_b)} \quad (35)$$

where $\dot{m} \left[\frac{\text{kg}}{\text{s}} \right]$ is the mass flow rate, $c_p \left[\frac{\text{J}}{\text{kg} \cdot ^\circ\text{C}} \right]$ is the fluid specific heat and $k_{fluid} \left[\frac{\text{W}}{\text{m} \cdot ^\circ\text{C}} \right]$ is the fluid thermal conductivity. $T_w [^\circ\text{C}]$ and $T_b [^\circ\text{C}]$ are the wall temperature and the bulk temperature, respectively, with T_b defined as the mean value between the bulk fluid temperature at the inlet ($T_{b,in} [^\circ\text{C}]$) and the outlet of the channel ($T_{b,out} [^\circ\text{C}]$):

$$T_b = \frac{T_{b,out} + T_{b,in}}{2} \quad (36)$$

$D_h [\text{m}]$ denotes the hydraulic diameter and $A_s [\text{m}^2]$ is the heated micro-channel surface area.

The hydraulic diameter is defined as:

$$D_h = \frac{4A_c}{p} \quad (37)$$

with $A_c [\text{m}^2]$ the channel cross-section area and $p [\text{m}]$ the wetted perimeter. The main feature of each geometry are reported in Table 17.

Channel Type	Area [mm ²]	Channel length <i>L</i> [mm]	<i>Dh</i> [mm]
Straight Channel	101	101	1
Straight Parallel Channels type-II	947	101	2
Standard Serpentine	296.5	296.5	1
Standard Serpentine with ribs	459.3	296.5	1
Wavy-Sin. Serpentine	354	354	1

Table 17: Geometrical parameters of the tested micro-cells.

Among all terms that appear in the *Nu* equation some are constant, others are calculated and still others has been extrapolated starting from experimental data. The inlet fluid temperature falls within the constant parameters. The $T_{b,in}$ term corresponds to the water (or solution) inlet temperature in micro-cells, kept constant at 21 °C for all the measures carried out. The fixed temperature value of 21 °C ensure a temperature gradient between fluid and surface of about 30 °C, for a set hot plate temperature of 50 °C, and of about 50 °C, for a set hot plate temperature of 70 °C. In addition, a cooling fluid temperature equal to the ambient temperature could encourage the implementation of micro heat exchangers on some existing applications.

Differently, parameters such as mass flow rate (\dot{m}), fluid specific heat (c_p) and thermal conductivity (k_{fluid}) are calculated by means of the following equations. The mass flow rate (\dot{m}) is determined starting from the volumetric flow rate (\dot{Q}) definition, multiplied by the working fluid density (ρ) at 21 °C:

$$\dot{m} = \rho \cdot \dot{Q} = \rho \cdot U \cdot S \left[\frac{\text{kg}}{\text{s}} \right] \quad (38)$$

Where \dot{Q} are the set flow rates and ρ is equal to: for water to $1000 \frac{\text{kg}}{\text{m}^3}$, for the solution with 30 % glycerin and 70 % water to $1085.6 \frac{\text{kg}}{\text{m}^3}$, for the solution with 70 % glycerin and 30 % water to $1192.8 \frac{\text{kg}}{\text{m}^3}$. In the following table the mass flow rates obtained in each condition are listed.

Flow rate [ml/min]	\dot{m} fluid: water	\dot{m} fluid: 30 % Gl./70 % Wt.	\dot{m} fluid: 70 % Gl./30 % Wt.
6	0.0001	0.0001	0.0001
12	0.0002	0.0002	0.0002
18	0.0003	0.0003	0.0004
24	0.0004	0.0004	0.0005
30	0.0005	0.0005	0.0006
48	0.0008	0.0009	0.0010
60	0.0010	0.0011	0.0012
90	0.0015	0.0016	0.0018
102	0.0017	0.0018	-
120	0.0020	0.0022	-
138	0.0023	0.0025	-
144	0.0024	0.0026	-
150	0.0025	0.0027	-
156	0.0026	0.0028	-
168	0.0028	0.0030	-
180	0.0030	0.0033	-
210	0.0035	-	-
216	0.0036	-	-
240	0.0040	-	-

Table 18: Mass flow rate values corresponding to set flow rates for each working fluid.

As regards the fluid thermal parameter c_p and k ; the fluid specific heat and thermal conductivity are calculated at the fluid average bulk temperature. In particular for water, these parameters are evaluated on the base of the following physical models describing the properties trend as a function of temperature [22]:

$$c_p = -10^{-4} \cdot T_b^3 + 0,028 \cdot T_b^2 - 1,753 \cdot T_b + 4206 \quad (39)$$

$$k = 2,72 \cdot 10^{-10} \cdot T_b^5 - 6,12 \cdot 10^{-8} \cdot T_b^4 + 4,84 \cdot 10^{-6} \cdot T_b^3 - 1,64 \cdot 10^{-4} \cdot T_b^2 + 3,62 \cdot 10^{-3} \cdot T_b + 0,56 \quad (40)$$

In the case of water-glycerin solutions, since there are no tool online to use, the thermal properties are calculated by summing up the c_p and k values of the single parts, weighed on the related percentages by volume (sol-1: 30 % glycerin & 70 % water; sol-2: 70 % glycerin & 30 % water) [36]:

$$c_p = Vol_w\% \cdot c_{p_w} + (1 - Vol_w\%) \cdot c_{p_g} \quad (41)$$

$$k = Vol_w\% \cdot k_w + (1 - Vol_w\%) \cdot k_g \quad (42)$$

The subscripts w and g indicate water and glycerin, respectively. The physical models described above are applied to determine water parameters. For glycerin, instead, the tables available in literature are not enough detailed in order to read, or calculate with a low error, the values of c_p and k associated to temperatures very close to each other. Furthermore, despite several researches, a website that allows to calculate the thermal properties of pure glycerin isn't found.

Then, to determine the c_p and k values an online fluid property calculator [37] that reports Ethylene Glycol among the different fluids proposed is used. As can be seen from Table 19, ethylene glycol has thermo-physical properties very close to those of glycerin. For this reason the glycol specific heat and thermal conductivity, evaluated at different bulk temperatures, are used in the calculation of the two solutions thermal properties.

Properties Table at 20 °C		
Liquid	Glycerin	Ethylene glycol
Density - ρ	0.00126 [g/mm ³]	0.00111 [g/mm ³]
Thermal conductivity - k	0.244 [W/mK]	0.249 [W/mK]
Specific heat - c_p	2.39 [kJ/kgK]	2.38 [kJ/kgK]

Table 19: Glycerin and Ethylene glycol properties table.

Lastly the extrapolation method applied to the last two terms, $T_{b,out}$ and T_w , is described in detail below.

Chapter 4 - Results: Thermal Measurements

In this section, the heat exchange capacity of all systems here proposed is quantified in terms of *Nusselt number* and compared at different *Reynolds numbers*, by settling the hot source temperature first to 50 °C and then to 70 °C. For all experimental measurements the inlet fluid temperature is kept constant at 21 °C. On the base of measurements of water and aluminum temperatures, the average *Nusselt number* is determined for each flow rate, geometry and cooling fluid conditions as described in chapter 3. In order to be able to give comments on the relative heat exchange performance of the tested micro-cells, it is important to bear in mind that the principal difference given by convective motions, as far as heat transfer is concerned, is an additional intense mechanism of heat transfer in the radial and azimuthal directions, commonly called “eddy transport”, that provide much better transfer of energy across the flow at a given axial position [38]. Therefore, thanks to the physical meaning of *Nu* number and its link with the *Re* number, it is possible in first analysis to look at the *Nusselt-Reynolds* curves and identify the configuration with the highest values of heat flux due to convection by suggesting a more efficient heat transfer. On the *Nu-Re* diagram the trends are also compared with the classical correlation proposed by Sieder & Tate [39] for laminar flow in circular cross-section straight conduits with a length-diameter ratio greater than 10, a *Prandtl number* (*Pr*) ranging from 0.48 to 16700 and a ratio $\frac{\mu}{\mu_w}$ ranging from 0.0044 to 9.75; with the aim to detect the main differences induced by geometry on the curves especially in the flow regime transition region. The Sieder & Tate correlation is the following [34],[39]:

$$Nu = 1.86 \cdot \left(\frac{D_h}{L} \cdot Re \cdot Pr \right)^{\frac{1}{3}} \cdot \left(\frac{\mu}{\mu_w} \right)^{0.14} \quad (43)$$

where D_h [m] is the hydraulic diameter, L [m] is the conduit total length, $\mu \left[\frac{\text{Ns}}{\text{m}^2} \right]$ is the fluid dynamic viscosity and $\mu_w \left[\frac{\text{Ns}}{\text{m}^2} \right]$ is the fluid dynamic viscosity evaluated at wall temperature, T_w [°C].

4.1 Temperature experimental data

For all micro-cells the raw data are the temperature measurements of the outlet fluid and cooled surface, the latter are taken inside the aluminum bottom, at a distance of 0.5 mm from surface, in three different points under the region of interest as shown in paragraph 3.1. For each case of study thermal measurements are taken under different flow conditions, from a minimum value equal for all of 6 ml/min, up to a variable maximum value in accordance with geometry considered (paragraph 3.2.1). The data are collected with a frequency of one data per second and the total measurement time is function of set flow rate as derived from emptying time of 140 ml syringe (Table 9). On the base of raw data, the temperature trends as a function of time and flow rate are derived. Being all curves very similar to each other, only the curves obtained for the standard serpentine cell are shown as an example for both hot plate temperatures of 50 °C and 70 °C. For the wall, the average temperature of the three values measured below surface is considered, as described in A.1 Interpolation and extrapolation method.

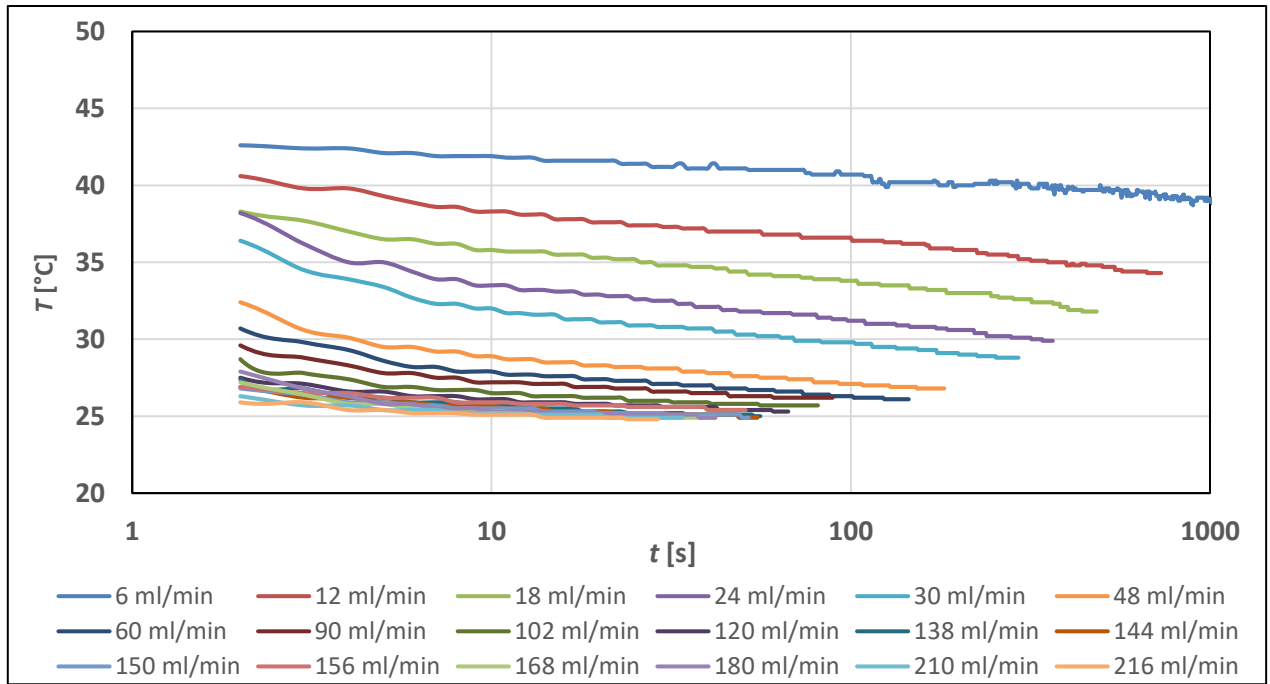


Figure 31: Water temperatures as a function of time [s] and flow rate [ml/min] for the standard serpentine cell at 50 °C.

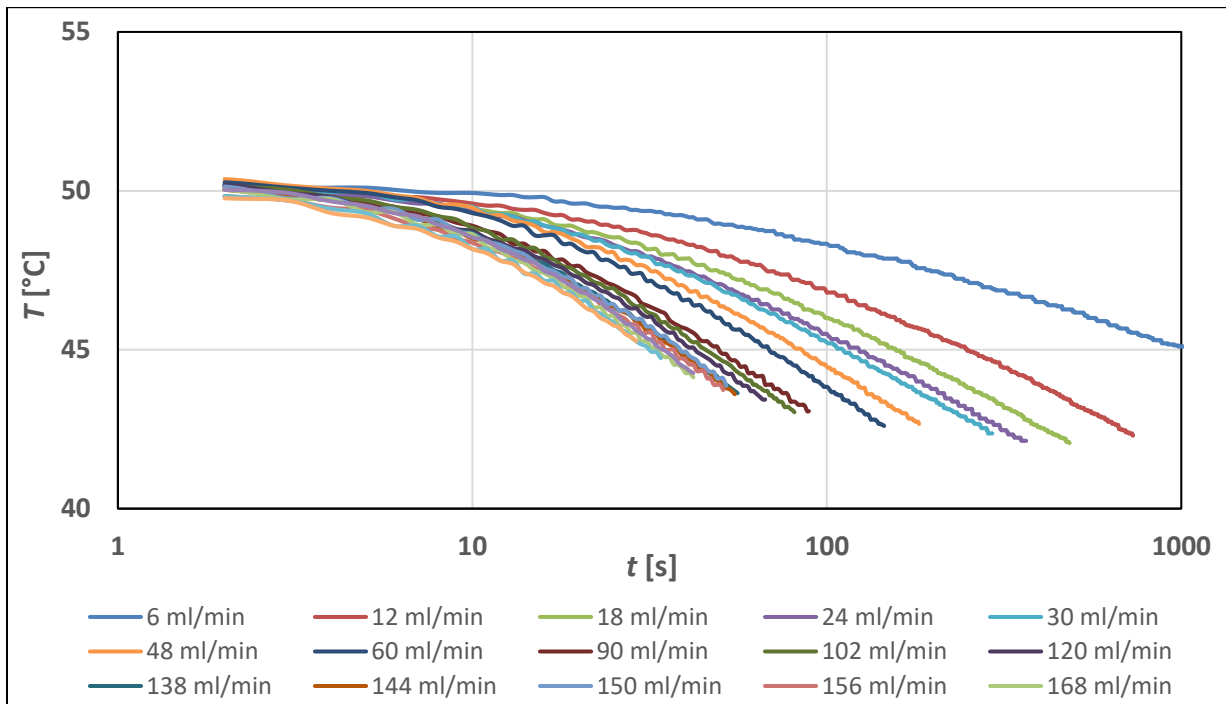


Figure 32: Wall temperatures as a function of time [s] and flow rate [ml/min] for the standard serpentine cell at 50 °C.

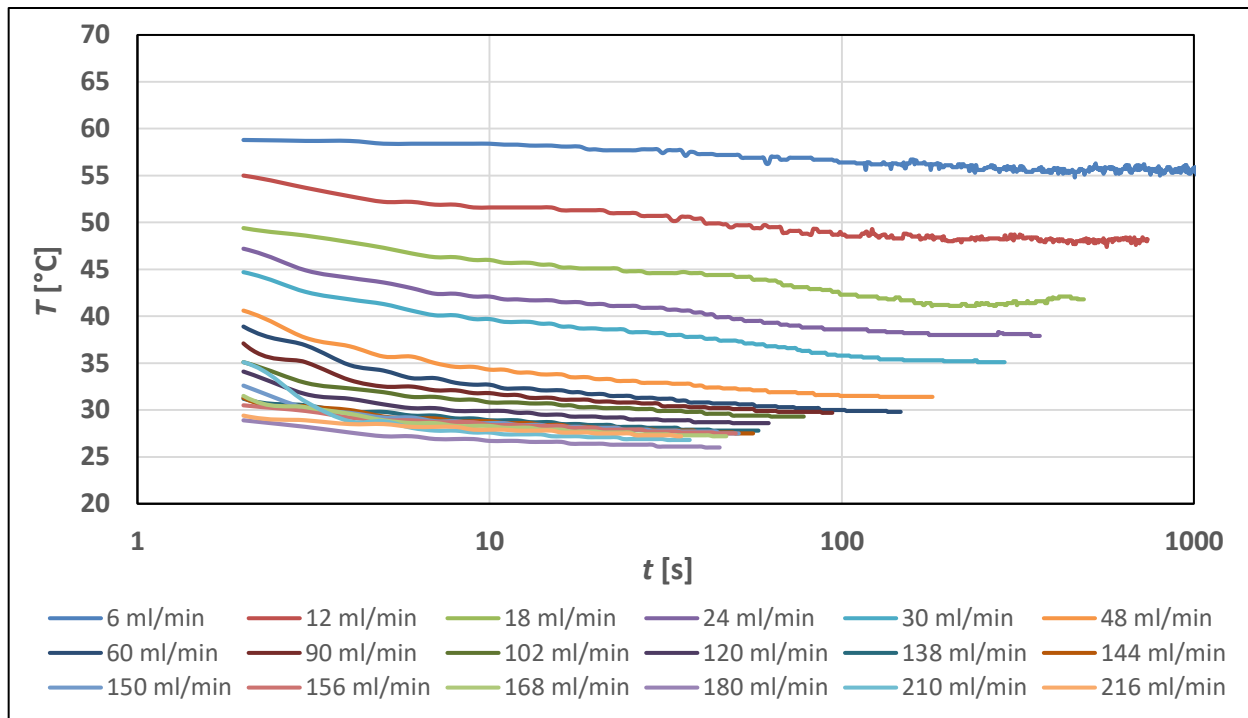


Figure 33: Water temperatures as a function of time [s] and flow rate [ml/min] for the standard serpentine cell at 70 °C.

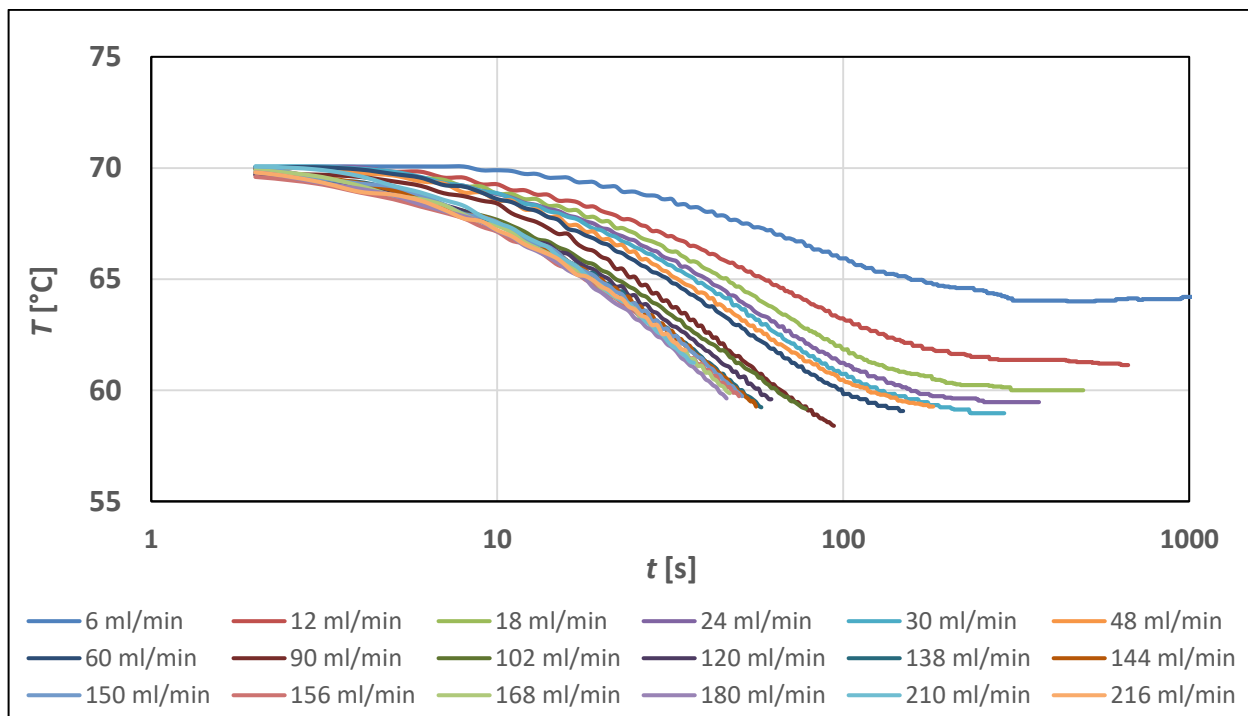


Figure 34: Wall temperatures as a function of time [s] and flow rate [ml/min] for the standard serpentine cell at 70 °C.

By observing these figures, it is noticeable that in all measurements initially the temperature decreases rapidly from values close to the hot source temperature to a plateau after a thermal transient, whose duration is a function of the flow rate, *i.e.* of *Reynolds number*. A constant temperature of outlet fluid presumably denotes a balance between the amount of heat removed by surface and heat flux kept constant by the source. Differently for wall temperature curves, in no case there is achievement of an equilibrium value, except for the lowest flow rates of 6 ml/min and 12 ml/min. Also from raw data is clear the influence of flow velocity on water and wall temperature. The increase of the flow rate modifies the final temperatures reached by water and cooled surface. The results show that, as the flow rate increases, the amount of heat transferred to the water between the inlet and outlet is reduced, due to a shorter travel time of the cooling fluid inside the device. On the other hand, the heat removed by surface increases due to a more frequent replacement of heated fluid with a lower temperature fluid. Moreover, for flow velocities greater than 1 m/s (60 ml/min), in all cases the curves are very close to each other and it is not possible to appreciate significant differences between final temperatures. In appendix A.4 the final temperatures reached by cooling fluid and wall for all configurations are listed.

One further remark concerns the oscillations of measured values which are observed in all flow rates, especially in the lower ones. These oscillations are due to local evaporation phenomena inside the channel induced by "hot spots" present along the fluid path, *e.g.* microscopic surface roughness. Other causes such as air introduced by syringe pump have been rejected because the system is closed and isolated from the external environment. The generation and detachment of bubbles leads to a temporary alteration of recorded temperature of the wall and fluid because of a temporary two-phase condition of the cooling fluid. Bubbles generation is very relevant in two out of six geometries studied: the straight channel and parallel channels type-I cells. In the

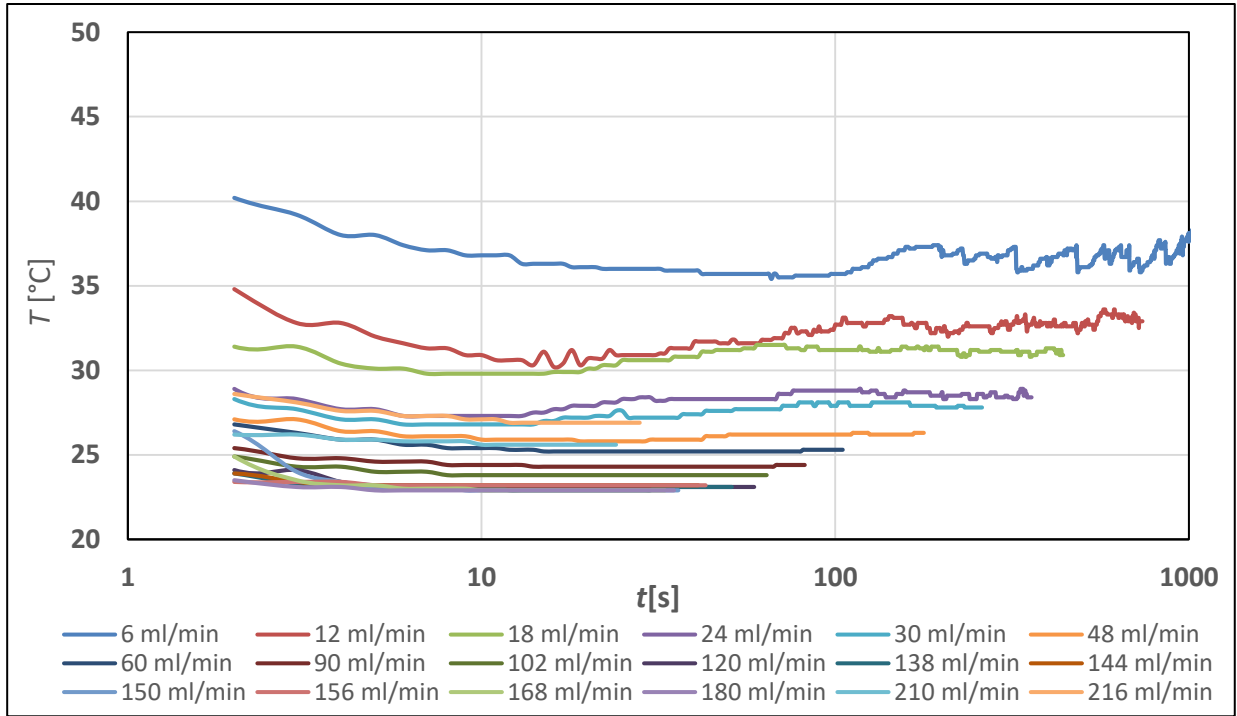


Figure 35: Water temperatures as a function of time [s] and flow rate [ml/min] for the straight channel cell at 50 °C.

straight channel the generation of bubbles is enhanced by limited cooling capability of this geometry that leads to a continuous formation of bubbles in correspondence of “hot spots”. A similar problem is also present for the parallel channels cell type-I. Indeed, in those channels characterized by a low percentage of flow rate the surface is less cooled and the formation of bubbles is encouraged, in addition being the flow in these channels very low, it is not able to push away any bubbles that could obstruct the passage and reduce the heat exchange surface. An example of influence of local evaporation on temperature measurements is shown in the following figure, where the water temperature curves for the straight channel with a source temperature of 50 °C are shown. The uncertainty given by this phenomenon on temperature measurements is taken into account in the error related to the extrapolation and interpolation analytical model applied to raw data. By temperature data of outlet water for the parallel channels cell type-I, a comparison between the classic configuration (plexiglass top and

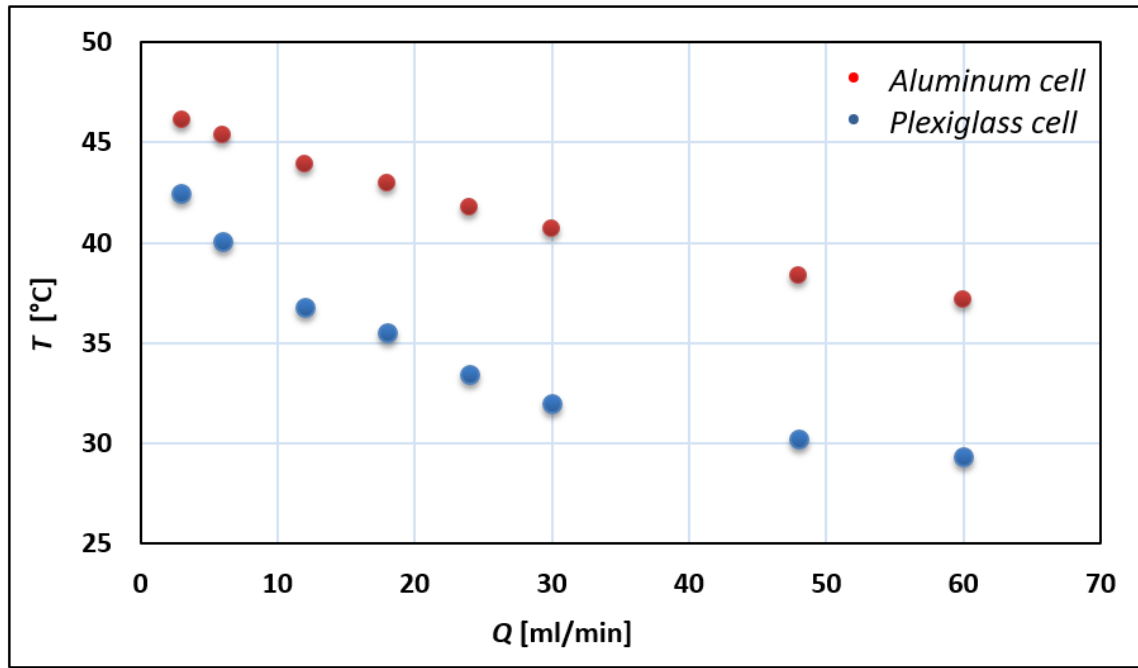


Figure 36: Outlet water temperatures as a function of flow rate [ml/min] for the parallel channels cell realized in plexiglass and aluminum at 50 °C.

aluminum bottom) and the variation totally in aluminum is performed in order to evaluate the effect of the material on the heat exchange properties of device. In Figure 36 the measured temperature for both configurations are compared. Looking at the plotted values the cell made totally in aluminum shows considerably higher temperatures of outlet water than the counterpart for all set flow rates, suggesting an over-heating of fluid along the channel path because of fact that all channel walls are affected by heat exchange. A limited volume of fluid inside micro-channel and a greater heat exchange surface lead to a significant reduction of the temperature gradient between cooling fluid and wall reducing the efficiency of heat transfer. Therefore, these preliminary results highlight the greater heat transfer capability of a micro-device realized in adiabatic and conductive material, that together with an easier implementation on existing engineering applications, make this solution an interesting alternative to the conventional micro-heat exchangers made totally in a conductive material.

4.2 Temperature extrapolated data

To determine the equilibrium temperature reached by fluid and wall after a time equal to 1400 sec., the interpolation and extrapolation analytical model of temperature described in appendix A.1 is applied. It is useful to remember that the maximum extrapolation time of 1400 sec. is assessed on the basis of lowest flow rate of 6 ml/min, which reaches the final equilibrium temperature in the emptying time of syringe. Also in this case, an example of the application of mathematical model to raw temperature data of water and wall for standard serpentine cell is given.

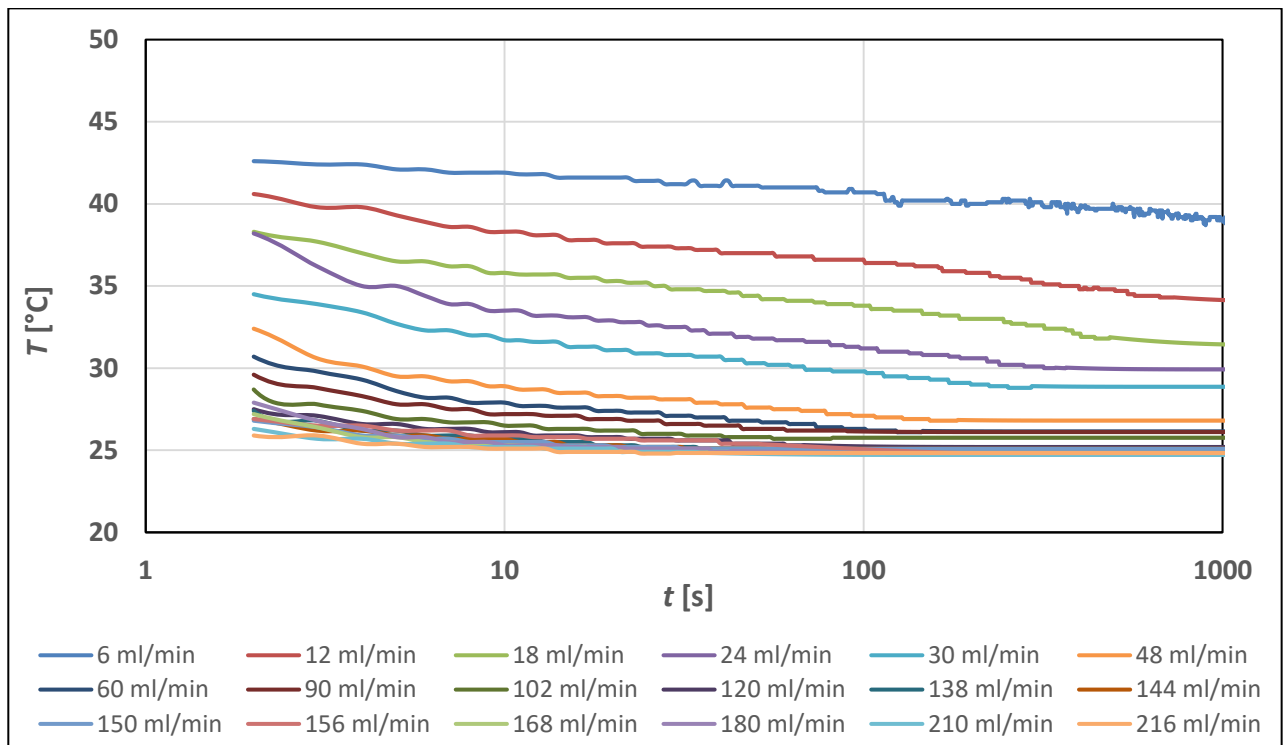


Figure 37: Extrapolated water temperatures as a function of time [s] and flow rate [ml/min] for the standard serpentine cell at 50 °C.

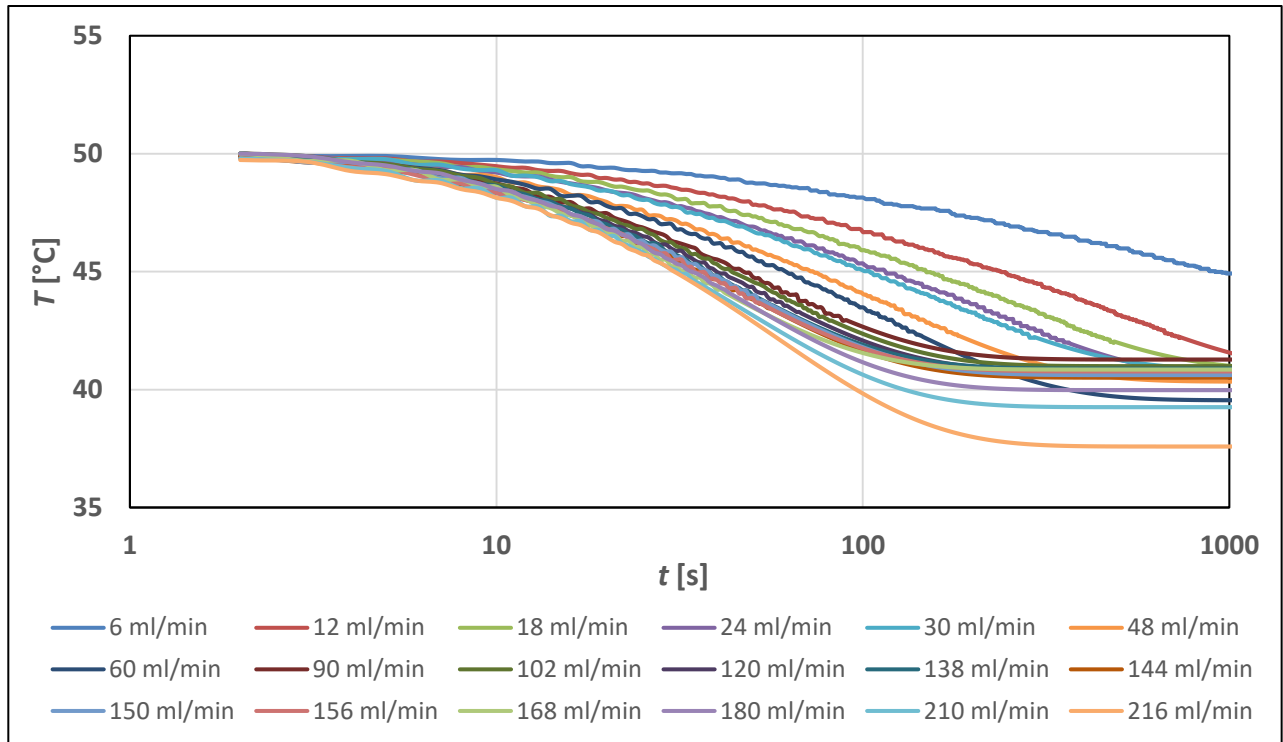


Figure 38: Extrapolated wall temperatures as a function of time [s] and flow rate [ml/min] for the standard serpentine cell at 50 °C.

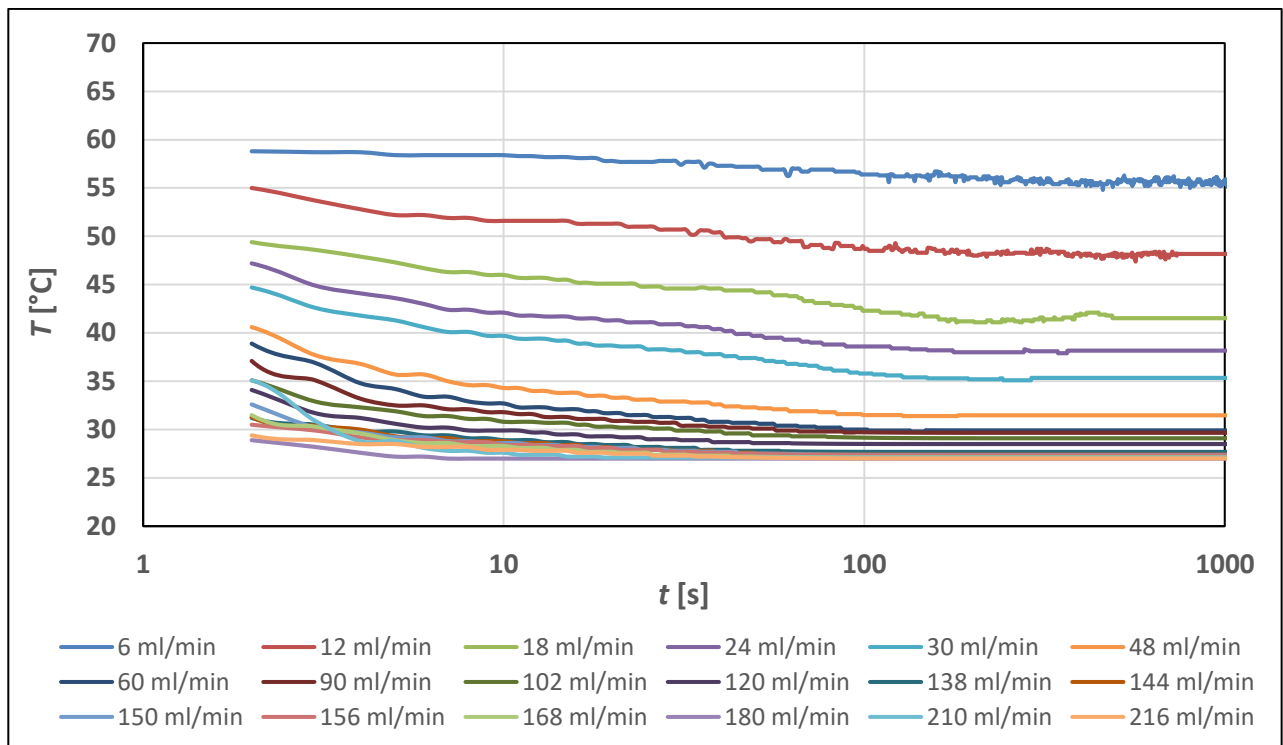


Figure 39: Extrapolated water temperatures as a function of time [s] and flow rate [ml/min] for the standard serpentine cell at 70 °C.

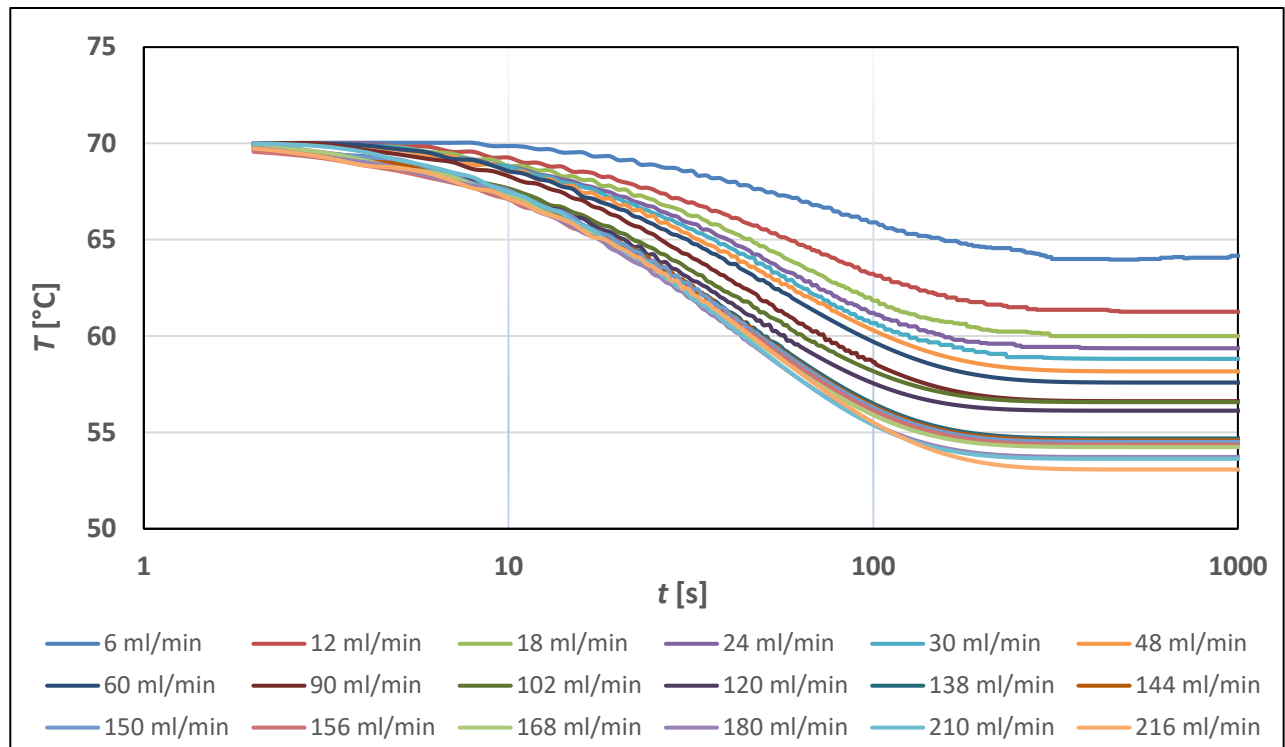


Figure 40: Extrapolated wall temperatures as a function of time [s] and flow rate [ml/min] for the standard serpentine cell at 70 °C.

For all fluid measurements, the extrapolation values predicted by model are a natural extension of plateau already reached by temperature data, ensuring a coherence between curves and a compliance with the trend obtained for raw data. The same coherence and compliance is maintained also for most of wall measurements, but sometimes the model is not always able to maintain a correct order between predicted trends. Because, in disagreement with raw data, it incorrectly predicts a growing temperature with flow rates with a consequent overlap between curves as shown in Figure 38.

The final temperature values obtained for fluid and wall with indication in red of relevant anomalous values provided by analytical model are shown in appendix A.5. The error in the extrapolation process, especially with higher flow rates, is due to a limited database of raw data available for least squares interpolation and a wall temperature far from being in equilibrium

condition. Both causes don't allow the model to correctly determine the temperature trend, thus leading to an overestimation of the equilibrium values with reference to the expected trend. The problem of this incorrect modeling of raw data was solved with the collaboration of A. Dermanis [40], who proposed to apply the least squares interpolation simultaneously to all flow rates in such a way as to relate them to each other. In other words, to evolve the physical model expression in order to take into account its dependence on time (t) and fluid velocity (v), so as to treat velocity as a physical boundary condition to be imposed on system. The model it has been rewritten as a system of four equations with 8 variables function of time and velocity:

$$\begin{cases} T(t, v) = a(v) \cdot e^{-b \cdot t^{d(v)}} + c(v) \\ a(v) = a_1 \cdot e^{-a_2 \cdot v} + a_3 \\ d(v) = d_1 \cdot v + d_2 \\ c(v) = c_1 \cdot e^{-c_2 \cdot v} + c_3 \end{cases} \quad (44)$$

where $a_{1,2,3}$; $d_{1,2}$ e $c_{1,2,3}$ are new constants to be determined with a least squares interpolation applied simultaneously to all flow rates. With this new mathematical model it is possible to correctly determine the equilibrium wall temperatures even at highest flow rates, as shown in the following figure, where the new trends obtained for standard serpentine are reported as example:

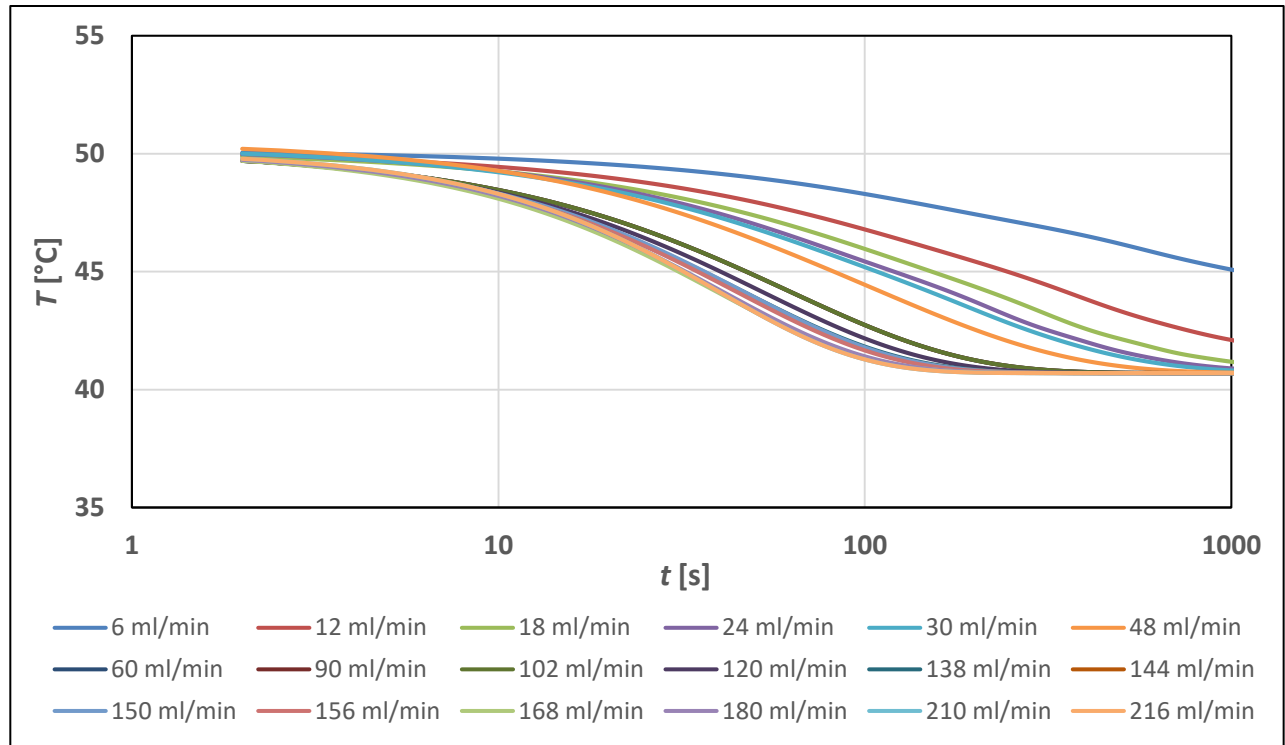


Figure 41: New extrapolation of wall temperatures as a function of time [s] and flow rate [ml/min] for the standard serpentine cell at 50 °C.

4.3 Thermal measurements results

On the base of fluid and wall equilibrium temperatures, the *Nusselt number* is calculated for each configuration and flow rate studied as described in Chapter 3, to explore and compare the thermal performances of micro-channels here proposed. The heat exchange efficiencies are evaluated by means of the *Nusselt-Reynolds* diagram by keeping in mind the physical meaning of *Nusselt number* and its link with the *Reynolds number*. Before comparing the thermal results, the measurement system and the calculation model are validated by comparing the *Nusselt* values calculated for the straight channel with values available in literature. In particular, the match is made with results shown in the works of P. Lee and S.V. Garimella, concerning heat exchange in rectangular straight micro-channels in a condition of constant heat flux of 0.45 W/mm² [41], [42]. Figure 42 shows an example of matching for the results obtained at 50 °C.

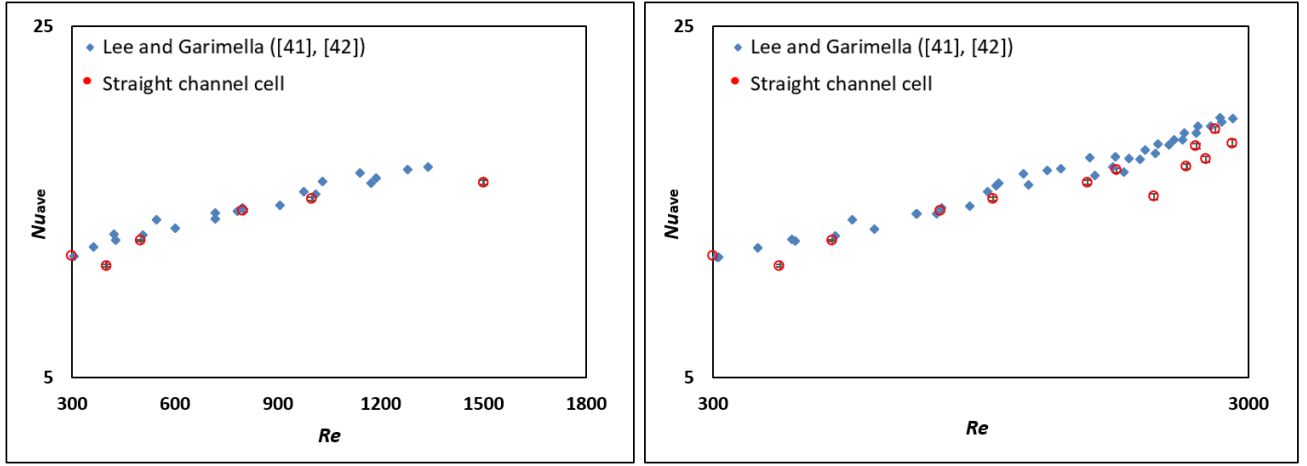


Figure 42: Comparison of the Average Nusselt numbers as a function of the Reynolds number obtained for straight channel cell at 50 °C with the results proposed by Lee and Garimella [41], [42].

A similar result is obtained for a source temperature of 70 °C. The good agreement between data in a wide range of *Reynolds numbers* ($300 < Re < 3000$) states the accuracy of the methodology applied and ensures the validity of conclusions deduced by comparison of *Nusselt numbers* among other configurations. A first comparison is reported in Figure 43 (hot source temperature of 50 °C) and Figure 44 (hot source temperature of 70 °C) that show the *Nusselt number* as a function of *Reynolds number* for three micro-cells: parallel channels type-II, standard serpentine and wavy-sinusoidal serpentine cells, with error bars and together with the classical correlation proposed by Sieder & Tate [39]. The error analysis results will be discuss in the following paragraph. In the inset the *Nusselt* values for $1000 < Re < 5000$ are highlighted to better show the trend of the curves in the turbulent regime.

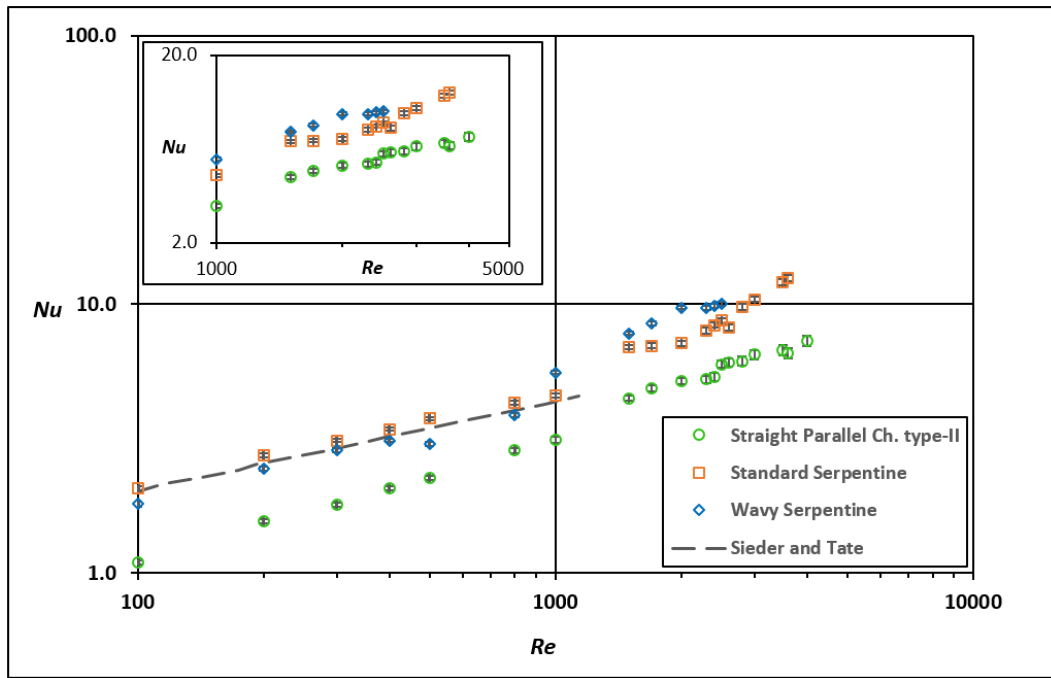


Figure 43: Comparison of the Average Nusselt numbers as a function of the Reynolds number obtained for the three tested micro-cells at 50 °C with the classical correlation proposed by Sieder & Tate [39].

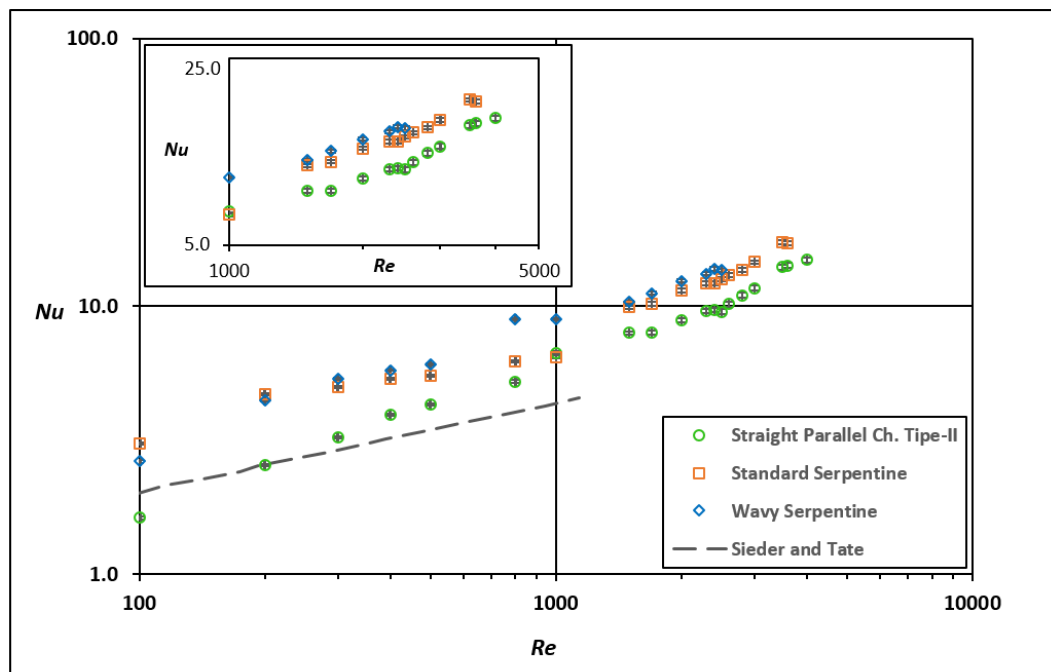


Figure 44: Comparison of the Average Nusselt numbers as a function of the Reynolds number obtained for the three tested micro-cells at 70 °C with the classical correlation proposed by Sieder & Tate [39].

In order to give comments on the relative heat exchange performance of the tested micro-cells, it is important to remind that convective motions, as far as heat transfer is concerned, provide much better transfer of energy across the flow thanks the additional intense mechanism of heat transfer in the radial and azimuthal directions [38]. Being *Nusselt number* a measure of heat flux due to convection, larger *Nusselt* values suggest a most efficient heat transfer given by the device. Looking at Figure 43 and Figure 44, it is immediately noticeable that both cells with serpentines (standard and wavy) show larger *Nusselt numbers* than those of the parallel channel configuration, for a given *Reynolds number*. Moreover, *Nusselt number* increases with *Reynolds number* with a power-law with exponent around 0.5 for all geometries, in agreement with theoretical predictions and Sieder-Tate empirical law [39] shown for laminar flow in Eq. 43. By the physical meaning of *Nusselt number*, the impact of geometry and flow regime on convective motions is clearly shown in this plot. Especially for a hot source temperature of 70 °C the serpentine with wavy channel attains the highest values of *Nusselt number* for several *Re* values, suggesting that this geometry allows the most efficient heat transfer, only slightly lower values being obtained for the standard serpentine. On the other hand, the results for the parallel channel configuration show less efficiency, the reasons for all these behaviors must be still detailed through the μ PIV analysis. Considering also the different flow regimes, it is possible to observe in both figures only a small change in slope when moving from laminar to turbulent regimes. Presumably, this is a consequence of using a non-classical channel shape, whereas the empirical laws are tuned for strictly linear circular section micro-channels. Therefore, for both hot source temperatures, it seems that the largest differences among the tested geometries are attained in laminar conditions, whereas they are less pronounced in the turbulent regime, not in agreement with Sieder-Tate suggestions [39]. This could be given to the fact that the serpentine configurations in comparison to parallel channels could promote flow acceleration and recirculation already in laminar conditions, and that these differences would be attenuated in

fully established turbulence. The most evident results obtained for a set hot source temperature of 70 °C are due to a larger temperature gradient between fluid and wall. With a fixed inlet flow temperature of 21 °C the temperature gradient between fluid and surface is just under 30 °C for a set hot plate temperature of 50 °C, while it is around 50 °C for a set temperature of 70 °C.

A similar discussion could be done by observing curves in Figure 45 (hot source temperature of 50 °C) and Figure 46 (hot source temperature of 70 °C) that show the *Nusselt number* as a function of *Reynolds number* for the standard serpentine cell with ribs and the standard serpentine tested with two different solutions of water and glycerin. Both compared with the standard serpentine cell tested with distilled water. The *Nusselt* values are shown with error bars and together with the classical correlation proposed by Sieder & Tate [39]. In the inset the *Nusselt* values for $1000 < Re < 5000$ are highlighted to better show the trend of the curves in the turbulent regime.

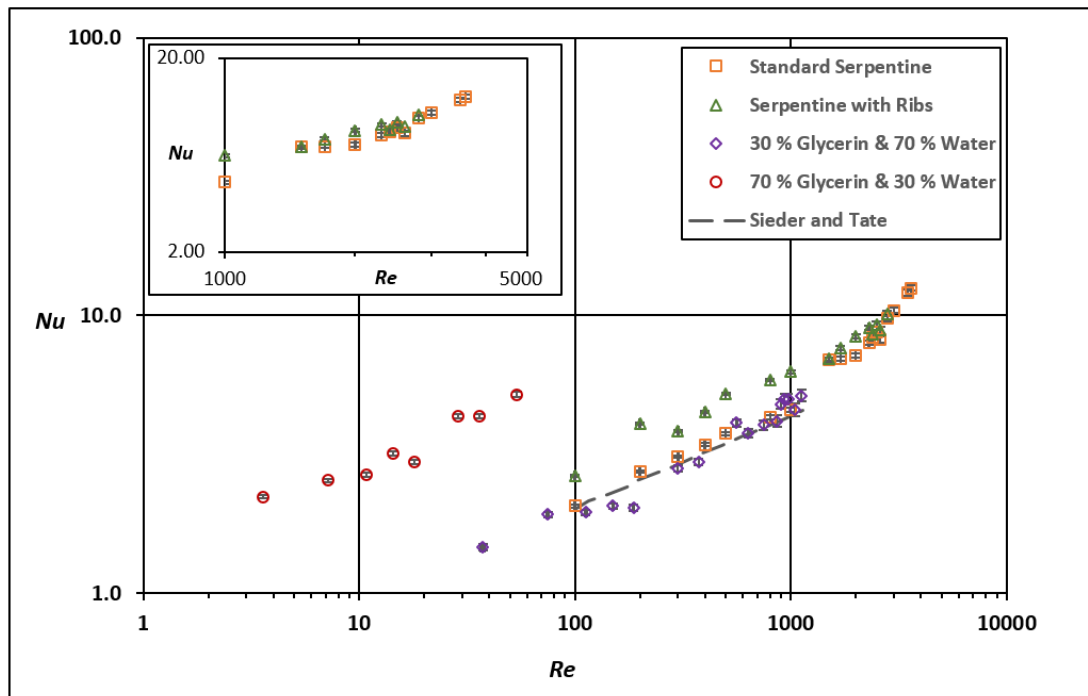


Figure 45: Comparison of the Average Nusselt numbers as a function of the Reynolds number obtained for the four tested micro-cells at 50 °C with the classical correlation proposed by Sieder & Tate [39].

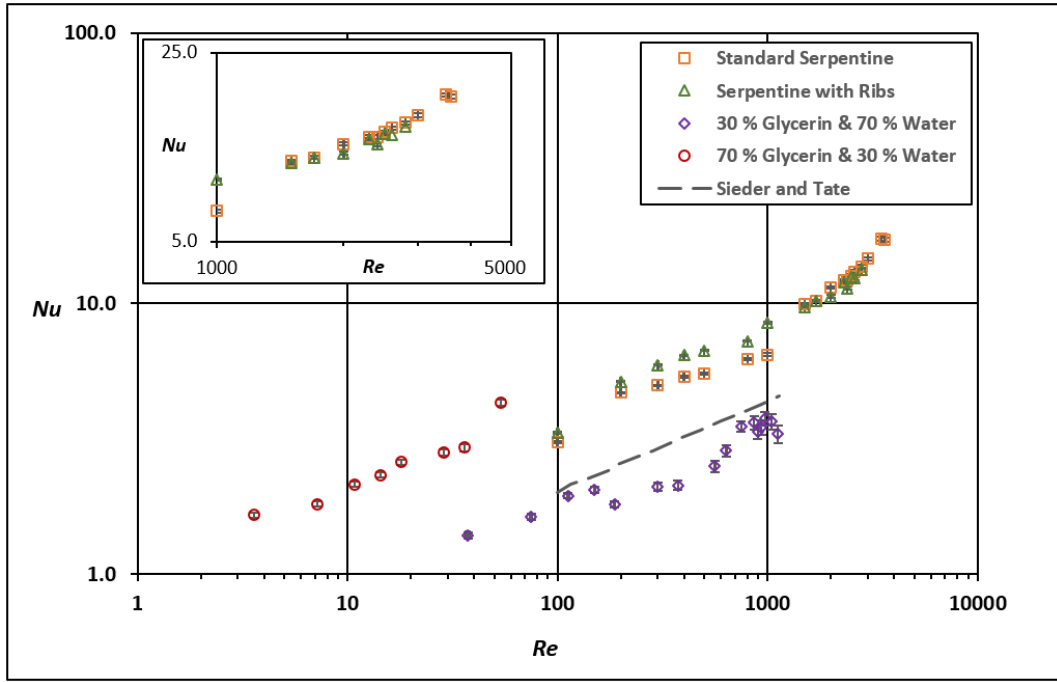


Figure 46: Comparison of the Average Nusselt numbers as a function of the Reynolds number obtained for the four tested micro-cells at 70 °C with the classical correlation proposed by Sieder & Tate [39].

Starting by serpentine cell with ribs, for both source temperatures, it could be seen how the insertion of horizontal elements along the path brings to higher *Nusselt* values than those of the standard serpentine cell without ribs, for a given *Reynolds number*. The reason could be a combination of a greater heat exchange surface and a larger convection motion due to cross-section variation along the channel path. Thinking about the law of conservation of mass, the partial obstruction of channel cross-section due to the thickness of rib increases the local fluid velocity ensuring a greater heat exchange. Despite the potential of such cell, the serpentine channel tested with a solution of 30 % water and 70 % glycerin seems to attain the highest values of *Nusselt number*. Even if it is not possible to make a direct match for a given *Reynolds number* due to different viscosity, the trend of available values suggests the capability of this different cooling fluid to allow the most efficient heat transfer also considering the previous discussion about the wavy-sinusoidal channel. On the other hand, the results for the serpentine

cell tested with a solution of 70 % water and 30 % glycerin show a lower efficiency, also in this case all these behaviors must be still detailed through the μ PIV analysis. Looking at the curves development it is possible to notice some details already seen in the previous comparison. For example a *Nusselt number* that increases with *Reynolds number* with a power-law with exponent around 0.5 for all configurations, in agreement with theoretical predictions and Sieder-Tate empirical law [39]. Moreover, also the small change in slope when moving from laminar to turbulent regimes seems to be confirmed. Lastly, unlike water, the *Nusselt numbers* calculated for glycerin solutions appear to be strongly affected from the system's reference temperatures, showing much wider variations than other micro-cells between the two source temperatures. This could be a consequence of the different thermal properties of glycerin, especially of a lower specific heat than that of water (glycerin: $2.39 \frac{\text{kJ}}{\text{kg}\cdot^{\circ}\text{C}}$ at 20 °C; water: $4.186 \frac{\text{kJ}}{\text{kg}\cdot^{\circ}\text{C}}$ at 20 °C) which implies a great sensitivity to limited temperature variations.

4.4 Error analysis results

In *Nusselt-Reynolds* graphs for each value the error bars along the x and y axis are reported to give an idea of uncertainties related to parameters, evaluated on the basis of formulas presented in appendix A.2. To determine the error propagated on the *Reynolds number*, the quantity to be considered is the volumetric flow rate \dot{Q} , set on the syringe pump and used to calculate the bulk velocity. Since the flow rate error is given only by the uncertainty relating to the setting of flow rate value on syringe pump (equal to ± 0.05 ml/min), for all devices tested with water the error value on *Reynolds* is assessed around ± 0.83 %. In case of solution with 70 % water & 30 % glycerin the error on *Reynolds* is ± 0.31 % due to different properties of fluid and equal to ± 0.03 % for the solution with 30 % water & 70 % glycerin. Differently from *Reynolds number*, the uncertainty on *Nusselt number* is a function of the micro-cell type considered. In fact, being

Nusselt a function of the fluid temperature at the outlet of the channel and the wall temperature, it is affected by different errors depending on geometry and set flow condition. The error in the outlet temperature and wall is given by two factors. The first is the uncertainty related to the mathematical model applied for the interpolation of the experimental data and the extrapolation of the equilibrium temperature. The second is the error of the measuring system. In the following figures the plots of error associated with the *Nusselt number* (ΔNu) as a function of *Reynolds number* are shown for each micro-device.

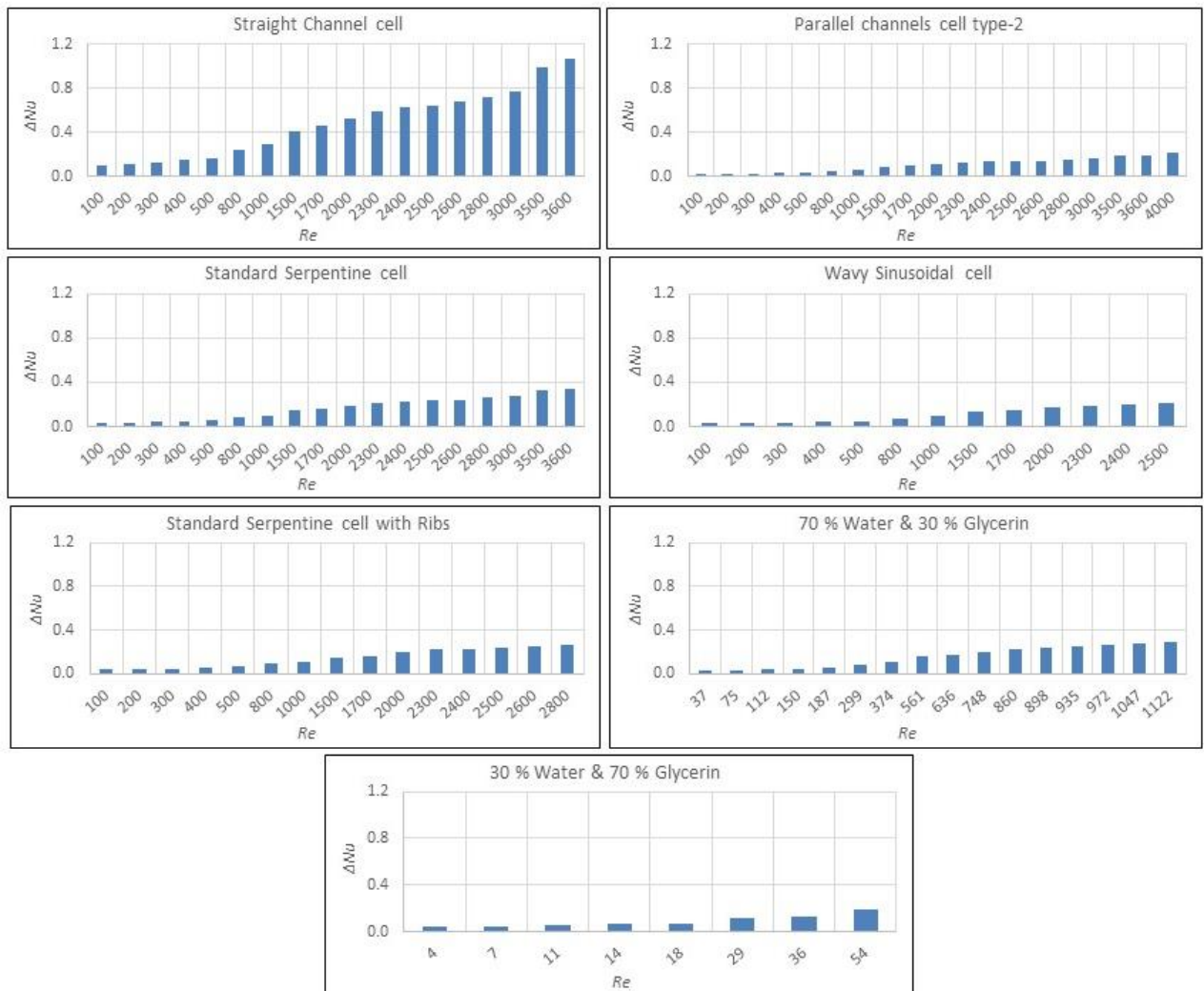


Figure 47: Error on Nusselt number (ΔNu) as a function of Reynolds number for all cells at 50 °C.

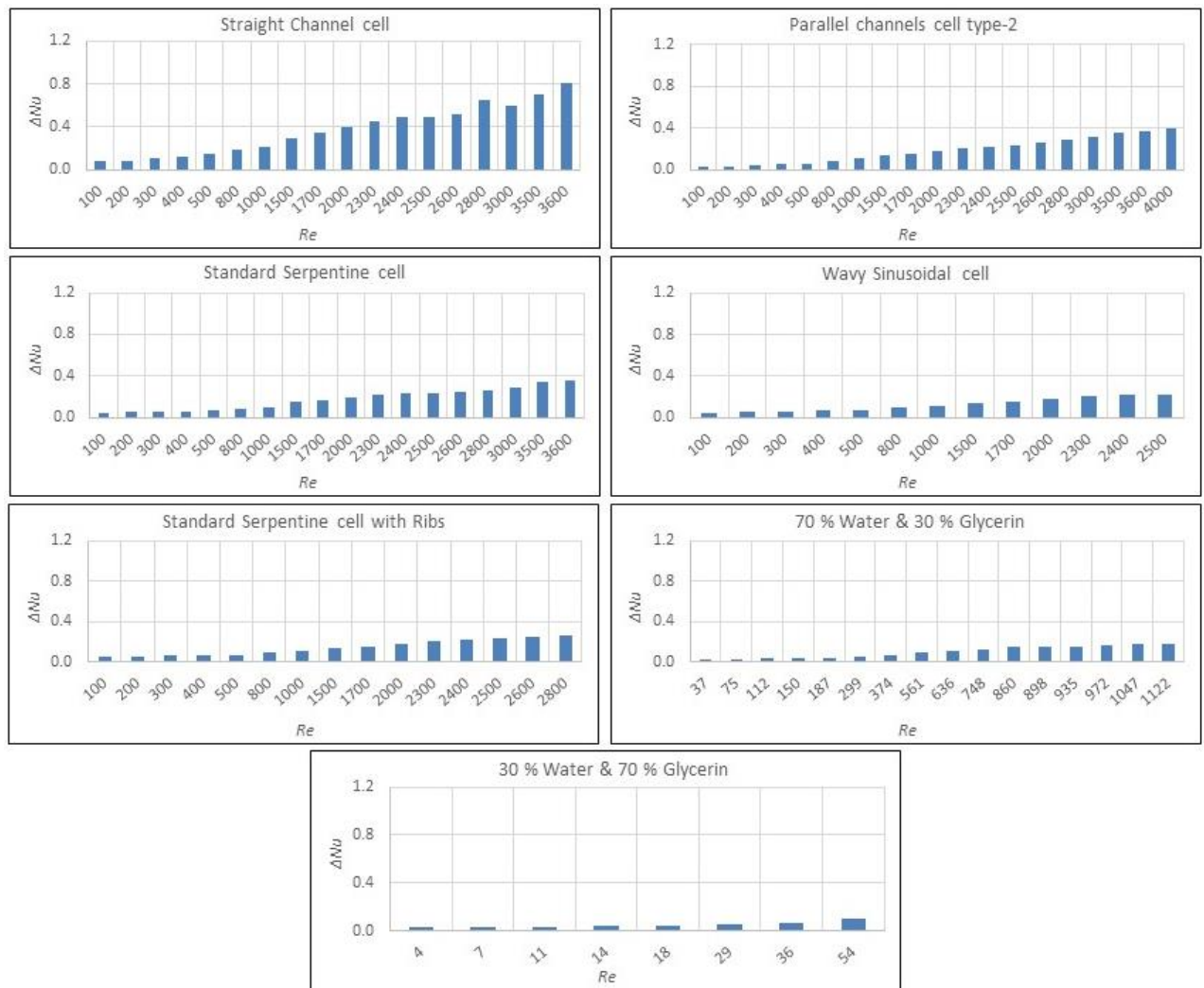


Figure 48: Error on Nusselt number (ΔNu) as a function of Reynolds number for all cells at 70 °C.

By Figure 47 and Figure 48 is clear that in all cases the high flow rates have a much greater uncertainty than lower flow rates. For example, the highest value of ± 1.07 % is obtained for straight channel cell for a flow rate of 216 ml/min with a source temperature of 50 °C. This large divergence is given to the fact that for flow rates greater than 60 ml/min the available database as input of mathematical model becomes very small, due to a short exhaustion time of the 140 ml syringe, with a consequent increase of error in the prediction of equilibrium temperature. Among all devices, the straight channel micro-cell shows for both temperature conditions the highest error for a given flow rate because of local evaporation phenomenon. As already mentioned, the straight channel is the most sensitive geometry to this phenomenon and the high

uncertainty on the model reflects the strong temperature oscillations recorded by thermocouples due to a considerable generation of bubbles inside the channel. For straight channel the errors fall in a range of 0.01-1.01 %, while all other devices have low values included in a range of 0.01-0.4 %. A last observation can be made by comparing errors trends plotted at different hot source temperatures. The lowest error relative to measurements at 70 °C could be for a larger temperature gradient between fluid and wall temperature which allows to have well-defined temperature trends that reduces the uncertainty related to analytical model solutions.

Chapter 5 – Fanning Friction Factors and Efficiencies

The counterpart of a high heat transfer efficiency due to larger convective motions is the establishment of an increasing pressure drop along the axial flow direction, encountered also in case of use of water-glycerin solutions because of a high fluid viscosity. Thus, aiming to evaluate an effective heat exchange efficiency parameter for each micro-device, pressure losses are evaluated in terms of the *Fanning factor*, as introduced in chapter 2. The experimental results for pressure drops and the relative friction factor are reported respectively in Figure 49, Figure 50 and Figure 51.

The relative pressure losses measured for each micro-cell in a range of flow rates from 6 ml/min to 102 ml/min in accordance with working range of pressure sensor, have a slightly non-linear trend, in agreement with expectations ([43], [44], [45]). Results are quite similar for the parallel channels and the standard serpentine cells, while reaching a value more than 1.5 larger for the standard serpentine configuration tested with a solution of 70 % water and 30 % glycerin, 2.5 larger for the wavy configuration, 3 times larger for serpentine with ribs cell and up to a maximum of 5 times larger for the standard serpentine configuration tested with a solution of 30 % water and 70 % glycerin. For the wavy and the serpentine with ribs cells, the geometry is the main cause of such values of pressure losses.

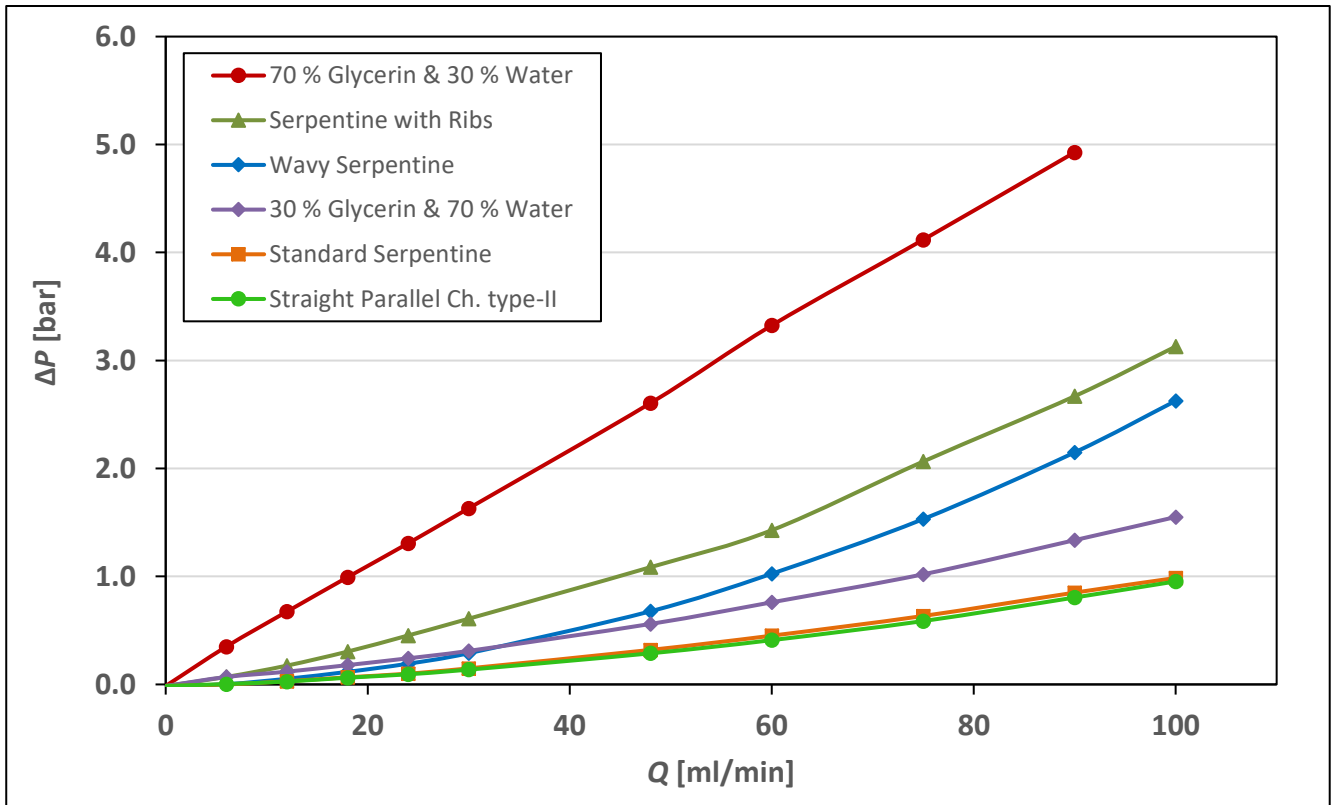


Figure 49: Relative pressure-drop as a function of flow rate [ml/min] for the tested micro-channels.

The wavy configuration, due to the series of bends, implying a continuous inversion of flow direction, increases a lot the pressure losses, presumably due to the presence of recirculation regions both in laminar and turbulent conditions. Different phenomenon occurs in the serpentine with ribs, where the cylindrical steel elements, diameter of 0.4 mm and length of 17 mm, fixed along duct axis at the middle of the channel are obstacles to the fluid flow, implying pressure losses higher than those produced by wavy serpentine. Moreover, the continuous variation of cross-section size induces three-dimensional motions in correspondence of ribs edges that increase the pressure drop along the channel path. On the other hand, the parallel channel and standard serpentine cells retain long linear sections, which give mainly distributed pressure losses, so far much lower than the local head losses due to bend, obstacles and changes in cross-sections. With regards to serpentine cell tested with water-glycerin solutions, pressure measurements reflect clearly the greater viscosity of fluids than water. Especially for the solution

with 30 % water and 70 % glycerin the very high viscosity equal to $0.033 \frac{\text{Ns}}{\text{m}^2}$ dominates long linear sections losses in standard serpentine, positioning itself above all other curves with the highest pressure drops for a given flow rate. The effects of a larger fluid viscosity are more moderate for the solution with 70 % water and 30 % glycerin ($0.002 \frac{\text{Ns}}{\text{m}^2}$), showing pressure losses higher than standard serpentine tested with water, but still below the values measured for the wavy geometry.

Looking at curves shown in Figure 50 and Figure 51, it is possible to observe a change of trend that brings the parallel channels cell on top, with the highest friction factors than other micro-cells. In detail, Figure 50 and Figure 51 show friction factors as a function of *Reynolds number* for all micro-cells considering a hot source temperature of 70 °C, together with the classical correlation proposed by J.T. Fanning [46] for rectilinear pipe. For a source temperature of 50 °C the results are very similar.

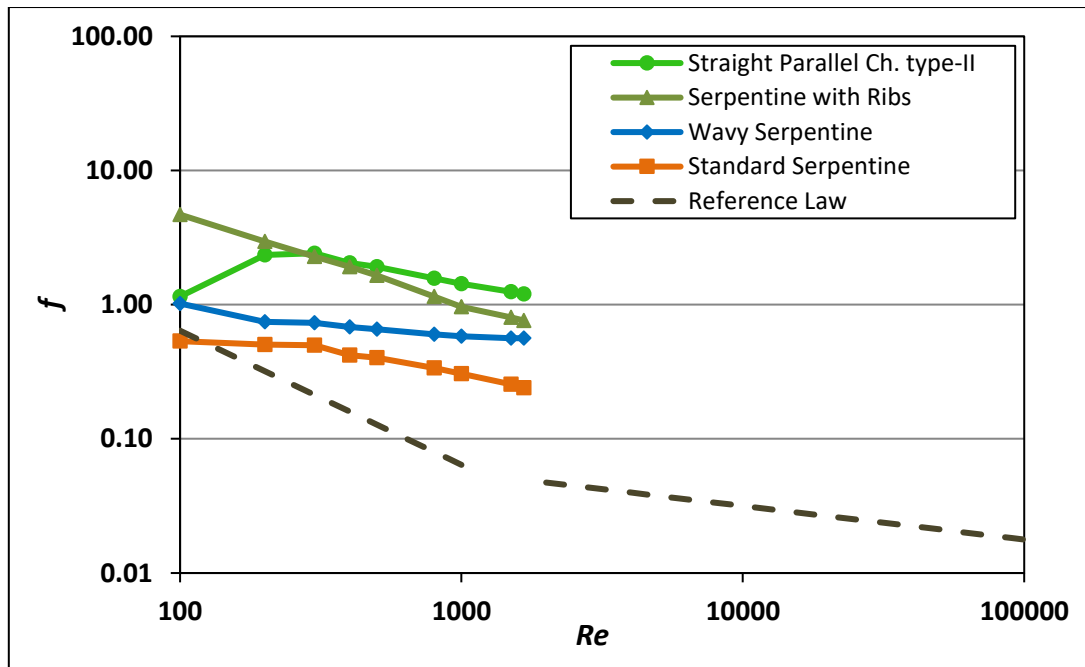


Figure 50: Fanning friction factor (f) as a function of Reynolds number for the tested micro-channels at 70 °C: parallel channels, standard serpentine with and without ribs, wavy-sinusoidal serpentine, with the classical correlation proposed by J.T. Fanning [46].

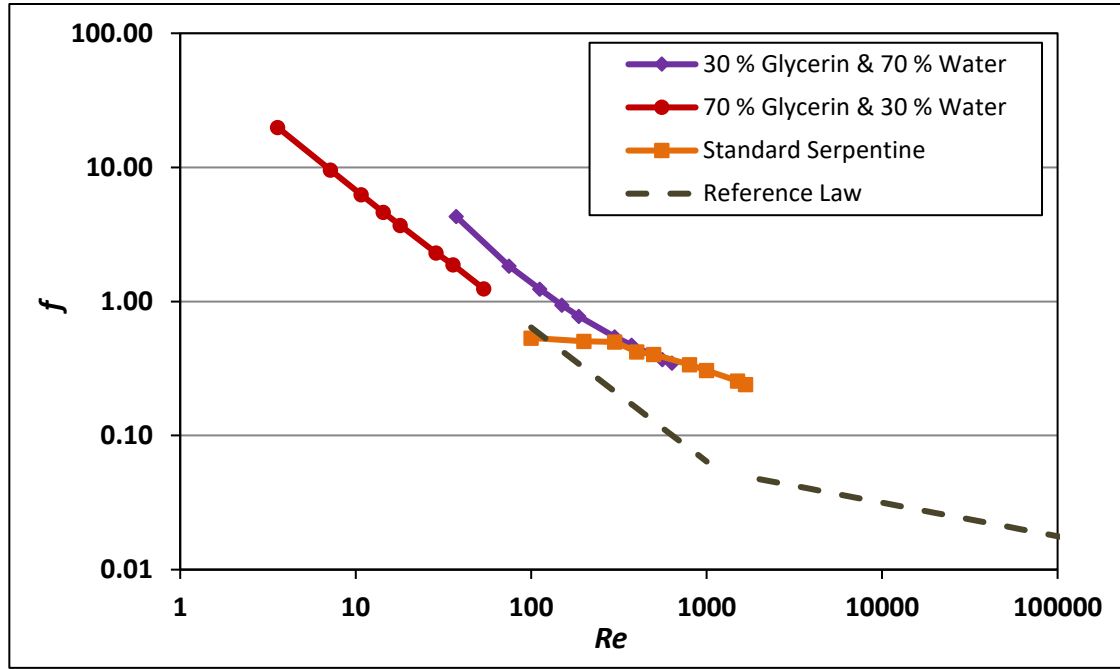


Figure 51: Fanning friction factor (f) as a function of Reynolds number for the tested micro-channels at 70 °C: standard serpentine tested with water and water-glycerin solutions, with the classical correlation proposed by J.T. Fanning [46].

To understand the new curves arrangement, it is important to remember that to evaluate the *Fanning factor*, it is necessary to compute the hydraulic diameter and the equivalent length for each micro-cell in accordance with Eq. 25. As reported in the following table, the first of such quantities is the highest and the second is the lowest for the parallel channels configuration.

Channel Type	Channel eq. length L [mm]	Dh [mm]
Straight Parallel Channels type-II	101	2
Standard Serpentine	296.5	1
Standard Serpentine with ribs	296.5	1
Wavy-Sin. Serpentine	354	1

Table 20: Geometrical parameters of the tested micro-cells.

Therefore, in Figure 50, the factor for the parallel channels cell is much higher than that for the other geometries. The serpentine with ribs still getting higher non-dimensional losses in comparison to the wavy and standard serpentine, that still getting lowest values, because they have comparable length and hydraulic diameter. The factor trends shown in Figure 50 are far from friction values encountered in a rectilinear pipe (this is reported in dotted lines in both figures), presumably also in this case, due to a non-classical channel shape that induces turbulent motion also in laminar conditions. On the other hand, as shown in Figure 51, the trends obtained for the serpentine tested with water-glycerin solutions are near to the reference law and decrease with *Reynolds number* with a power-law with the exponent around -1, in agreement with this. Due to a larger viscosity of these solutions than water, despite a non-classical channel shape, any flow acceleration and recirculation induced by geometry are suppressed, leading the factor values to be in line with those of a rectilinear pipe with flow in laminar conditions, especially for the solution with 30 % water and 70 % glycerin.

Looking always at Figure 51, also in this case the standard serpentine tested with a solution of 70 % water and 30 % glycerin confirms higher non-dimensional losses in comparison to the standard serpentine tested with water, in accordance with the pressure losses curves. On the other hand, the trend of the solution with 30 % water and 70 % glycerin seems to have very low non-dimensional losses, slightly higher than the lowest values obtained for standard serpentine. This paradox with reference to results given by pressure measurements is due to the fact that regardless of the *Reynolds number*, the *Fanning factor* is calculated on the base of bulk velocity determined directly from set flow rate and therefore equal for all configurations (Table 21). At the same time, in case of a water-glycerin solution, for a same flow rate a different *Reynolds number* is determined (Table 21) due to different values of viscosity and density, with the consequent that at same velocity values correspond to lower value of *Reynolds numbers*. Since

results are not compared under the same velocity conditions, it happens that for a given *Reynolds number*, a lower *Fanning factor* is related, leading to this apparent condition of having very low friction factors for the configuration with the highest pressure losses. It is important to highlight that even for the solution with 70 % water and 30 % glycerin the *Reynolds* values obtained are different due to different solution properties, but in this case they are still near to those obtained for water and therefore don't affect a lot the curve arrangement. In Table 21 *Fanning factors*, velocities and *Reynolds numbers* are compared.

Cooling Fluid: Distilled Water	Bulk Velocity U [m/s]	Re	Parallel Channels type-II	Standard Serpentine Ch.	Wavy-Sin. Serpentine Ch.	Serpentine Ch. with Ribs
Q [ml/min]			Fanning Factor	Fanning Factor	Fanning Factor	Fanning Factor
6	0.1	100	1.15	0.53	1.02	4.69
12	0.2	200	2.35	0.50	0.74	2.95
18	0.3	300	2.42	0.50	0.73	2.29
24	0.4	400	2.05	0.42	0.68	1.92
30	0.5	500	1.91	0.40	0.66	1.65
48	0.8	800	1.57	0.34	0.60	1.15
60	1.0	1000	1.43	0.31	0.58	0.97
90	1.5	1500	1.25	0.26	0.56	0.80
102	1.7	1700	1.20	0.24	0.56	0.76

Cooling Fluid: 30 % Glycerin- 70 % Water	Bulk Velocity U [m/s]	Re	Standard Serpentine Ch.
Q [ml/min]			Fanning Factor
6	0.1	37	4.30
12	0.2	75	1.84
18	0.3	112	1.24
24	0.4	150	0.94
30	0.5	187	0.77
48	0.8	299	0.54
60	1.0	374	0.47
90	1.5	561	0.37
102	1.7	636	0.35

Cooling Fluid: 70 % Glycerin- 30 % Water	Bulk Velocity U [m/s]	Re	Standard Serpentine Ch.
Q [ml/min]			Fanning Factor
6	0.1	4	19.89
12	0.2	7	9.56
18	0.3	11	6.25
24	0.4	14	4.63
30	0.5	18	3.70
48	0.8	29	2.30
60	1.0	36	1.88
90	1.5	54	1.24
102	-	-	-

Table 21: Bulk Velocities, Reynolds numbers and Fanning factors at 70 °C.

5.1 Efficiency parameter

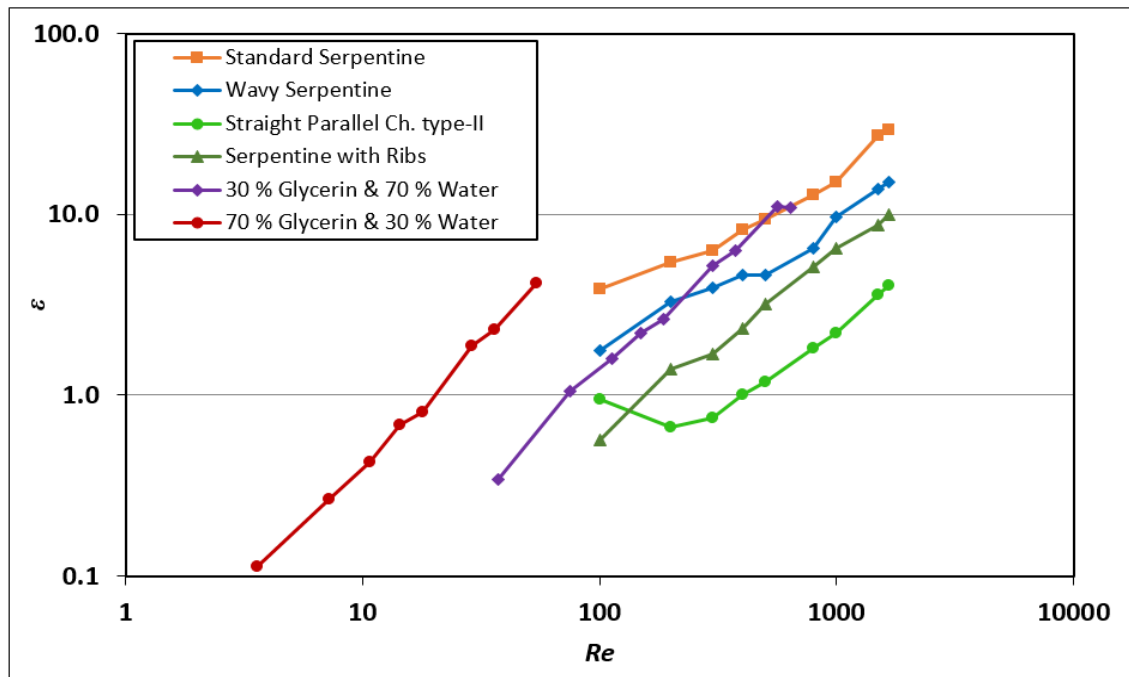


Figure 52: Comparison of the efficiency parameters as a function of Reynolds number for the three tested micro-cells at 50 °C.

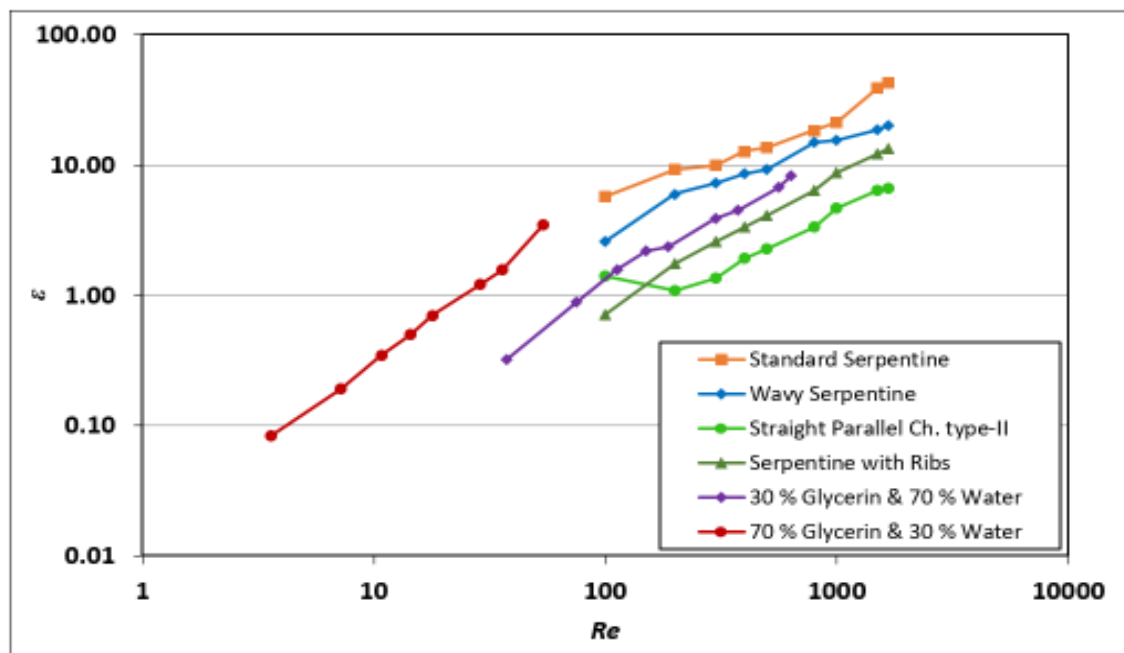


Figure 53: Comparison of the efficiency parameters as a function of Reynolds number for the three tested micro-cells at 70 °C.

The evaluation of efficiency (ϵ) is performed by relating the average *Nusselt number* to the *Fanning factor* according to the definition given in chapter 2 and results are shown in Figure 52 and Figure 53. The overall observation is that the standard serpentine micro-cell for both hot source temperatures attains the highest heat exchange efficiency regardless of flow regime, getting high *Nusselt numbers* combined with low pressure losses. This is due to a geometry assembled with a few right angles separated by long linear sections, thus allowing a net improvement in comparison to the parallel channels configuration, with a relative geometrical complexity which places it in last position with lowest efficiency values. On the other hand, the wavy serpentine geometry gets good performances, followed by serpentine with 70 % water and 30 % glycerin solution and serpentine with ribs, half a way between the standard serpentine and the parallel channels configuration. Looking at Figure 53, hot source temperature set to 70 °C, the highest values of *Nusselt number* attained by wavy serpentine cell, joined with its medium-high pressure drop, place this geometry in second place, with lower efficiency values than standard serpentine especially for *Reynolds* higher than 1000, where presumably the well-developed recirculation regions increase a lot the pressure losses. Differently, the low pressure losses shown by serpentine with 70 % water and 30 % glycerin solution brings it in third place, despite very low *Nusselt numbers*. Just above the parallel channels cell there is the serpentine with ribs, which sees its high *Nusselt number* values, very near to those of wavy and standard serpentine, penalized due to very high load losses.

In Figure 52, hot source temperature set to 50 °C, the results remain unchanged except for the serpentine with 30 % water and 70 % glycerin solution that goes above the wavy serpentine due to higher *Nusselt* values shown at this temperature for the same pressure losses. About the standard serpentine tested with a solution of 30 % water and 70 % glycerin, in both cases even if it is not possible to make a direct match for a given *Reynolds number*, the trend of available values suggests the capability of this configuration to allow very good performances, slightly

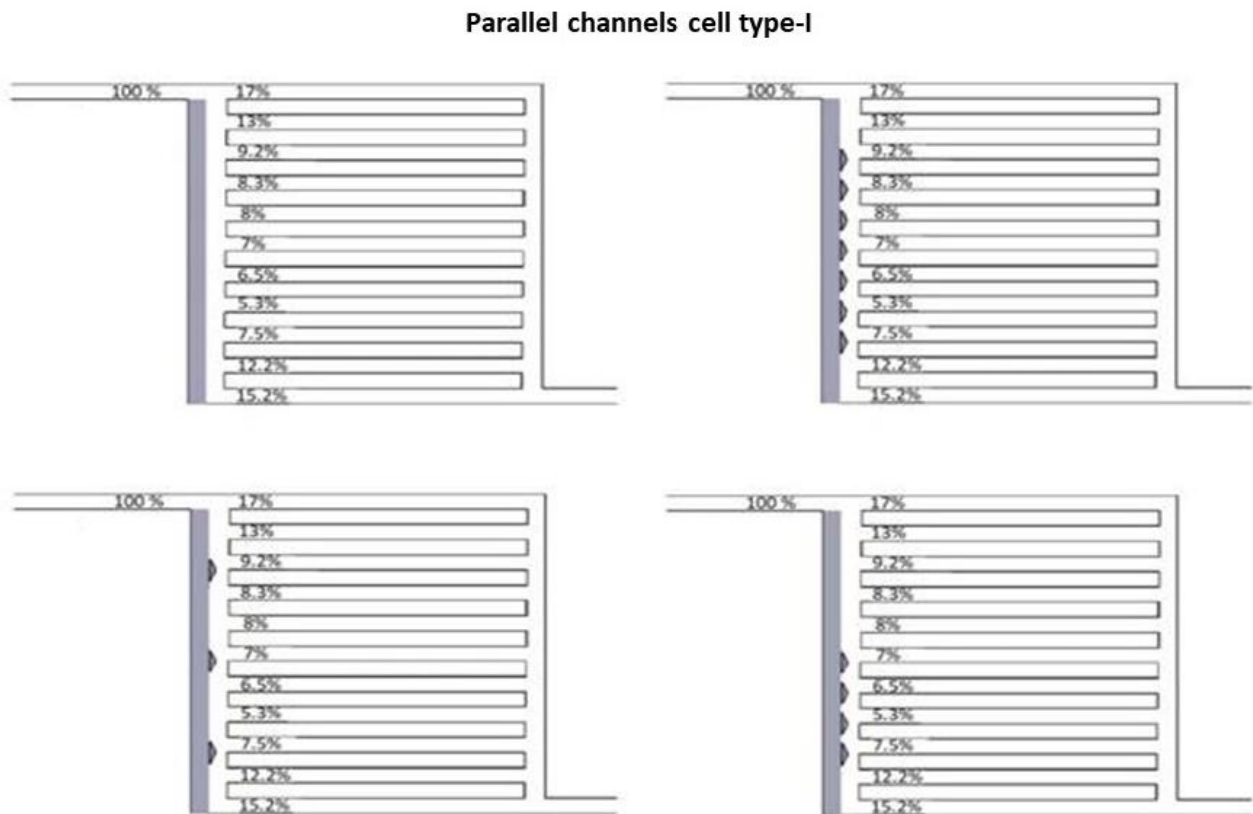
lower at 70 °C or slightly upper at 50 °C than those of standard serpentine. In the following chapter, μ PIV measurements are employed to detail the observed global heat exchange performances of each micro-cell configuration on the base of the local velocity field and fluid dynamics phenomena.

Chapter 6 - μ PIV Results

In this section, Particle Image Velocimetry, applied in accordance with some of the main references ([47], [48], [49]), is employed to characterize the velocity fields of the micro-cells previously analyzed on the $Nu-Re$ diagram and heat transfer efficiency point of view. This in order to correlate fluid dynamic and thermal fields, thus supporting the observed heat transfer properties by detailed velocity fields measured within the channels. Specifically, the μ PIV results will be shown for the straight parallel channels type-II cell to be considered as reference, standard serpentine, wavy-sinusoidal serpentine and the standard serpentine tested with glycerin solutions. For each case of study, images are acquired at two different flow rates: 30 ml/min and 90 ml/min, typical of the laminar regime, where the greatest differences between thermal results are observed. For both flow rates, the attention will be focused on local fluid recirculation and acceleration, as related to the specific geometry and to the different cooling fluid. In detail, the mean vector, magnitude, vorticity and entropy (as indicator of the local contribution to mixing and heat exchange) fields will be shown, together with the comparison of vertical profiles and the analysis of standard deviations (Std) for both velocity components u and v . It is important to underline that it was not considered necessary for purposes of the study to investigate in detail the vortical structures and three-dimensional motions occurring within the channels, at bend and curve locations. This because the aim of PIV measurements was to detail and support the thermal analysis results and to identify the causes of different heat exchange efficiencies.

6.1 Configurations selection for analysis

Among all micro-cells introduced in section 3.1 the straight channel and the serpentine with ribs aren't considered for the μ PIV analysis; because it was not possible to acquire reliable images that allow a correct comparison with other configurations, due to a too fast particles motion inside the channel. Also the parallel channels cell type-I isn't considered in this part of the study due to a not uniform distribution of flow inside the channels, as shown in Figure 54, even with the implementation of the fluid guide profiles. However, a net improvement in flow distribution was obtained with the parallel channels cell type-II, to be considered as a reference for the study, designed as an evolution of the previously type-I cell.



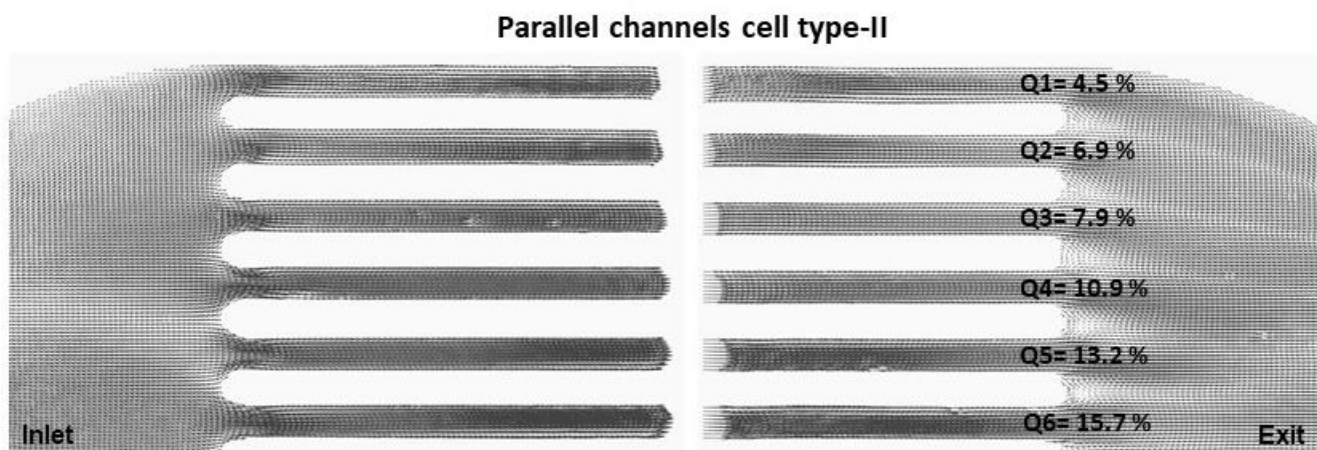


Figure 54: Flow distribution in the parallel channels cell type-I vs parallel channels cell type-II (inner and outer sections of the six first channels, Figure 55).

The analysis of the flow distribution in the cell type-I suggested the modification of the inlet and outlet geometry, see Figure 54, in order to guarantee a better distribution of flow rate along the different channels.

The following results obtained for the selected micro-cells: parallel channels type-II cell, standard serpentine, wavy-sinusoidal serpentine and the standard serpentine tested with glycerin solutions, are related to well-defined acquisition areas delimited in blue in Figure 55 for a set flow rate of 30 ml/min and Figure 56 for a set flow rate of 90 ml/min. At 90 ml/min the acquisition areas for the serpentine configurations are greater than those at 30 ml/min allowing to capture the rapid displacement of tracer particles, especially close to the curvilinear sections. For all configurations, images were acquired far from the inlet channel in order to have a completely developed flow field. In Figure 55 B/C and Figure 56 B/C areas delimited in red are the channel parts whose technical details are shown in the lower left panel.

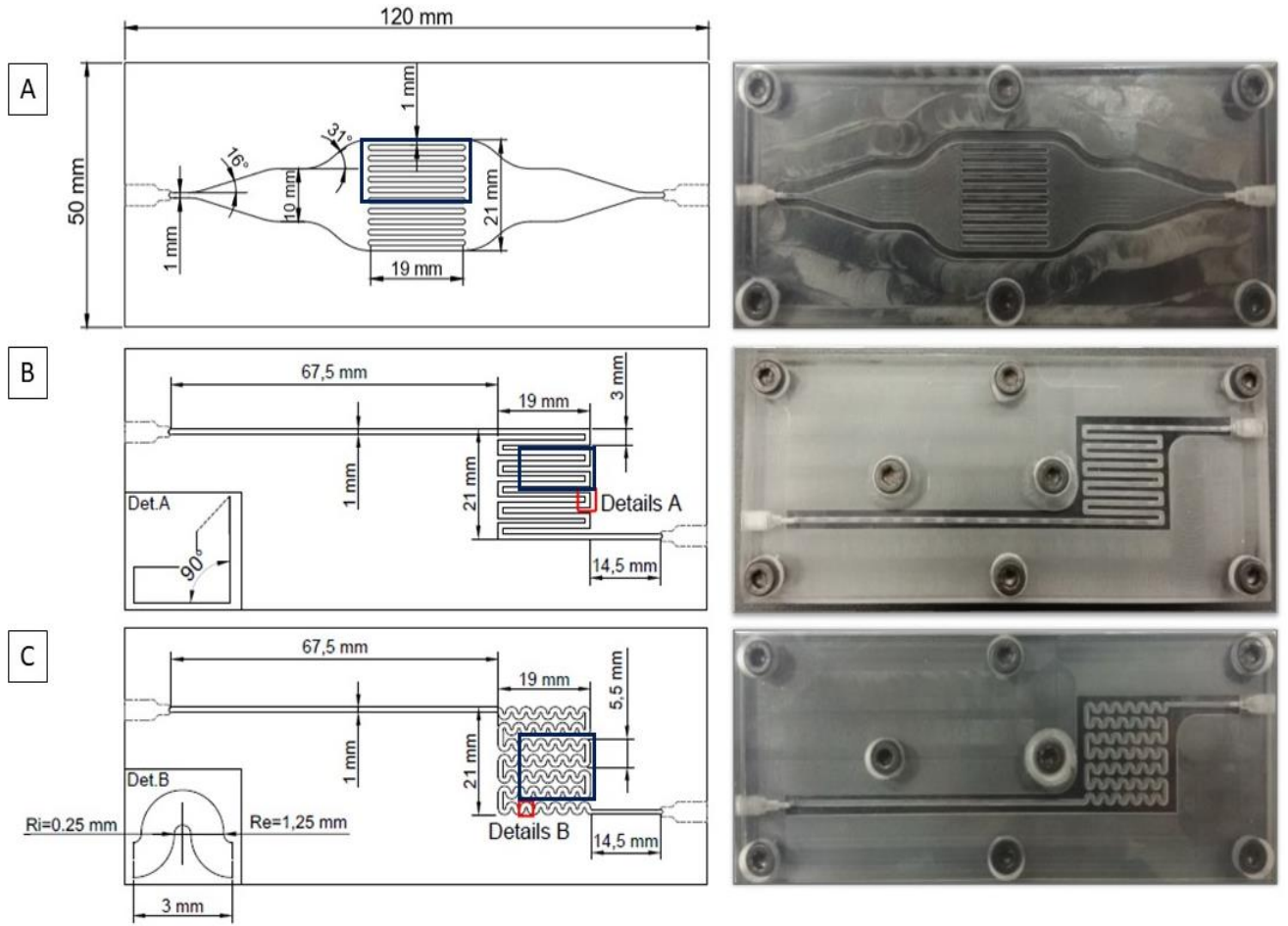


Figure 56: Flow rate of 90 ml/min. Acquisition areas delimited in blue with main technical features (left column) and picture (right column) of the top view of the micro-cells. A) straight parallel channels type-II, B) standard serpentine, C) wavy-sinusoidal serpentine. In red the area whose technical details are shown in the lower left panel.

6.2 Mean velocity vectors and magnitude fields

In Figure 57, the velocity vectors map of the micro cells are compared at a flow rate of 30 ml/min. The results reported for the parallel channel configuration, Figure 57a, show a very uniform inlet and outlet flow, with only a few relevant modifications, in accordance with the work of Jiao et al. (2005), on liquid water transport in straight micro-parallel-channels [50]. These are located at the inlet of each channel, giving rise to local accelerations, without any

relevant separation, and in the form of separated recirculating regions at the outlet crossings of different channels. On the other hand, for the standard serpentine cell, Figure 57b, at each 90° bend, a strong separation is observed, with both local acceleration and possible three-dimensional motion (as shown also in M. Hirota *et al.* (2000) [51] and Liou *et al.* (2018) [28]). This could highly increase the local heat transfer, especially as a consequence of the local accelerations and of the relatively large residual channel size. A similar condition is observed in the serpentine tested with solutions of water and glycerin, Figure 57d and Figure 57e. However, in these conditions the flow separation phenomenon in the curvilinear sections is gradually attenuated by the higher fluid viscosity, especially in the case of solution with 30 % water and 70 % glycerin. Also the wavy serpentine cell, Figure 57c, shows periodic large flow recirculation and reduced channel size, even if with large local accelerations (in accordance with work of W.M. Abed (2015) [20], Z. Dai *et al.* (2015) [24] and K. Tsatsumi *et al.* (2011) [52]). Again, this contributes to a local increase of heat transfer due to local accelerations, but also to a simultaneous decrease due to the reduced available channel cross-section. These results are in agreement with thermal measurement findings (Figure 43, Figure 44, Figure 45 and Figure 46), thus showing that the main reason for the increasing *Nusselt number* for serpentine cells in comparison to the parallel cell, at similar flow rates, is dependent on local high intensity accelerations. On the other hand, the reduced size of the channel in serpentine configurations is also the motivation for an increase in pressure drops. A slightly different discussion must be made in case of solution with 30 % water and 70 % glycerin characterized by high *Nusselt numbers* (Figure 45 and Figure 46) and local acceleration phenomena attenuated due to high fluid viscosity. In this case, indeed, the high thermal performance are due to mainly by thermal properties of solution, *e.g.* higher specific heat, rather than to specific fluid motion. The effect of viscosity on local accelerations will be investigated in section 6.5 with the analysis of velocity profiles.

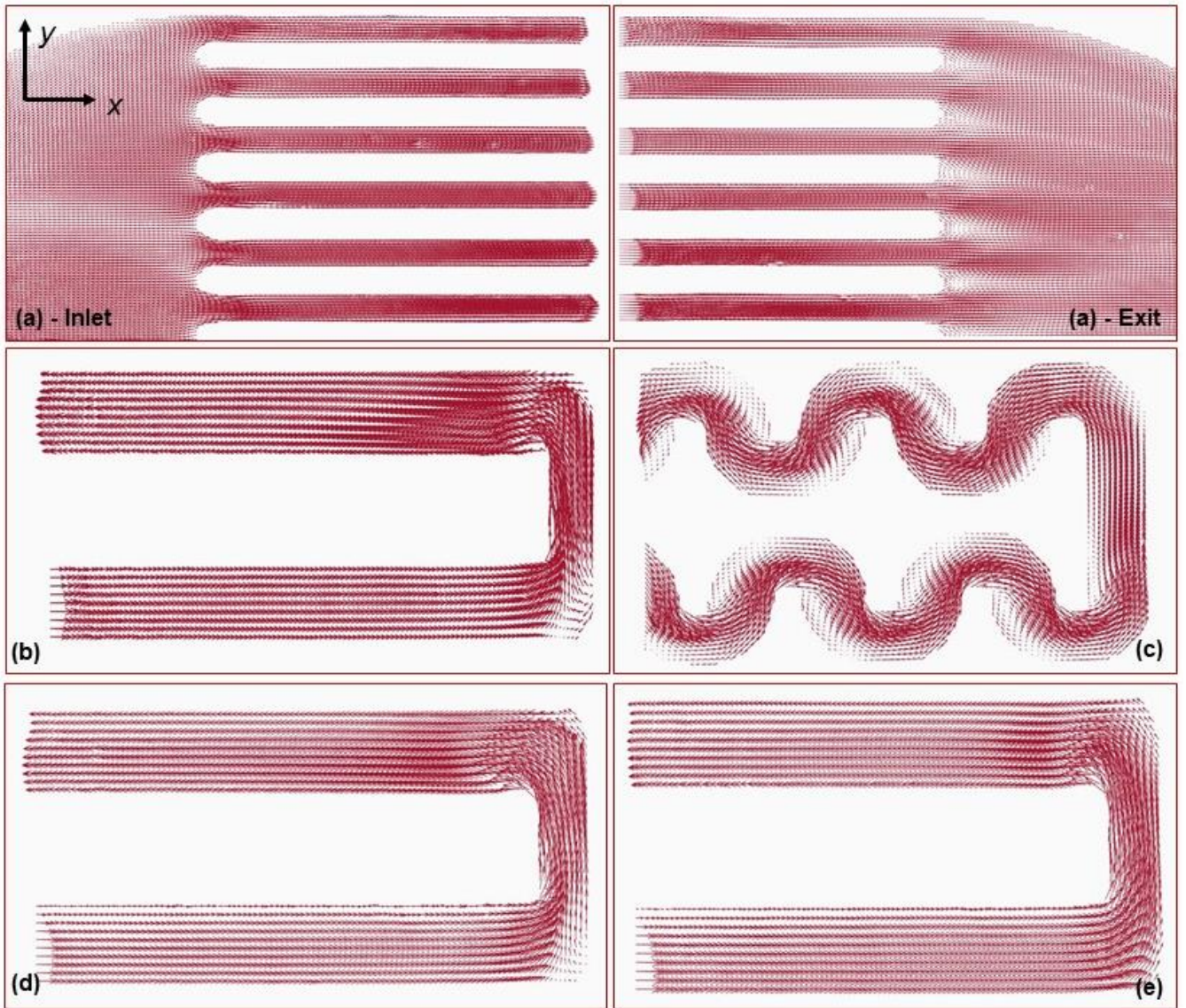


Figure 57: Mean velocity vectors fields at 30 ml/min. (a) straight parallel channels, (b) standard serpentine, (c) wavy serpentine, d) std. serpentine with 70 % water & 30 % glycerin, e) std. serpentine with 30 % water & 70 % glycerin.

In order to better appreciate the differences in the fluid flows of the cells, color maps of the average normalized velocity magnitude and vorticity fields, for a flow rate of 30 ml/min are reported in Figure 58 and Figure 63, respectively. The analysis of Figure 58 and Figure 63 confirms the concerns already emerged.

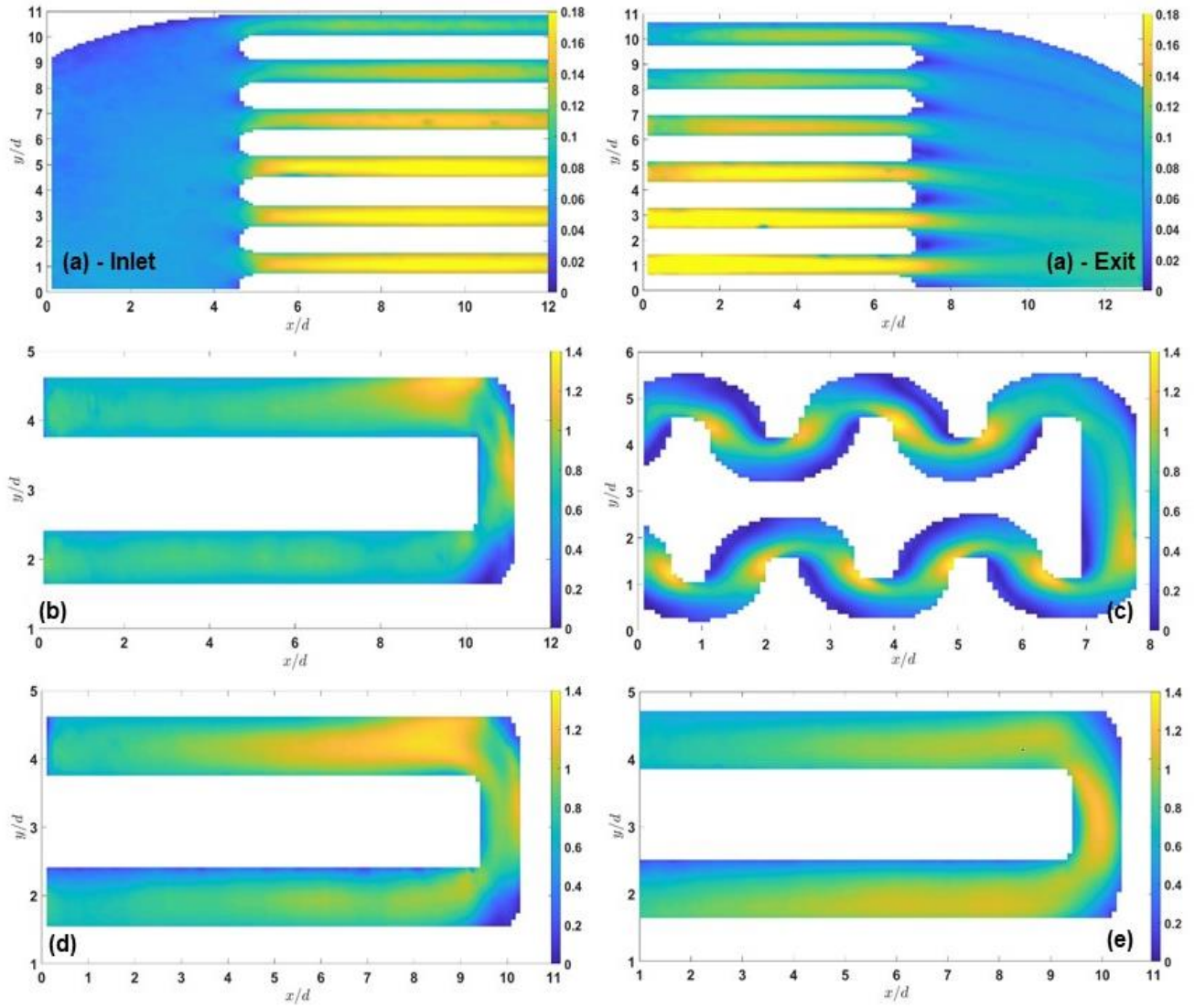


Figure 58: Mean velocity magnitude color maps at 30 ml/min. (a) straight parallel channels, (b) standard serpentine, (c) wavy serpentine, (d) std. serpentine with 70 % water & 30 % glycerin, (e) std. serpentine with 30 % water & 70 % glycerin.

Indeed, the yellow regions in Figure 58 represent quite high local velocities attained in the serpentine geometries (note the change in scale range), with related low velocity regions (accordingly to Abed *et al.* (2015) [20] and Liou *et al.* (2018) [28]). Indeed, in these high velocity sections, where the magnitude of the normalized velocity is larger than one, the average velocity is highly exceeded. Figure 58d and Figure 58e show the effect of the increase in fluid viscosity, due to different amounts of glycerin, on the velocity magnitude, which leads to a more

homogeneous velocity field with lower velocities. In Figure 58a, for the parallel channel geometry, it is also shown how the total flow rate is subdivided non-uniformly into the single channels. Actually, the large part of the flow, *i.e.* more than 60 % of the total flow rate, crosses the central five channels, making these central channels the main ones for the heat exchange process.

6.3 Mean Standard deviation and vorticity fields

The color maps of standard deviation of velocity components, u and v , are reported in Figure 59, Figure 60, Figure 61 and Figure 62, determined for all configurations at the two flow rates analyzed. The analysis of standard deviations allows to evaluate how much the instantaneous fields of velocity components u and v deviate from their mean values and therefore to evaluate the amount of mechanical energy transferred to vortical and turbulence motions. This, in some sense, is affecting the efficiency of heat transfer.

The values and axes shown in Figure 59, Figure 60, Figure 61 and Figure 62 are made non-dimensional by dividing it by bulk velocity and channel diameter, respectively. For both flow rates, similar discussions can be made. Starting by the parallel channels cell, it shows very low values of standard deviation for both components, suggesting an almost total absence of important alterations of fluid motion in instantaneous fields with reference to prevailing direction (right to left) and a very good compliance of those with their average values. A different condition is for serpentine configurations that have higher values of Std , but still contained in a range of 0-0.1, especially for the u component. For these micro-cells the highest standard deviation values are obtained in correspondence of bend and curve sections, underlining the presence of vortical and turbulence motions due to inversion of flow direction. By Comparing Figure 59b, d and e, the effect of fluid viscosity on three-dimensional motions occurring inside

the channel is evident. In case of standard serpentine tested with a solution of 30 % water and 70 % glycerin the turbulence phenomena appear completely damped, confirming the results obtained from the velocity fields analysis.

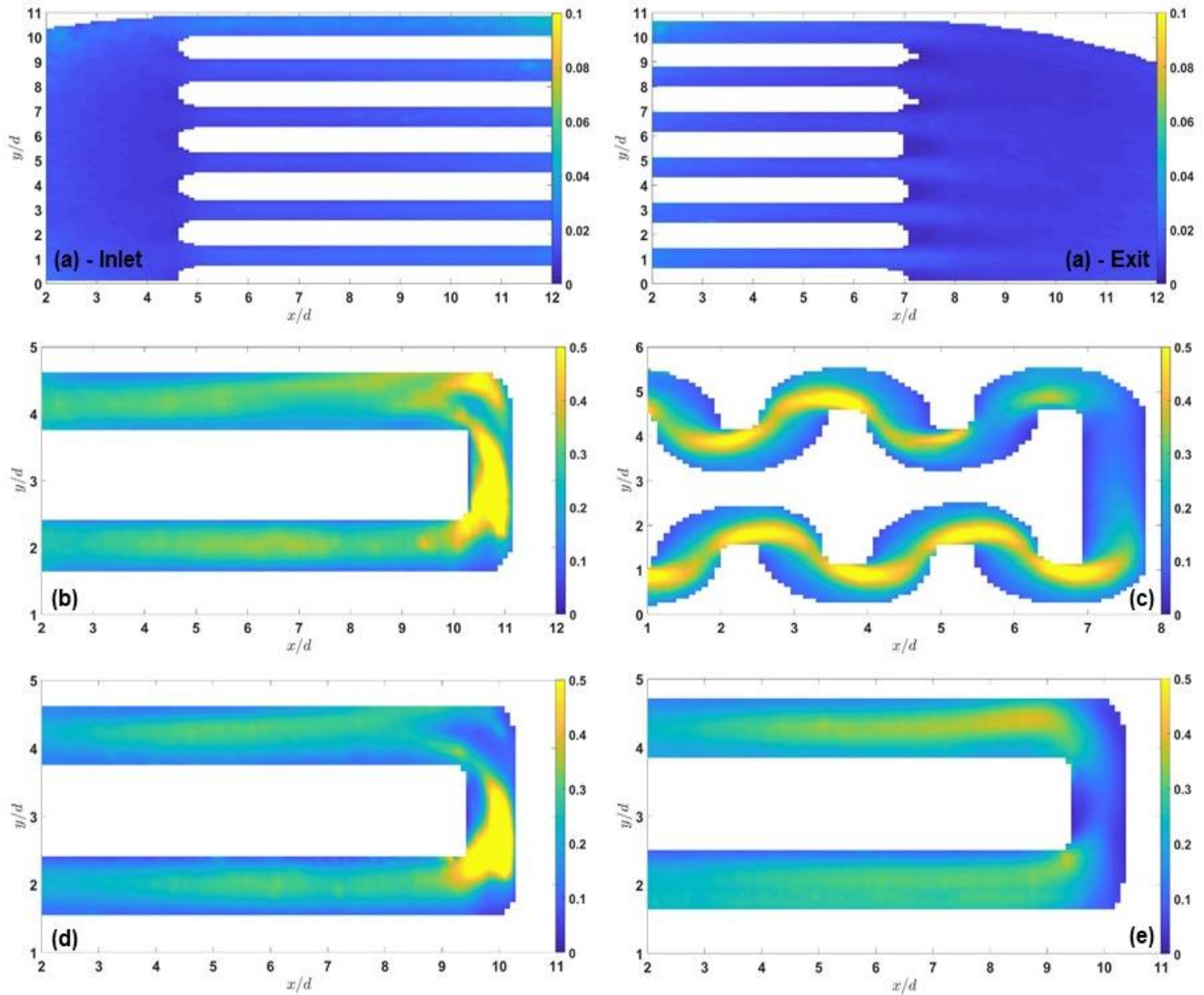


Figure 59: Standard Deviation of u component at 30 ml/min. a) straight parallel channels type-II, b) standard serpentine, c) wavy-sinusoidal serpentine, d) std. serpentine with 70 % water & 30 % glycerin, e) std. serpentine with 30 % water & 70 % glycerin .

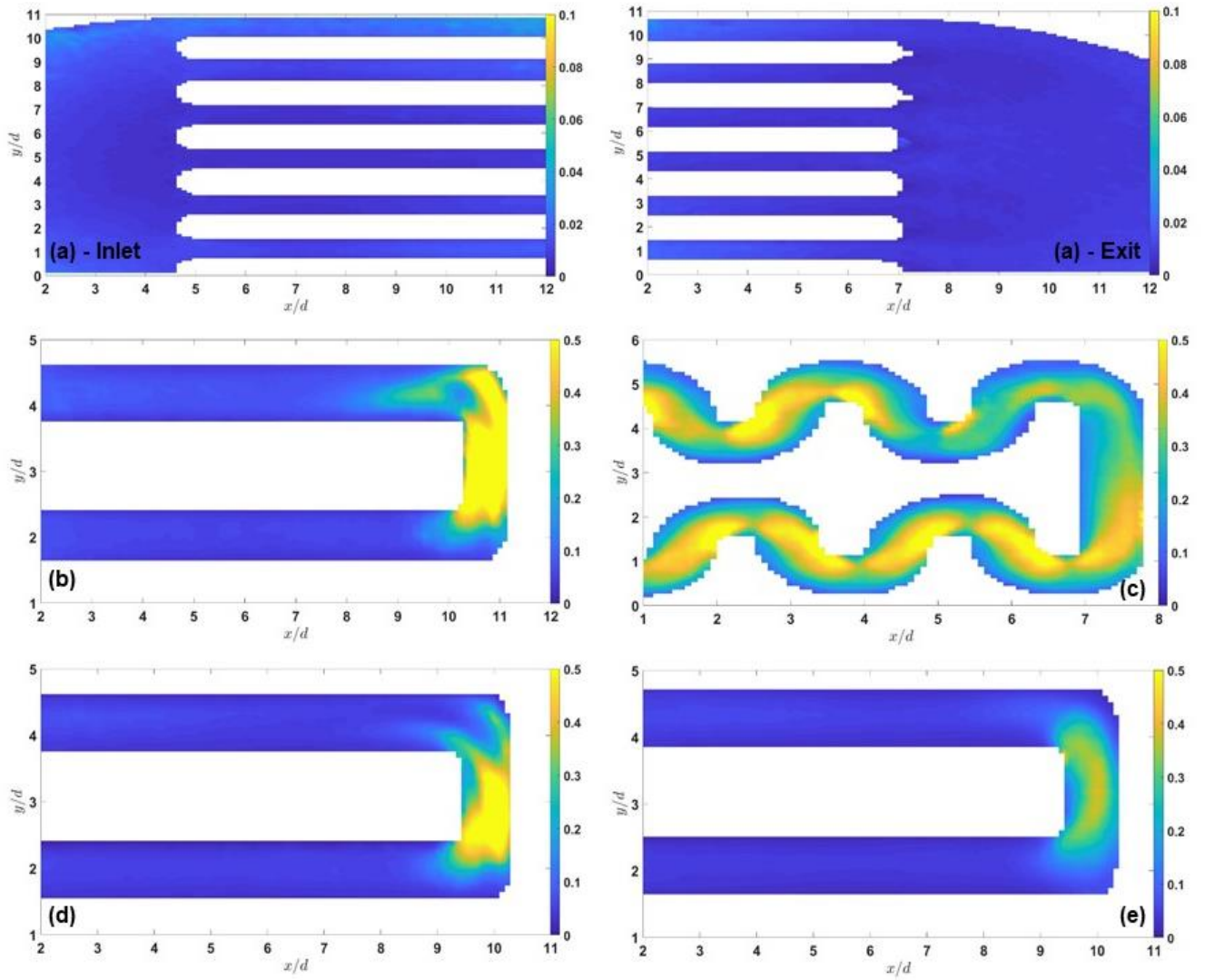


Figure 60: Standard Deviation of v component at 30 ml/min. a) straight parallel channels type-II, b) standard serpentine, c) wavy-synusoidal serpentine, d) std. serpentine with 70 % water & 30 % glycerin, e) std. serpentine with 30 % water & 70 % glycerin.

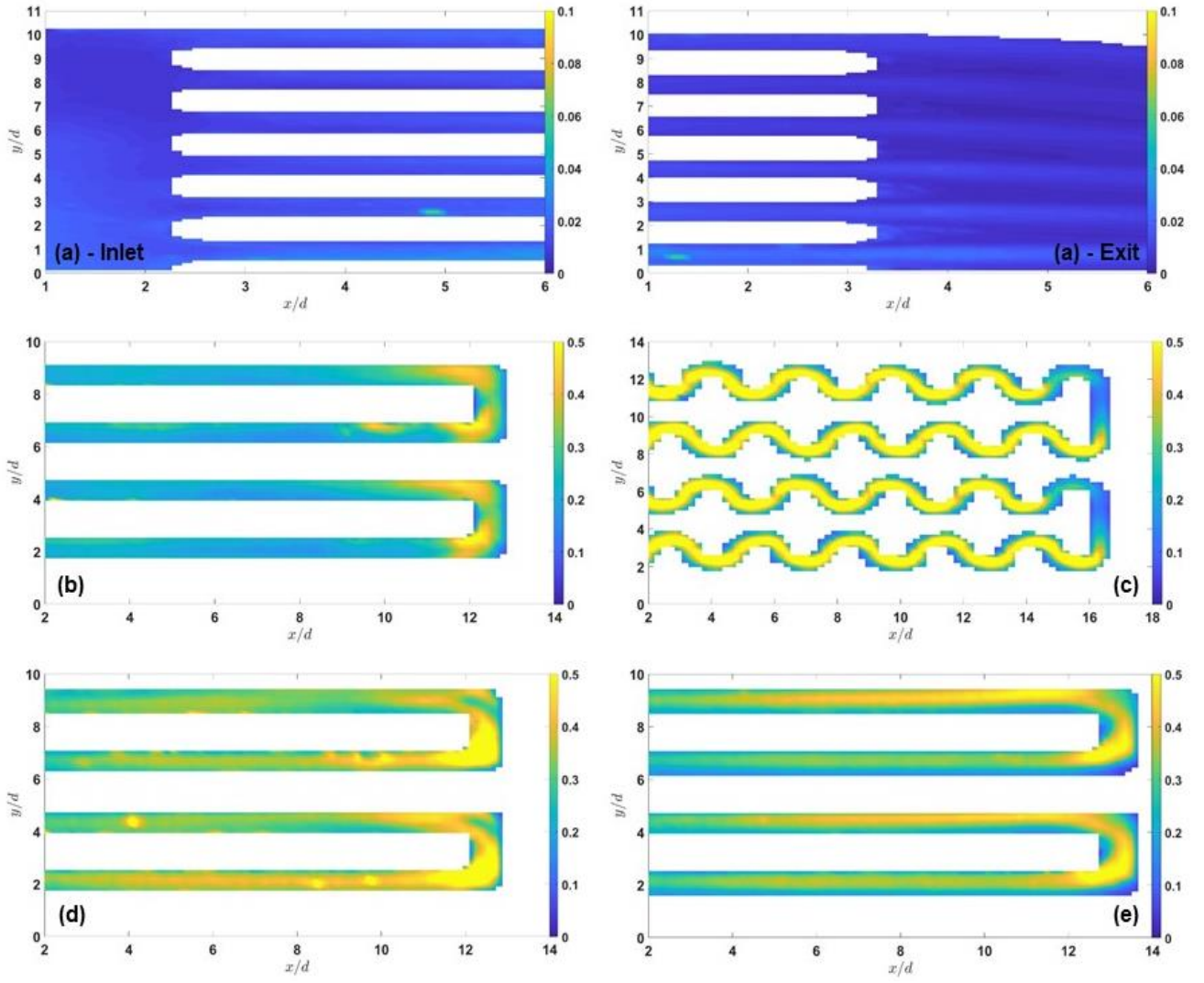


Figure 61: Standard Deviation of u component at 90 ml/min. a) straight parallel channels type-II, b) standard serpentine, c) wavy-sinusoidal serpentine, d) std. serpentine with 70 % water & 30 % glycerin, e) std. serpentine with 30 % water & 70 % glycerin.

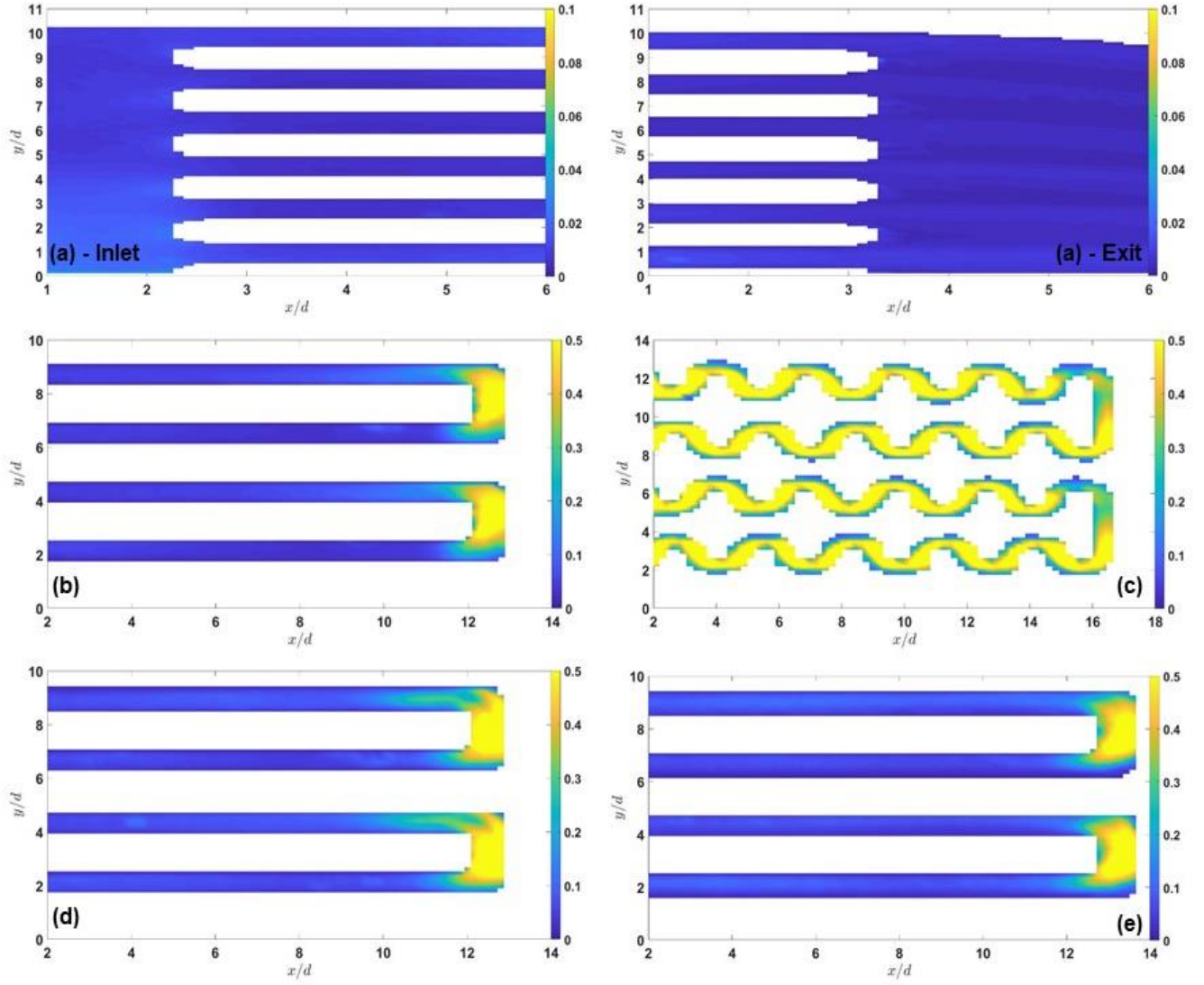


Figure 62: Standard Deviation of v component at 90 ml/min. a) straight parallel channels type-II, b) standard serpentine, c) wavy-synusoidal serpentine, d) std. serpentine with 70 % water & 30 % glycerin, e) std. serpentine with 30 % water & 70 % glycerin.

In order to better understand the influence of geometry on the vortical motions, color maps of the average normalized vorticity fields, for a flow rate of 30 ml/min are reported in Figure 63. Where it is possible to observe a growth in the level of vorticity from geometry (a), where it is limited to boundary layers, to geometry (b-d-e), where vorticity is high in boundary layers along straight sections and in recirculation regions at bending sections and to geometry (c), which shows vorticity of opposite sign in correspondence of each curvilinear section.

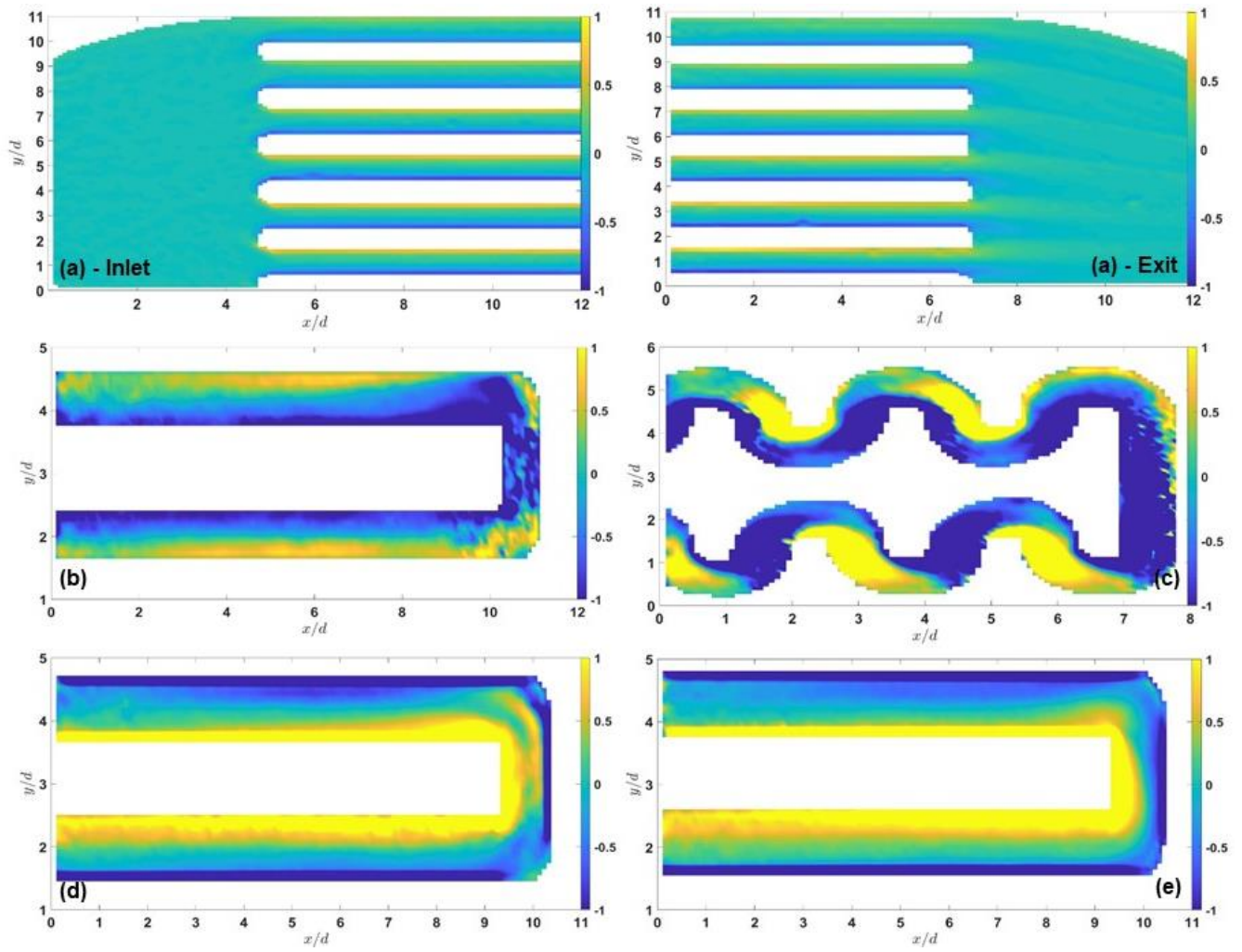


Figure 63: Mean vorticity color maps at 30 ml/min. (a) straight parallel channels, (b) standard serpentine, (c) wavy serpentine, (d) std. serpentine with 70 % water & 30 % glycerin, e) std. serpentine with 30 % water & 70 % glycerin.

Also in this case, it can easily be observed the influence of a higher fluid viscosity on the formation of recirculation zones, attenuated in both cases (d and e), in comparison to the standard serpentine filled with water. Therefore, results in Figure 58 and Figure 63 show that the local fluid mechanics motivation for improved global heat transfer performances in serpentine rather than in linear configurations derives from the simultaneous presence of recirculation and acceleration regions, except in cases where the thermal properties of cooling fluid are predominant over fluid-dynamic phenomena.

6.4 Mean velocity vectors, magnitude and vorticity fields at 90 ml/min

The situation is similar also moving towards the turbulent regime, as shown in Figure 64, Figure 65 and Figure 66, for a higher flow rate of 90 ml/min. The basic concerns are the same as before, of course with different values. The greater differences compared to results obtained at 30 ml/min emerged in serpentine configurations. Starting from standard serpentine configuration and by comparing the color-maps of magnitude at 30 ml/min, Figure 58b/d/e, and 90 ml/min, Figure 65b/d/e, it is immediately noticeable how at 90 ml/min the magnitude of the normalized velocity is larger than one also in the linear sections, suggesting a major effect of curvature on fluid motion, with the consequence of larger flow acceleration areas. On the other hands, the color maps of vorticity showed no substantial differences, confirming even at this flow rate the presence of turbulent motions in correspondence of bending zones. Instead, for the wavy configuration the comparison between Figure 58c, magnitude at 30 ml/min, and Figure 65c, magnitude at 90 ml/min, shows a loss of information on fluid motion. Presumably, at this flow rate the particles motion in correspondence of acceleration areas was too fast to allow the acquisition of reliable images. However, vorticity still confirms the results obtained at 30 ml/min.

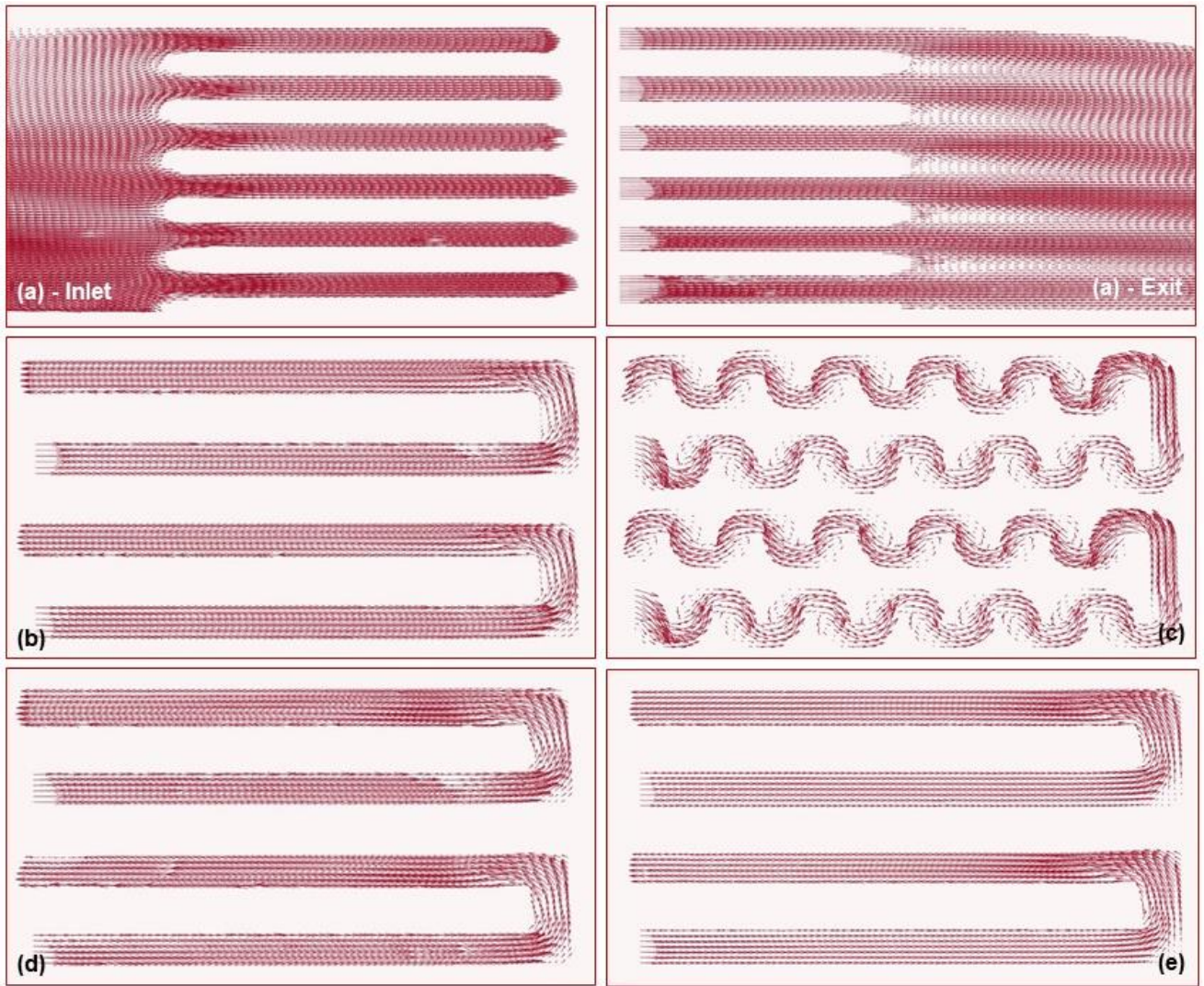


Figure 64: Mean velocity vectors fields at 90 ml/min. (a) straight parallel channels, (b) standard serpentine, (c) wavy serpentine, d) std. serpentine with 70 % water & 30 % glycerin, e) std. serpentine with 30 % water & 70 % glycerin.

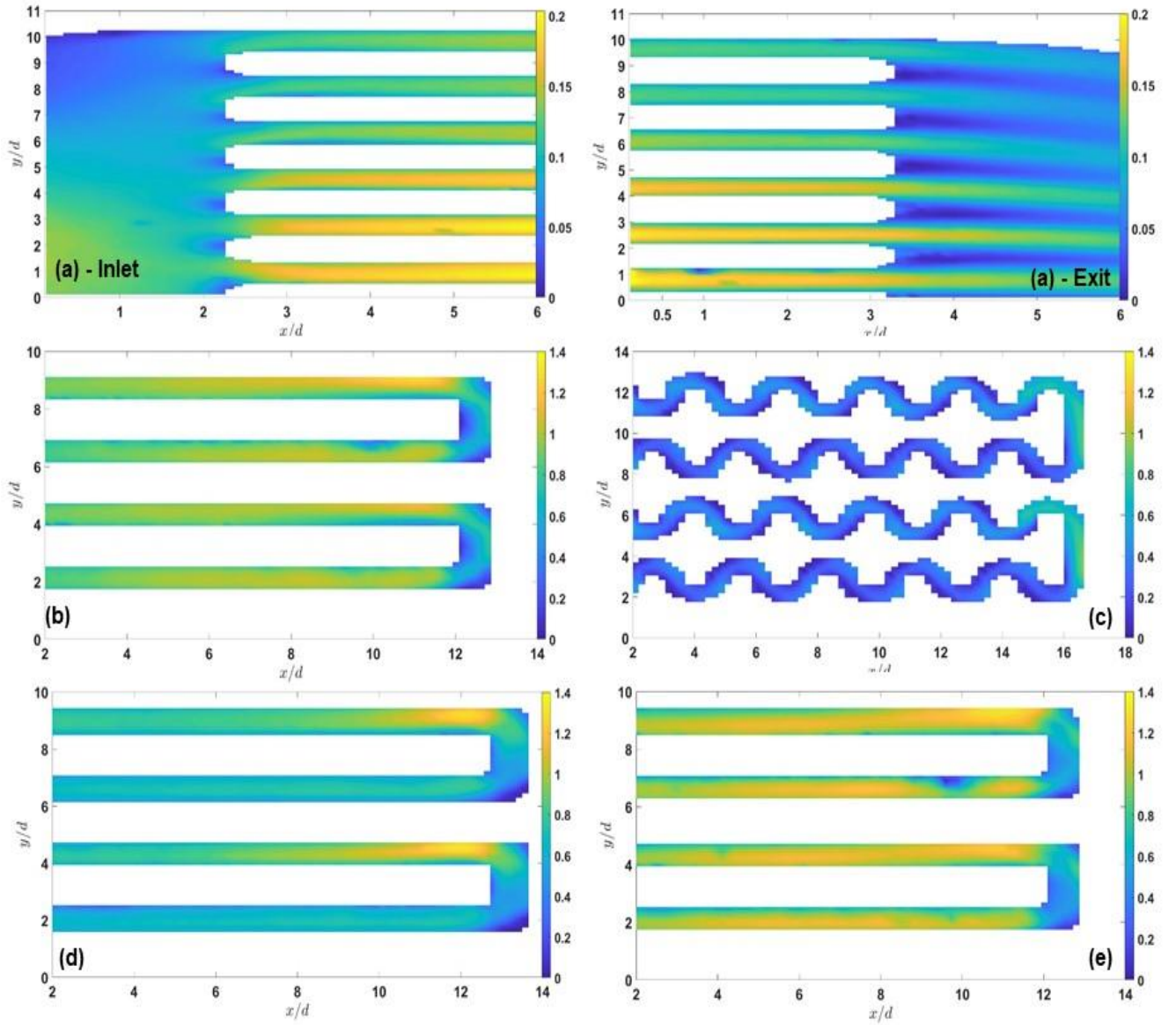


Figure 65: Mean velocity magnitude color maps at 90 ml/min. (a) straight parallel channels, (b) standard serpentine, (c) wavy serpentine, d) std. serpentine with 70 % water & 30 % glycerin, e) std. serpentine with 30 % water & 70 % glycerin.

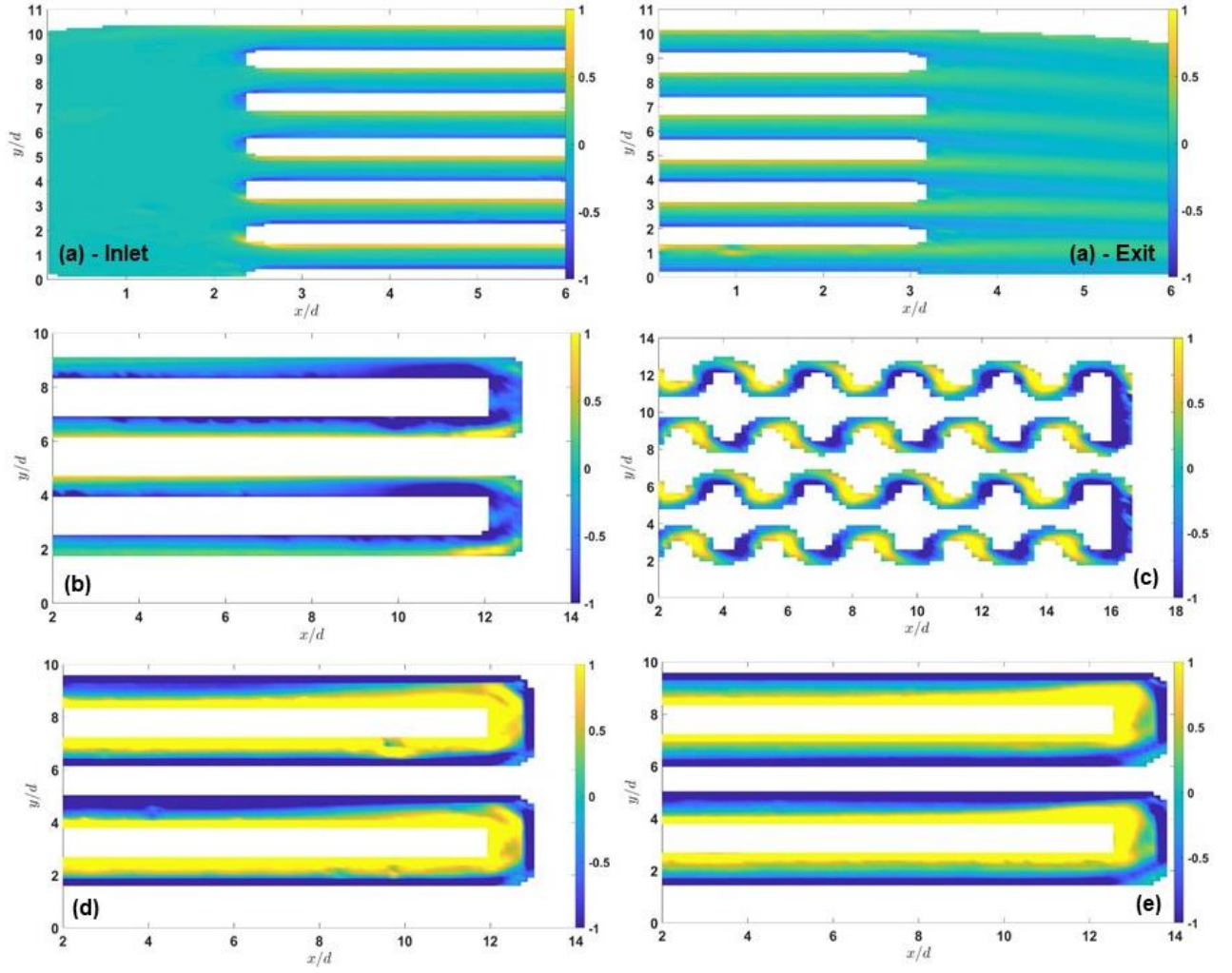


Figure 66: Mean vorticity color maps at 90 ml/min. (a) straight parallel channels, (b) standard serpentine, (c) wavy serpentine, d) std. serpentine with 70 % water & 30 % glycerin, e) std. serpentine with 30 % water & 70 % glycerin.

6.5 Vertical Profiles of standard serpentine cells

Looking at the mean fields of velocity magnitude, Figure 58 and vorticity, Figure 63, the effect of fluid viscosity on motion field has clearly emerged. To detail quantitatively this aspect a comparison is made between vertical profiles extracted at a flow rate of 30 ml/min in different sections of channel between the standard serpentine tested with water and those tested with two solutions of water and glycerin. The sections considered for the profile comparison are

shown in the following Figure 67. For each configuration section 1 is nine points away from the vertical element, section 2 is taken half a point away from the lower rectilinear side and section 3 is around one point away from the vertical element. The results obtained are shown in the Figure 68, Figure 69 and Figure 70, where u and v are the velocity components, U_{bulk} is the bulk velocity employed as a normalization factor and d is the channel diameter.

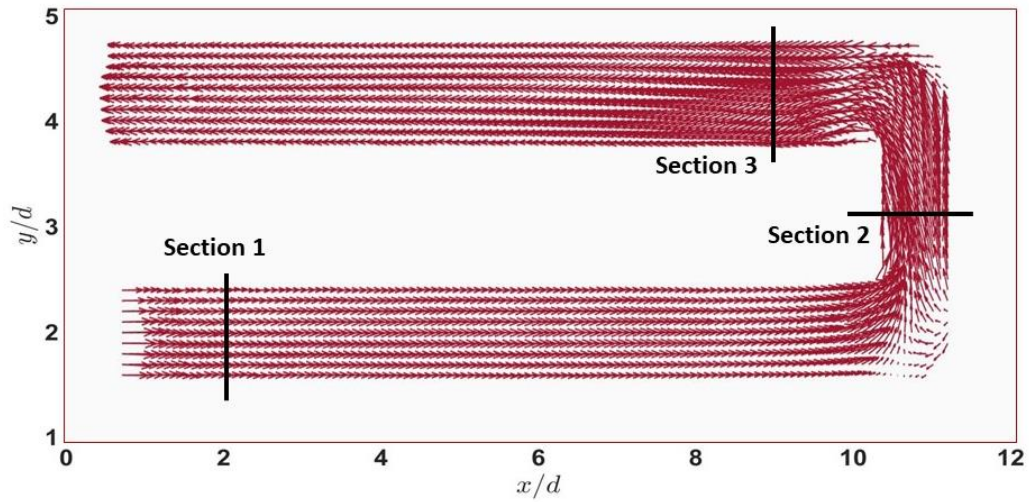


Figure 67: Standard serpentine geometry. Sections for the analysis of vertical profiles.

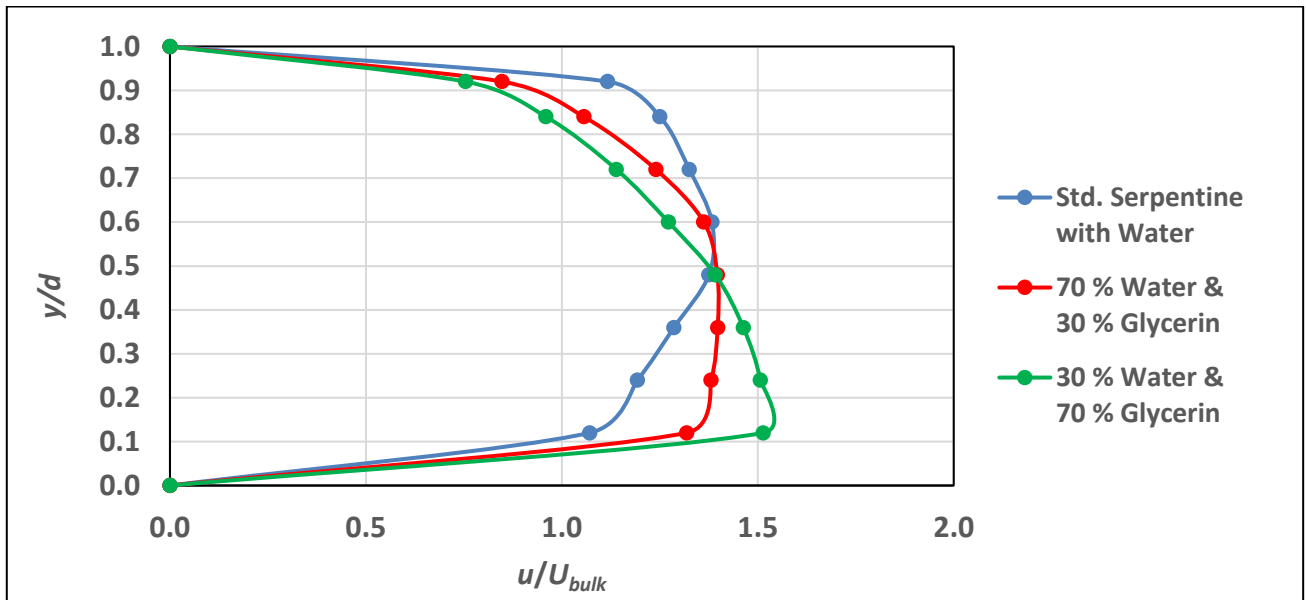


Figure 68: Comparison of vertical profiles extracted at position 1. Std. serpentine tested with water (red curve), std. serpentine tested with 70 % water and 30 % glycerin (blue curve) and std. serpentine tested with 30 % water and 70 % glycerin.

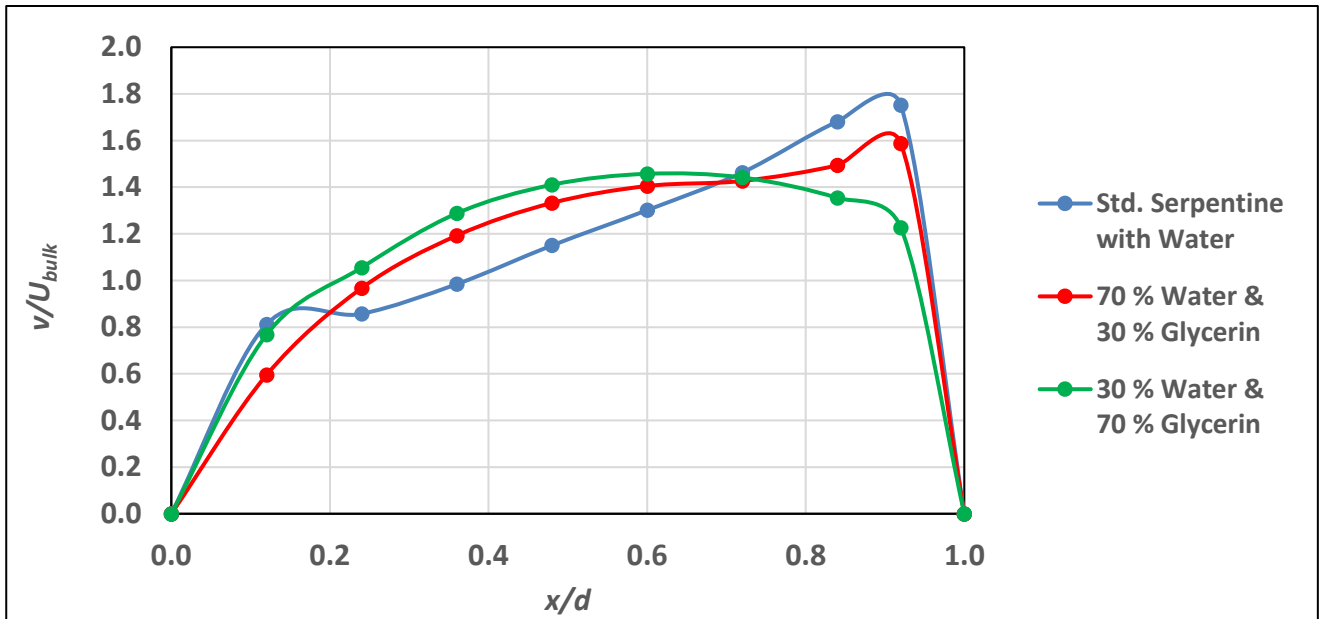


Figure 69: Comparison of vertical profiles extracted at position 2. Std. serpentine tested with water (red curve), std. serpentine tested with 70 % water and 30 % glycerin (blue curve) and std. serpentine tested with 30 % water and 70 % glycerin.

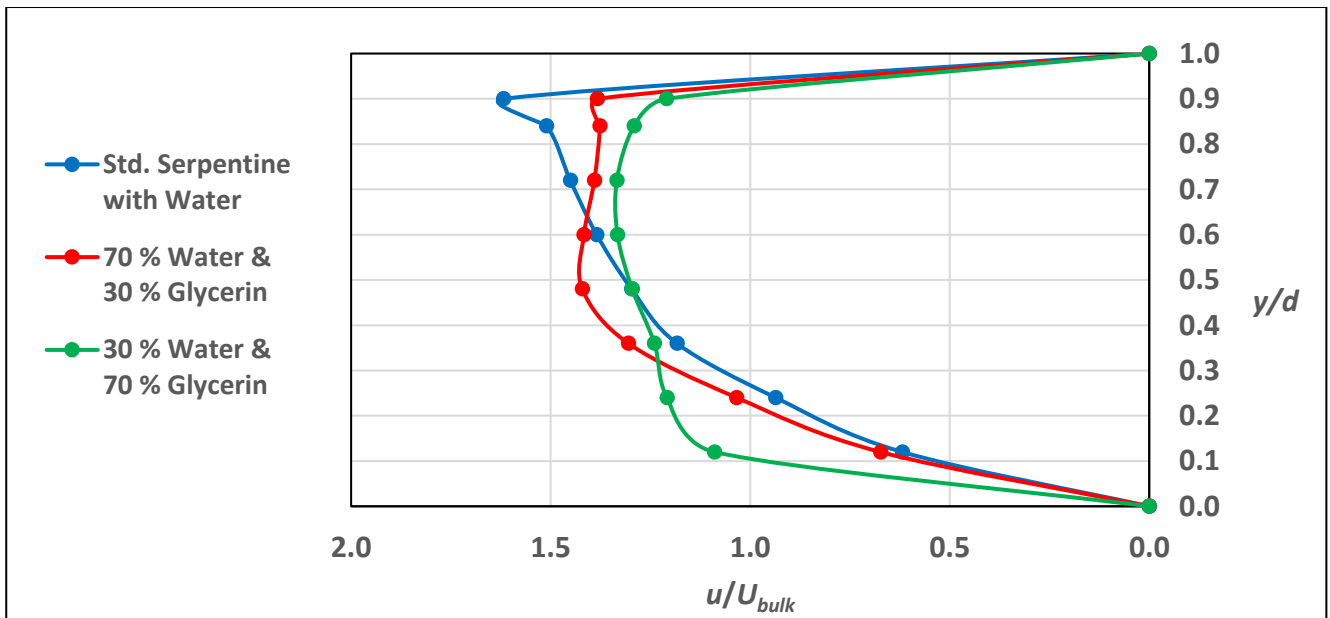


Figure 70: Comparison of vertical profiles extracted at position 3. Std. serpentine tested with water (red curve), std. serpentine tested with 70 % water and 30 % glycerin (blue curve) and std. serpentine tested with 30 % water and 70 % glycerin.

Figure 68 shows the profiles extracted at position 1 taken away from the bending zone in the middle of the horizontal section. From the overlap of curves it can be notice how the peak reached by curves extracted in cases with glycerin is shifted downwards compared to the parabolic trend of serpentine tested with water. This translation is presumably caused by greater inertia of fluid to reoccupy the entire cross-section downstream of curve and the attenuated recirculation areas in correspondence of curvilinear section as shown by vectors fields in the Figure 57d and Figure 57e. On the other hand, Figure 69 and Figure 70 show another aspect of increase in viscosity. First of all a gradual damping of the curvature effect on fluid motion as the percentage of glycerin in solution increases. It is possible to identify this damping effect by observing in Figure 69 a more symmetric and parabolic trend of curve, especially for the solution with 70 % glycerin, with a consequent attenuation of maximum value reached by local fluid accelerations at the exit of bending zone, Figure 70. All these trends are in agreement with the mean velocity vector fields and magnitude findings for these configurations, confirming that the main reason for the increasing *Nusselt number* for serpentine cell tested with solutions of water and glycerin, at similar flow rates, is not dependent only by local high intensity accelerations, but especially by greater thermal properties given by glycerin.

6.6 Mean Entropy fields

Following previous works on the argument ([25], [26], [53]), an indicator of the local contribution to mixing and heat exchange is given by the local rate of entropy production, assuming convective motions without internal heat generation. Since any non-equilibrium process is an irreversible process, due to the second law of thermodynamics, it is possible to define the entropy production as a function of velocity gradients, see Eq. 30, this makes entropy rate a measure of mixing and heat transfer capability, so far being here used to quantify the previous statements. Mean entropy production rates are shown in Figure 71 for all

configurations at 30 ml/min, made non-dimensional by using bulk velocity and channel diameter. At a first sight, it is clear that such a production basically vanishes all over the field for the parallel channel configuration, except for the boundary layers and the outlet crossing of the channels. On the other hand, the highest entropy is achieved in the standard serpentine cells, being related to the local flow acceleration and not to the recirculation, as confirmed by the comparison with Figure 58 and Figure 63.

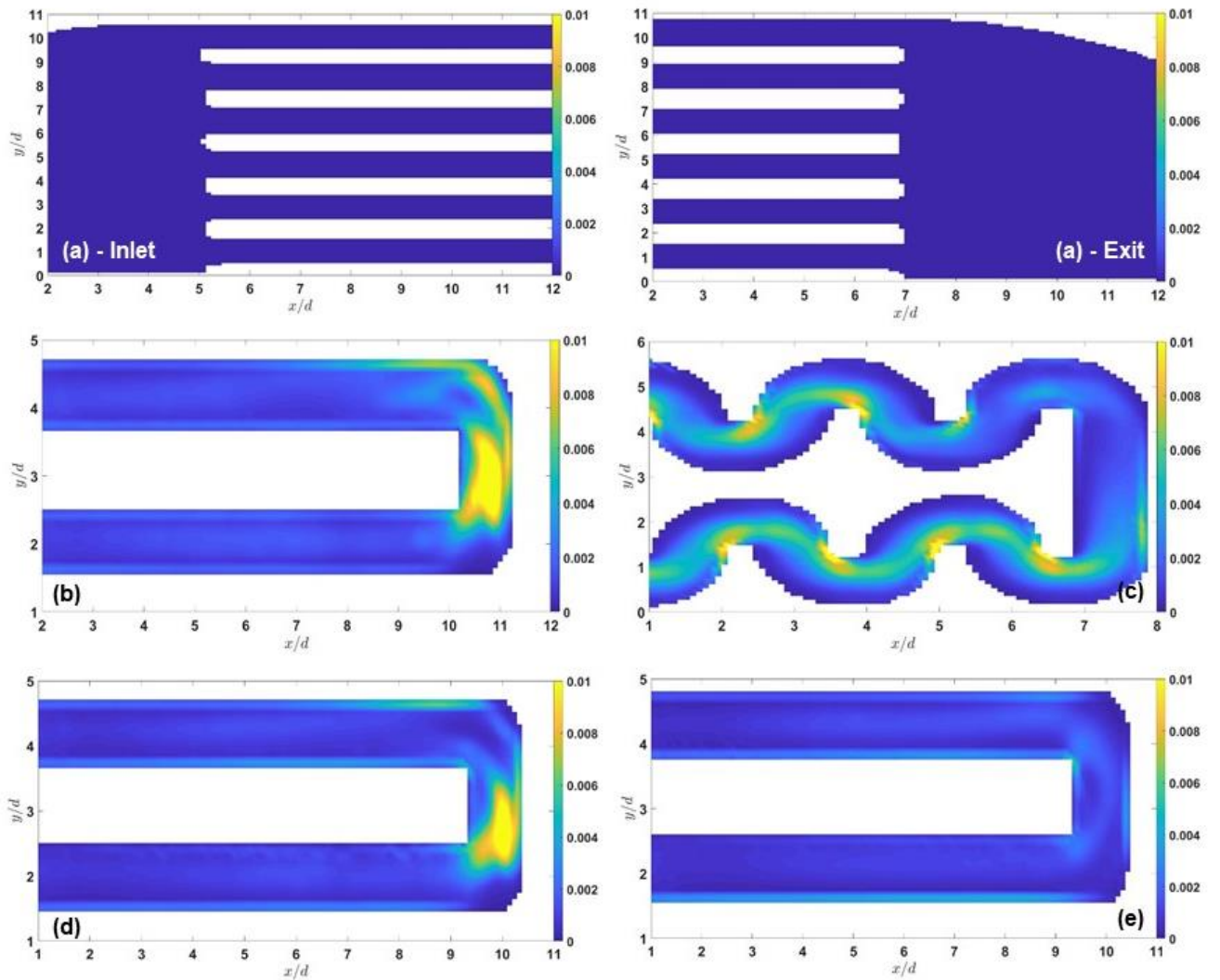


Figure 71: Mean entropy fields at 30 ml/min. (a) straight parallel channels, (b) standard serpentine, (c) wavy serpentine, d) std. serpentine with 70 % water & 30 % glycerin, e) std. serpentine with 30 % water & 70 % glycerin.

In Figure 71e, the production of entropy appears very low, almost zero, due to the absence of local high intensity accelerations along the path, as shown in Figure 58e, so far partially suppressed by the high viscosity of flow. The correspondence of local flow acceleration with highest entropy values is established also for the wavy serpentine configuration, where the highest entropy values, slightly lower than the previous case, are related to the local increment of velocity. The comparison of the mean entropy fields obtained at 30 ml/min and 90 ml/min, Figure 72, shows that these phenomena take place also moving towards higher flow rates.

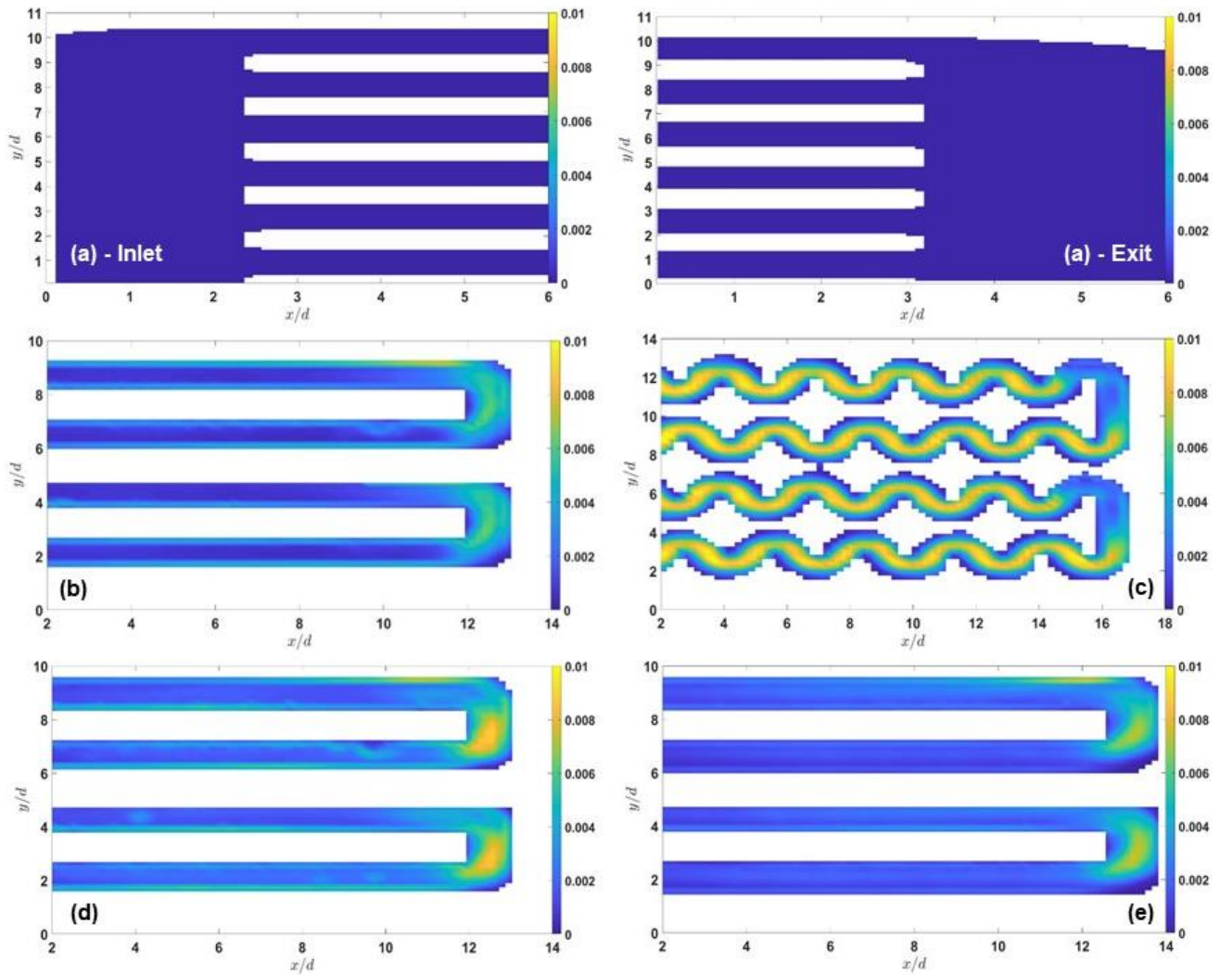


Figure 72: Mean entropy fields at 90 ml/min. (a) straight parallel channels, (b) standard serpentine, (c) wavy serpentine, d) std. serpentine with 70 % water & 30 % glycerin, e) std. serpentine with 30 % water & 70 % glycerin.

Therefore, by mean entropy field compared with magnitude and vorticity mean fields is possible to state that the recirculation regions do not contribute to mixing and heat transfer increment, rather only to pressure loss increments. So, on the base of the thermal analysis, the μ PIV results showed that the main reason for the increasing *Nusselt number* for the serpentine cells in comparison to the parallel cell, at similar flow rates, is only dependent on local high intensity accelerations and not on recirculation regions, as confirmed by mean entropy fields. Recirculations do not contribute to mixing and heat transfer increment, rather only to pressure loss increments, as the reduced size of the channel characteristic of the serpentine configurations, especially for the wavy micro-cell. Different conditions, instead take place, for solutions with high glycerin contents, *e.g.* 30 % water and 70 % glycerin, for which the high thermal exchange properties are mainly related to different properties of working fluid and not only to local high intensity fluid accelerations.

Chapter 7 – Conclusions

In the present work, the thermo-hydrodynamic behaviour of different micro-channels is investigated: a straight parallel channels configuration with two novel proposals of the inlet and outlet geometry, a conventional serpentine path, a new wavy-sinusoidal serpentine path and a U-shaped channel with aluminium horizontal ribs. Also the classical straight channel configuration is investigated to validate the measurement system. All configurations are tested with distilled water except for the conventional serpentine in which a solution with two different percentages of glycerin and water, *i.e.* 70 % glycerin and 30 % water; 30 % glycerin and 70 % water is also implemented. To test the heat transfer properties and the detailed fluid flow behaviour, this research was extended from typical range of *Reynolds number* in the laminar regime, from 50 to 1500, up to reach the turbulent regime with *Reynolds number* of 4000. Results are evaluated first in term of *Nusselt-Reynolds* diagram and then through the efficiency of the cells. Looking at *Nusselt-Reynolds* curves, serpentine configurations tested with water show larger *Nusselt numbers* than those of the parallel channel configuration, especially the wavy channel and serpentine cell with ribs attain the highest values of *Nusselt number*. Being *Nusselt number* a measure of heat flux due to convection this suggests a most efficient heat transfer given by the serpentine configurations. However, despite the potential of such cells, the serpentine channel tested with a solution of 30 % water and 70 % glycerin seems to attain the highest values of *Nusselt number*. Even if it is not possible to make a direct match for a given *Reynolds number* due to different viscosity, the trend of available values suggests the capability of this different cooling fluid to allow the most efficient heat transfer. In this plot also the impact of flow regime on convective motions emerged clearly showing the largest differences among the tested geometries in laminar conditions, whereas they are less pronounced in the turbulent regime. This is due to the fact that the serpentine configurations in comparison to parallel channels promote flow accelerations and recirculation already in laminar conditions, as emerged by μ PIV

analysis, and that these differences are attenuated in fully established turbulence. These previous results were partially confirmed by the efficiency performed by relating the average *Nusselt number* to the *Fanning factor*, that showed how the standard serpentine micro cell tested with water attains the highest heat exchange efficiency regardless of flow regime, getting high *Nusselt numbers* combined with low pressure losses. Thanks to a geometry assembled with a few right angles separated by long linear sections, this configuration allows a net improvement in comparison to the parallel channel configuration, with a relative geometrical complexity, and lower pressure losses in comparison to the wavy channel and serpentine with ribs cell with a very complex geometry. Also in this case the trend of the standard serpentine tested with a solution of 30 % water and 70 % glycerin suggests the capability of this configuration to allow very good performances. On the base of the thermal analysis the μ PIV measurements were employed to detail the observed global heat exchange performances of parallel channels type-II cell, standard serpentine and wavy-sinusoidal serpentine configuration, in order to make a link with results highlighted by the thermal measurements. Specifically, the attention was focused on local fluid recirculation and acceleration as related to the specific geometry and to the different flow rates. In particular the PIV results showed that the main reason for the increasing *Nusselt number* for the serpentine cells in comparison to the parallel cell, at similar flow rates, is only dependent on local high intensity accelerations and not on recirculation regions, as confirmed by mean entropy fields, that appear not contribute to mixing and heat transfer increment, rather only to pressure loss increments, as the reduced size of the channel characteristic of these configurations, especially for the wavy micro-cell. Different conditions, instead take place, for solutions with high glycerin contents, *e.g.* 30 % water and 70 % glycerin, for which the high thermal exchange properties are mainly related to different properties of working fluid and not only to local high intensity fluid accelerations. Lastly, the comparison of the mean fields (vectors,

magnitude, vorticity and entropy) obtained at 30 ml/min and 90 ml/min showed how the basic phenomena are similar also moving towards higher flow rate.

Appendix

A.1 Interpolation and extrapolation method

To calculate the *Nusselt number*, in each condition the equilibrium temperature reached by the outlet water ($T_{b,out}$) and the surface (T_w) after the thermal transient have to be considered. Due to the dependence of the syringe time on the flow rate, not for all conditions the available measurement time is long enough to reach thermal equilibrium. For this reason, the water and surface equilibrium temperatures are analytically determined on the base of a physical thermal model ([22]), applied to experimental data via an interpolation and extrapolation method:

$$T_{eq} = a \cdot e^{-b \cdot t} + c \quad (45)$$

where T_{eq} [°C] is the final equilibrium temperature reached by fluid, or wall, after the thermal transient; a, b, c are coefficients analytically determined and t [s] is the time ranging from 0 sec., start of measurement, to a maximum of 1400 sec., maximum extrapolation time.

The interpolation and extrapolation method is applied to all flow rates, even at lower ones, so as to homogenize the database having for all rates the water and surface temperature reached after 1400 seconds. The maximum extrapolation time of 1400 sec. is assessed on the base of the lowest flow rate equal to 6 ml/min, reaching the final equilibrium temperature in such a time interval.

Flow Rate [ml/min]	Measurement Time [seconds]	Extrapolation Time [seconds]
6	1400	1400
12	700	1400
18	467	1400
24	350	1400

30	280	1400
48	175	1400
60	140	1400
90	93	1400
102	82	1400
120	70	1400
138	61	1400
144	58	1400
150	56	1400
156	54	1400
168	50	1400
180	47	1400
210	40	1400
216	39	1400
240	35	1400

Table 22: Measurement time vs extrapolation time.

The analytical data analysis model is developed on Excel calculation program provided by *Microsoft Corporation* © and involves the use of a non-linear solver tool. The solver tool is based on the Generalized Reduced Gradient (GRG2) analysis code, developed by Leon Lasdon, Texas University, and Alan Waren, Cleveland University, in collaboration with the society leader in analytics for spreadsheets *Frontline Systems Inc.* [54].

Regardless of geometry and set hot plate temperature, for all flow rates, the initial database consists the temperature measurements of outlet fluid and surface. In particular, for the wall temperature (T_w) the analytical model is applied at the average values of the temperatures measured by the three thermocouples placed in the micro-cells bottom side (T_1, T_2, T_3):

$$T_w = \frac{T_1 + T_2 + T_3}{3} \quad (46)$$

The procedure is divided into two successive phases. In the first phase the coefficients a , b , c are obtained by applying a least square interpolation to experimental data, in an iterative way, by minimizing the sum of square residuals, given by the difference between measured data and those calculated with the physical model. To correctly execute the non-linear interpolation algorithm, it is necessary to provide initial non-zero values of the coefficients a , b and c , *i.e.* $a=10$, $b=0.001$ and $c=40$. The initial values are determined from the exponential function that approximates the experimental data, subsequently corrected with the values obtained from the least squares interpolation. In the second phase, after identifying the optimal coefficients, the equilibrium temperature is determined at a time of 1400 sec. through an extrapolation process.

A.2 Error analysis: Reynolds and Nusselt numbers

In the Re and Nu equations some terms, such as $U, \dot{m}, T_{b,in}, T_{b,out}, T_w$, are calculated starting from experimental data by means of physical relations or mathematical models. The error on the experimental data due to instrumentations and the error associated with the analytical model, propagate within the calculation process, leading to a degree of uncertainty on the values obtained for the dimensionless numbers. The estimation of error is evaluated through an accurate error analysis performed on the following points:

- Flow rate set on the syringe pump, \dot{Q}
- Measured temperature, $T_{in/out/w}$
- Residuals of the interpolation and extrapolation analytical model.

The temperature set on the hot plate is error-free because the plate reaches precisely the set value. To determine the error propagated on the *Reynolds number*, the quantity to be considered is the volumetric flow rate \dot{Q} , set on the syringe pump and used to calculate the bulk velocity. All the other quantities are physical and geometrical terms assumed without error. The flow rate error, $\Delta\dot{Q}$, is given by the uncertainty relating to the setting of flow rate value on syringe pump equal to ± 0.05 ml/min, as explained in chapter 3.

$$\Delta Q = 0.05 \frac{\text{ml}}{\text{min}} = 8.3 \cdot 10^{-10} \frac{\text{m}^3}{\text{s}} \quad (47)$$

on the basis of the flow rate error, the error propagated on Re is given by:

$$\Delta Re = \left| \frac{\delta Re}{\delta \dot{Q}} \right| \Delta \dot{Q} = \left| \frac{\rho l}{S \mu} \right| \Delta \dot{Q} = \left| \frac{Re}{\dot{Q}} \right| \Delta \dot{Q} \quad (48)$$

with a percentage error of:

$$\Delta Re_{\%} = \frac{\Delta Re}{Re} \cdot 100 \quad (49)$$

Unlike Re , the uncertainty on *Nusselt number* is function of the micro-cell type considered. In fact, being Nu a function of the fluid temperature at the outlet of the channel and the wall temperature, it is affected by different errors depending on geometry and set flow condition. The error in the outlet temperature and wall is given by two factors. The first is the uncertainty related to the mathematical model applied for the interpolation of the experimental data and the extrapolation of the equilibrium temperature. The second is the error of the measuring instrument.

The uncertainty in the model is calculated as the ratio between the sum of square residuals and the amount of the input experimental data. The residual of the least squares interpolation is given by the difference between the measured temperature datum and the temperature calculated with the physical model.

$$\Delta T_{b,out/w} = \frac{\sum residuals^2}{n^{\circ} data} = \frac{\sum (T_{measure} - T_{model})^2}{n^{\circ} data} \quad (50)$$

The error related to the thermocouple reader of ± 0.05 °C, chapter 3, affects all measured temperatures: $T_{b,in}$, $T_{b,out}$ and T_w . For $T_{b,out}$ and T_w if the error value of the mathematical model is less or equal than the instrument error, only this latter is taken into account for the analysis. Otherwise, the highest value is considered.

$$\Delta T_{b,in} = \Delta T_{b,out} = \Delta T_w = 0.05 \text{ }^{\circ}\text{C} \quad (51)$$

In last, the flow rate error is the same considered for the *Reynolds number*:

$$\Delta Q = 0.05 \frac{\text{ml}}{\text{min}} = 8.3 \cdot 10^{-10} \frac{\text{m}^3}{\text{s}} \quad (52)$$

All other physical and geometrical parameters have been assumed to be error-free. At this point the error on Nu can be derived:

$$\begin{aligned} \Delta Nu &= \left| \frac{\delta Nu}{\delta Q} \right| \Delta Q + \left| \frac{\delta Nu}{\delta (T_{b,out} - T_{b,in})} \right| \Delta (T_{b,out} - T_{b,in}) + \left| \frac{\delta Nu}{\delta (T_w - T_b)} \right| \Delta (T_w - T_b) = \\ &= \left| \frac{Nu}{Q} \right| \Delta Q + \left| \frac{Nu}{T_{b,out} - T_{b,in}} \right| \Delta (T_{b,out} - T_{b,in}) + \left| \frac{Nu}{T_w - T_b} \right| \Delta (T_w - T_b) \end{aligned} \quad (53)$$

where the error in T_b is:

$$\Delta T_b = \left| \frac{T_b}{T_{b,in} + T_{b,out}} \right| \cdot (\Delta T_{b,in} + \Delta T_{b,out}) \quad (54)$$

also in this case the percentage error is determined as:

$$\Delta Nu_{\%} = \frac{\Delta Nu}{Nu} \cdot 100 \quad (55)$$

A.3 Particle Image Velocimetry analysis and post-processing

Detailed fluid dynamics measurements are required to detail the observed global heat exchange performances of micro-cells, in order to correlate the fluid dynamic and thermal fields and to explain the heat exchange properties of the micro-devices on the basis of the fluid dynamics phenomena occurring inside the channel. To characterize the velocity fields of micro-cells at 30 ml/min and 90 ml/min, the Micro Particle Image Velocimetry (μ PIV) technique is employed ([47],[55],[56]). It is important to underline that it was not considered necessary for purposes of the study to further investigate the vortical structures and three-dimensional motions that occur within the channels with a full 3D analysis, because for the aim of work the PIV measures have the main objective to support the thermal analysis results and to identify the causes of a higher heat exchange efficiency, together with the detection of those factors that instead hampered this process. The detailed fluid dynamics analysis, carried out to detect the main fluid characteristics for each geometry and cooling fluid studied, is performed on the basis of high resolution images acquired of the region of interest by an open source MATLAB-*MathWorks* © script: *PIVlab2017* developed by Dr. W. Thielicke and Prof. Dr. Eize J. Stamhuis [57]. In the images elaboration process two consecutive frames are analyzed in order to determine the flow tracer displacements using cross-correlation algorithms.

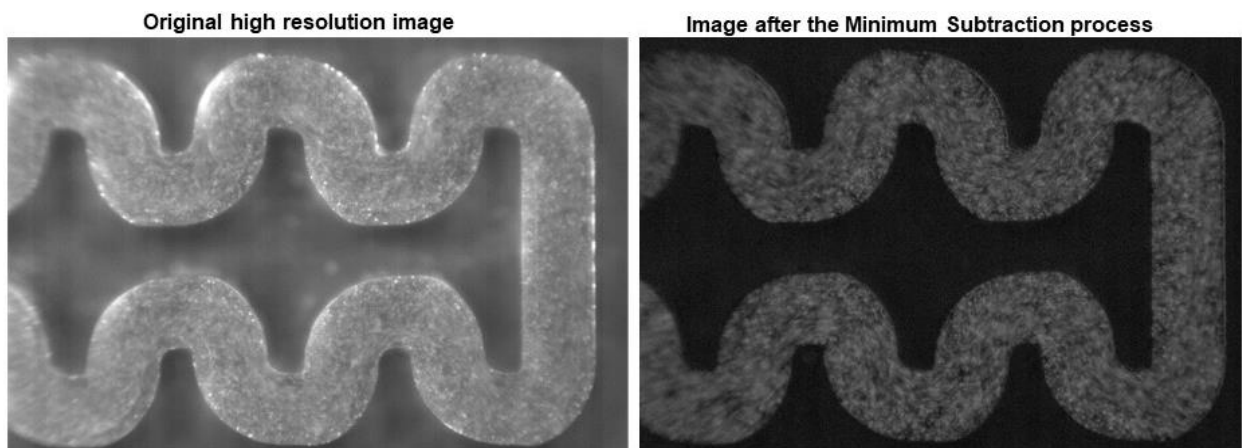


Figure 73: Wavy-sinusoidal serpentine cell, before (left) and after (right) the minimum subtraction.

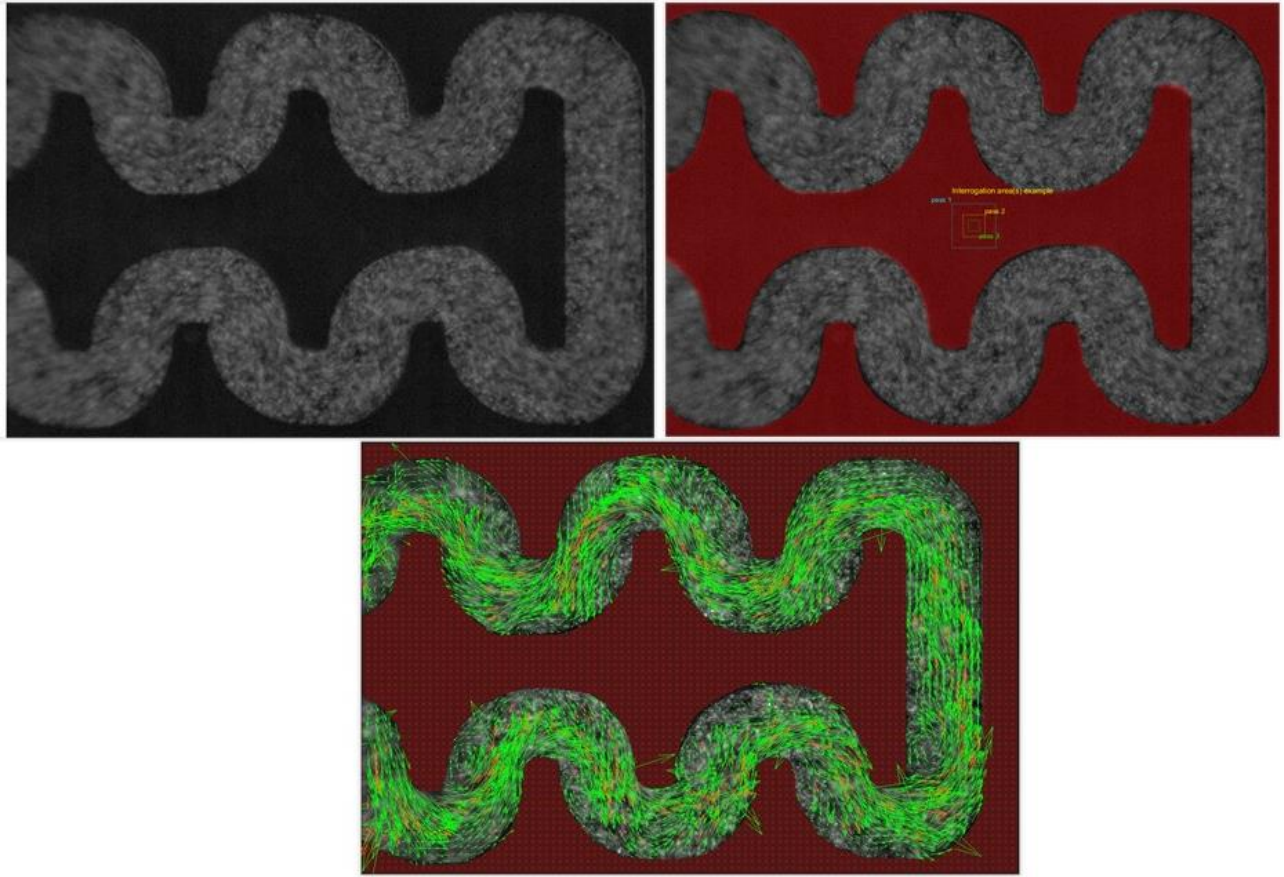


Figure 74: Wavy-sinusoidal serpentine cell raw image (top left), application of the exclusion mask (red area) with evidence of analysis windows (top right), instantaneous velocity vector fields (lower center).

Before to run the *PIVlab* analysis a minimum subtraction process is required to remove possible disturbing elements for the analysis, *e.g.* walls reflections and background from original acquisitions. Examples are given in Figure 73. After this preliminary pre-processing phase, for each configuration all frames minimum subtracted are elaborated by *PIVlab*. To correctly process the images is needed to give some analyses settings; first of all is very useful to draw an exclusion mask, shown in Figure 74, in order to remove all image parts not of interest for the analysis because out of the channel, so as to reduce the processing time. Next, in order to run the cross-correlation algorithm, the analysis windows offset and deformation are settled. In our case for all configurations the algorithm works with three windows size equal to 64×64 pixel, $32 \times$

32 pixel and 16×16 pixel and an overlapping of 50 %. The final sizes origin by a compromise between detail level of analysis and processing time, because reducing sub-windows size the elaboration time increases. For example with three windows of 64, 32, 16 pixel applied to 10.000 frame the processing time is 3 hours, with an added windows of 8×8 pixel the time increases up to 5 hours.

Once the analysis is finished and the instantaneous velocity vector fields in pixel/frame are obtained, Figure 74, before proceeding with the post-processing of results extracted by *PIVlab*, a vector validation algorithm is used to filter vectors and to interpolate missing data. By applying a standard deviation filter of ± 3 pixel/frame the elimination of spurious vectors is ensured without lost important information on fluid motion. The optimal filter values were determined on the base of several tests considering different case of study. The *PIVlab* processing and vector validation times are function of different factors such as number of images, extension of the region of interest, analysis windows size and any further processing options. The following table shows some examples of analysis times by varying the micro-cell geometry and the amount of frames to be process.

Micro-cell	Frame	Windows	Pre-processing settings	Time [hours]
Straight Parallel Channels type-II	6350	64-32-16 pixel	no	3 h
Standard Serpentine	10914	64-32-16 pixel	no	3 h
Wavy-Sin. Serpentine	14111	64-32-16 pixel	no	4 h

Table 23: PIVlab processing and vector validation times for different configurations.

The output data extracted from *PIVlab* are instantaneous vector fields of different parameters including the horizontal, u , and vertical, v , velocity components. The number of instant fields is equal to the number of analyzed frames and all values are expressed in pixel/frame. Each

instantaneous field is a matrix with a number of rows and columns function of the original images resolution. For all the micro-cells and cooling fluids considered, the last phase of data processing consists of calculating the average speed (or magnitude), vorticity and standard deviations starting from the instant u and v values, u_i and v_i , associated with each single frame. Other factors such as vertical profiles are then extracted from the average fields.

A.4 Measured temperatures of outlet fluid and wall

In the following tables the final measured temperatures reached by cooling fluid and wall for all configurations are listed.

Hot Source Temperature: 50 °C	Straight Channel	Parallel Channels type-II	Standard Serpentine Ch.	Wavy-Sin. Serpentine Ch.	Serpentine Ch. with Ribs	Stand. Serpentine with 30 % Glycerin-70 % Water	Stand. Serpentine with 70 % Glycerin-30 % Water
Flow Rate [ml/min]	T [°C]	T [°C]	T [°C]	T [°C]	T [°C]	T [°C]	T [°C]
6	37.4	39.1	38.8	39.4	42.1	33.6	35.7
12	32.9	34.8	34.3	34.7	38.8	30.3	31.7
18	31.2	32.2	31.8	32.4	34.2	28.1	28.8
24	28.4	31.2	29.9	30.4	32.3	26.7	27.8
30	27.8	30.2	28.8	28.7	31.4	25.8	27.2
48	26.3	28.4	26.8	27.3	29.0	25.0	26.4
60	25.3	27.7	26.1	28.1	27.8	24.3	25.7
90	24.3	27.3	26.2	27.7	26.1	23.9	24.8
102	24.0	27.1	25.7	27.3	25.6	23.2	-
120	23.2	26.6	25.3	27.2	25.8	22.9	-
138	23.1	26.1	25.0	26.4	25.3	22.4	-
144	23.3	26.1	24.9	26.3	25.3	22.4	-
150	23.1	25.9	24.9	26.2	25.3	22.8	-
156	23.3	25.4	25.4	-	25.2	22.9	-
168	23.0	25.7	24.9	-	25.3	22.8	-
180	23.0	25.4	24.9	-	-	22.6	-
210	25.6	25.1	24.9	-	-	-	-
216	26.9	25.0	24.8	-	-	-	-
240	-	25.1	-	-	-	-	-

Table 24: Final measured temperatures of outlet fluid for each flow rate [ml/min] and configuration at 50 °C.

Hot Source Temperature: 50 °C	Straight Channel	Parallel Channels type-II	Standard Serpentine Ch.	Wavy-Sin. Serpentine Ch.	Serpentine Ch. with Ribs	Stand. Serpentine with 30 % Glycerin-70 % Water	Stand. Serpentine with 70 % Glycerin-30 % Water
Flow Rate [ml/min]	T [°C]	T [°C]	T [°C]	T [°C]	T [°C]	T [°C]	T [°C]
6	49.7	43.9	44.7	45.3	46.1	48.9	49.7
12	48.1	40.6	42.3	42.4	46.0	49.3	49.7
18	47.5	40.4	42.1	41.9	43.1	49.0	49.5
24	46.8	39.7	42.1	41.7	43.0	48.8	49.5
30	47.1	39.7	42.4	41.0	43.0	48.7	49.1
48	48.3	40.5	42.7	41.9	43.1	48.9	49.1
60	48.6	41.4	42.6	42.3	42.7	48.9	49.1
90	48.4	42.9	43.1	42.1	43.4	49.5	49.2

102	48.3	43.1	43.0	42.9	43.6	49.3	-
120	48.2	43.5	43.4	43.1	43.4	49.4	-
138	48.2	44.0	43.6	42.5	43.8	49.3	-
144	48.1	44.0	43.6	43.0	44.0	49.3	-
150	48.2	44.6	43.9	43.0	43.7	49.4	-
156	48.0	44.4	43.7	-	43.8	49.5	-
168	47.8	45.5	44.1	-	44.3	49.5	-
180	48.1	45.0	44.3	-	-	49.6	-
210	46.9	45.5	44.7	-	-	-	-
216	46.9	45.6	45.3	-	-	-	-
240	-	45.8	-	-	-	-	-

Table 25: Final measured temperatures of wall for each flow rate [ml/min] and configuration at 50 °C.

Hot Source Temperature: 70 °C	Straight Channel	Parallel Channels type-II	Standard Serpentine Ch.	Wavy-Sin. Serpentine Ch.	Serpentine Ch. with Ribs	Stand. Serpentine with 30 % Glycerin-70 % Water	Stand. Serpentine with 70 % Glycerin-30 % Water
Flow Rate [ml/min]	T [°C]	T [°C]	T [°C]	T [°C]	T [°C]	T [°C]	T [°C]
6	50.4	49.6	55.2	56.7	60.6	40.7	43.1
12	38.4	42.9	48.2	49.3	52.1	34.2	36.1
18	37.6	39.9	41.8	43.8	46.7	31.8	33.3
24	32.4	37.6	37.9	39.8	42.3	29.8	31.2
30	33.6	35.7	35.1	37.1	39.4	27.4	30.0
48	28.7	32.2	31.4	36.1	33.8	25.7	27.3
60	28.4	31.5	29.8	33.8	32.8	24.9	26.7
90	26.0	29.3	29.7	31.2	30.1	24.4	26.0
102	26.2	28.7	29.3	30.6	29.4	24.1	-
120	26.1	28.1	28.6	29.9	29.0	24.1	-
138	25.9	27.4	27.8	29.1	28.2	23.8	-
144	25.8	27.2	27.5	29.1	27.6	23.4	-
150	24.9	26.8	27.5	28.8	27.9	23.1	-
156	25.1	26.8	27.5	-	27.7	23.8	-
168	24.9	26.3	27.2	-	27.4	23.3	-
180	24.8	26.4	26.0	-	-	23.3	-
210	29.1	26.2	26.8	-	-	-	-
216	28.6	26.1	27.2	-	-	-	-
240	-	25.8	-	-	-	-	-

Table 26: Final measured temperatures of outlet fluid for each flow rate [ml/min] and configuration at 70 °C.

Hot Source Temperature: 70 °C	Straight Channel	Parallel Channels type-II	Standard Serpentine Ch.	Wavy-Sin. Serpentine Ch.	Serpentine Ch. with Ribs	Stand. Serpentine with 30 % Glycerin-70 % Water	Stand. Serpentine with 70 % Glycerin-30 % Water
Flow Rate [ml/min]	T [°C]	T [°C]	T [°C]	T [°C]	T [°C]	T [°C]	T [°C]
6	68.8	58.2	64.0	63.8	67.6	68.8	69.0
12	68.4	53.3	61.1	59.5	64.4	68.2	68.8
18	67.5	52.4	60.0	57.0	63.4	68.2	68.7
24	67.7	52.2	59.5	56.0	62.2	68.2	68.3
30	66.0	51.8	59.0	55.8	62.2	68.8	68.4
48	66.0	53.3	59.3	56.1	60.9	68.5	68.5
60	65.5	54.4	59.1	60.0	63.7	68.5	68.6
90	65.6	57.9	58.4	57.4	60.1	68.7	68.6
102	65.5	58.1	59.2	57.57	60.3	68.6	-
120	65.8	58.8	59.6	57.5	60.6	68.7	-
138	65.7	59.7	59.2	58.1	60.0	68.7	-
144	65.6	59.8	59.3	58.1	59.8	68.8	-
150	65.7	59.6	59.7	58.07	61.5	68.7	-
156	65.6	60.2	59.7	-	63.5	68.8	-
168	65.8	60.7	59.9	-	64.5	68.8	-
180	66.1	61.4	59.6	-	-	69.2	-
210	65.0	62.3	61.2	-	-	-	-
216	65.0	62.2	61.8	-	-	-	-
240	-	62.7	-	-	-	-	-

Table 27: Final measured temperatures of wall for each flow rate [ml/min] and configuration at 70 °C.

A.5 Extrapolated temperatures of outlet fluid and wall

The final extrapolated temperatures for fluid and wall are shown below, with indication in red of relevant anomalous values provided by analytical model.

Hot Source Temperature: 50 °C	Straight Channel	Parallel Channels type-II	Standard Serpentine Ch.	Wavy-Sin. Serpentine Ch.	Serpentine Ch. with Ribs	Stand. Serpentine with 30 % Glycerin-70 % Water	Stand. Serpentine with 70 % Glycerin-30 % Water
Flow Rate [ml/min]	T [°C]	T [°C]	T [°C]	T [°C]	T [°C]	T [°C]	T [°C]
6	37.4	38.5	38.8	39.4	42.1	33.6	35.7
12	32.8	34.7	34.1	34.7	38.7	29.8	30.4
18	31.1	32.0	31.4	32.3	33.7	27.5	27.6
24	28.5	30.9	29.9	30.5	32.1	25.9	27.1
30	27.8	29.9	28.9	28.6	31.4	24.9	25.7
48	26.1	28.4	26.8	27.2	29.0	24.6	25.1
60	25.2	27.6	26.1	28.1	27.8	23.9	24.2
90	24.3	27.2	26.1	27.6	26.1	23.7	23.5
102	23.8	26.9	25.8	27.3	25.8	23.1	-
120	23.1	26.6	25.2	27.2	25.8	22.7	-
138	23.0	26.1	25.1	26.4	25.3	22.2	-
144	23.2	26.0	25.1	26.3	25.3	22.2	-
150	23.0	25.9	25.1	26.2	25.2	22.8	-
156	23.2	25.6	24.7	-	25.1	22.5	-
168	22.9	25.6	24.8	-	25.1	22.4	-
180	22.9	25.4	24.8	-	-	22.1	-
210	25.6	25.1	24.7	-	-	-	-
216	26.9	25.0	24.8	-	-	-	-
240	-	25.1	-	-	-	-	-

Table 28: Final extrapolated temperatures of outlet fluid for each flow rate [ml/min] and configuration at 50 °C, with indication in red of anomalous values provided by analytical model.

Hot Source Temperature: 50 °C	Straight Channel	Parallel Channels type-II	Standard Serpentine Ch.	Wavy-Sin. Serpentine Ch.	Serpentine Ch. with Ribs	Stand. Serpentine with 30 % Glycerin-70 % Water	Stand. Serpentine with 70 % Glycerin-30 % Water
Flow Rate [ml/min]	T [°C]	T [°C]	T [°C]	T [°C]	T [°C]	T [°C]	T [°C]
6	49.4	43.5	44.5	45.0	46.1	48.9	49.7
12	48.0	40.4	41.0	41.4	45.7	49.3	49.7
18	47.3	39.5	40.9	40.6	42.2	48.6	49.2
24	46.6	38.5	40.4	40.3	42.2	47.0	47.2
30	46.5	37.7	40.8	39.3	41.9	46.3	47.5
48	47.5	36.9	40.3	39.5	42.0	45.8	47.2
60	42.7	36.0	39.5	41.3	41.8	47.2	47.3
90	40.8	35.7	41.3	41.2	42.0	46.6	44.3

102	40.7	35.4	41.0	40.9	41.9	42.9	-
120	40.6	35.0	40.8	40.4	41.5	42.2	-
138	40.5	34.5	40.9	39.5	41.1	41.6	-
144	40.5	34.0	40.5	39.2	41.1	41.5	-
150	40.4	32.6	40.6	39.2	41.0	41.7	-
156	40.4	32.0	40.8	-	40.9	42.2	-
168	40.6	31.9	40.8	-	39.5	42.1	-
180	40.5	29.1	40.0	-	-	41.3	-
210	38.4	25.9	39.3	-	-	-	-
216	36.2	24.9	37.6	-	-	-	-
240	-	23.0	-	-	-	-	-

Table 29: Final extrapolated temperatures of wall for each flow rate [ml/min] and configuration at 50 °C, with indication in red of anomalous values provided by analytical model.

Hot Source Temperature: 70 °C	Straight Channel	Parallel Channels type-II	Standard Serpentine Ch.	Wavy-Sin. Serpentine Ch.	Serpentine Ch. with Ribs	Stand. Serpentine with 30 % Glycerin-70 % Water	Stand. Serpentine with 70 % Glycerin-30 % Water
Flow Rate [ml/min]	T [°C]	T [°C]	T [°C]	T [°C]	T [°C]	T [°C]	T [°C]
6	50.4	50.2	55.6	56.0	60.5	40.7	43.0
12	39.4	42.5	48.2	49.3	52.3	33.3	34.3
18	38.4	39.3	41.5	43.6	46.6	31.3	32.0
24	33.2	37.3	38.2	39.7	42.4	29.2	29.7
30	34.5	35.2	35.3	37.2	39.4	26.8	29.1
48	29.2	31.8	31.5	36.0	33.8	25.2	26.3
60	28.5	31.1	29.9	33.7	32.8	24.3	25.7
90	26.4	29.1	29.7	31.1	30.1	23.8	25.5
102	26.2	28.3	29.1	30.5	29.4	23.6	-
120	27.0	27.8	28.5	29.8	28.9	23.9	-
138	25.8	27.1	27.7	29.1	28.3	23.5	-
144	25.7	27.0	27.4	29.1	27.6	23.0	-
150	24.9	26.3	27.4	28.7	27.9	22.6	-
156	25.2	26.2	27.3	-	27.4	23.4	-
168	24.9	26.2	27.1	-	27.3	22.9	-
180	24.8	26.2	27.0	-	-	22.8	-
210	26.6	26.1	27.1	-	-	-	-
216	28.1	26.0	27.0	-	-	-	-
240	-	25.7	-	-	-	-	-

Table 30: Final extrapolated temperatures of outlet fluid for each flow rate [ml/min] and configuration at 70 °C, with indication in red of anomalous values provided by analytical model.

Hot Source Temperature: 70 °C	Straight Channel	Parallel Channels type-II	Standard Serpentine Ch.	Wavy-Sin. Serpentine Ch.	Serpentine Ch. with Ribs	Stand. Serpentine with 30 % Glycerin-70 % Water	Stand. Serpentine with 70 % Glycerin-30 % Water
Flow Rate [ml/min]	τ [°C]	τ [°C]	τ [°C]	τ [°C]	τ [°C]	τ [°C]	τ [°C]
6	69.8	58.1	63.9	63.8	67.5	68.6	69.0
12	68.6	52.9	61.3	59.5	64.4	68.3	68.7
18	67.8	51.5	60.0	56.9	63.5	68.5	68.8
24	64.9	50.3	59.4	55.6	62.5	68.2	68.3
30	65.8	48.8	58.8	55.1	62.0	68.6	68.4
48	64.6	47.7	58.2	54.9	60.7	68.5	68.5
60	64.3	45.5	57.6	55.5	59.8	68.5	68.6
90	64.5	45.0	56.6	54.8	59.3	68.6	68.3
102	62.6	44.7	56.6	54.6	58.9	68.5	-
120	64.2	44.2	56.1	53.7	58.0	68.4	-
138	63.1	43.8	54.7	53.2	56.7	68.6	-
144	61.7	43.4	54.6	53.1	56.5	68.6	-
150	62.7	41.7	54.5	53.1	55.3	68.4	-
156	61.9	40.8	54.4	-	54.8	68.6	-
168	56.9	40.4	54.2	-	54.4	68.5	-
180	61.5	40.2	53.7	-	-	68.5	-
210	63.8	40.1	53.6	-	-	-	-
216	61.6	40.0	53.1	-	-	-	-
240	-	40.0	-	-	-	-	-

Table 31: Final extrapolated temperatures of wall for each flow rate [ml/min] and configuration at 70 °C, with indication in red of anomalous values provided by analytical model.

A.6 Prandtl Number

Since the *Nusselt number* is dependent on both *Reynolds* and *Prandtl numbers*, in Figure 75, Figure 76, Figure 77 and Figure 78 the *Nusselt number* as a function of *Prandtl number* for a hot source temperature of 50 °C and 70 °C are also shown together with the correlation obtained in case of a laminar flow over a flat isothermal plate [2]:

$$Nu = 0.3 \cdot Re^{\frac{1}{2}} \cdot Pr^{\frac{1}{3}} \quad \text{with } 0.6 \leq Pr \leq 50 \quad (56)$$

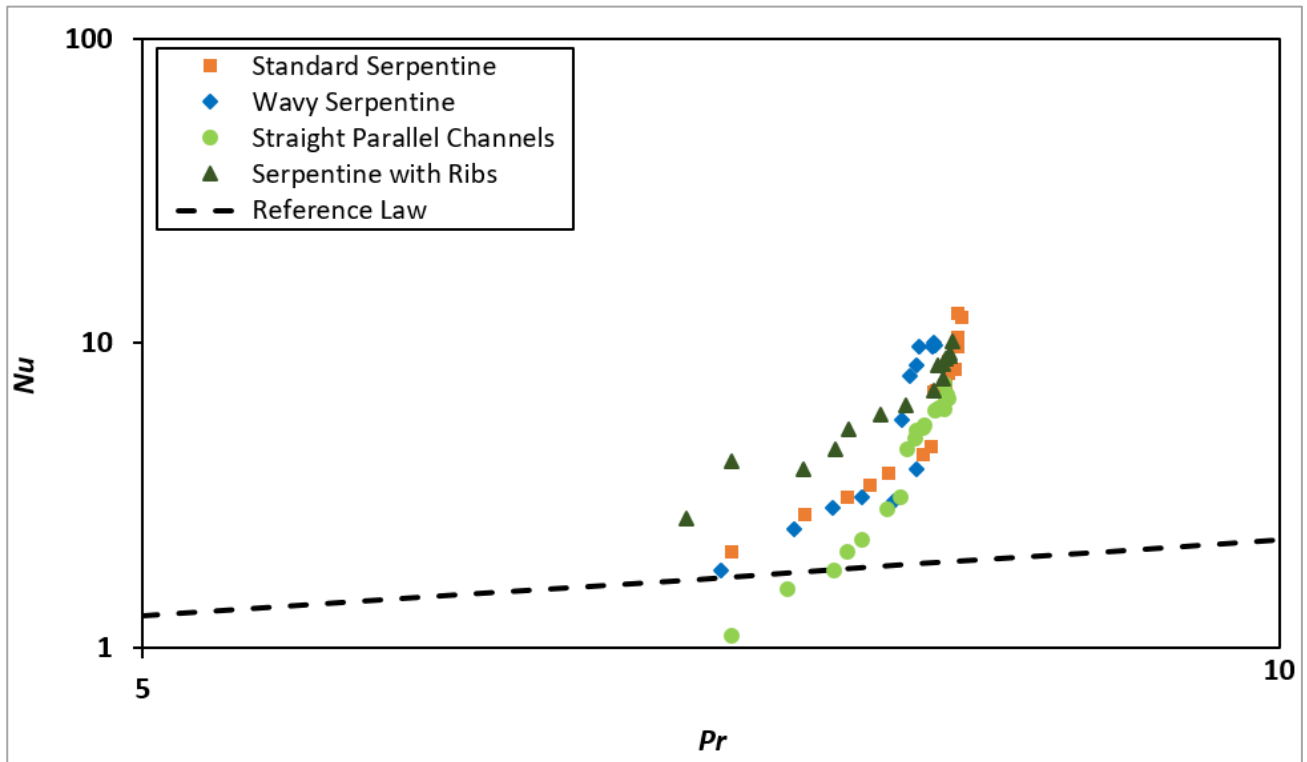


Figure 75: Comparison of the average Nusselt numbers as a function of the Prandtl number obtained for the four micro-cells tested with water together with the reference law for a laminar flow over a flat isothermal plate [2]. Hot source temperature equal to 50 °C.

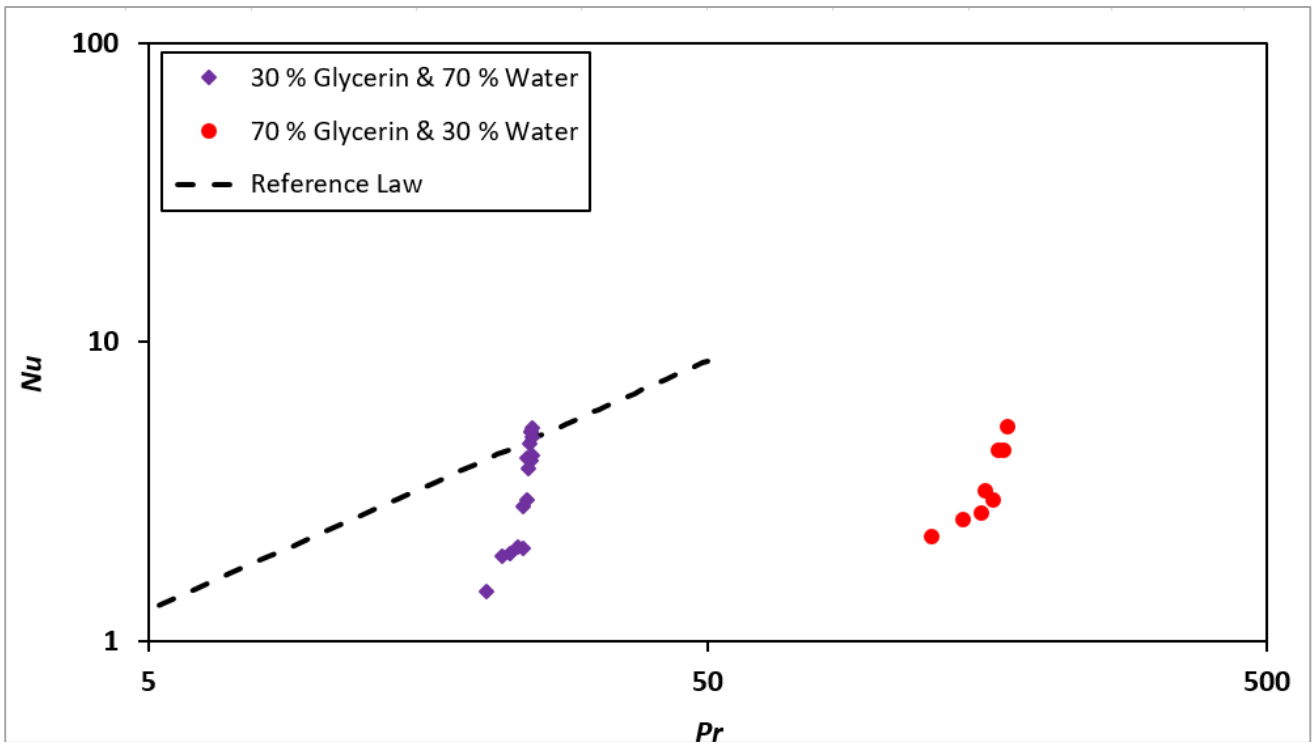


Figure 76: Comparison of the average Nusselt numbers as a function of the Prandtl number obtained for the two micro-cells tested with water/glycerin solutions together with the reference law for a laminar flow over a flat isothermal plate [2]. Hot source temperature equal to 50 °C.

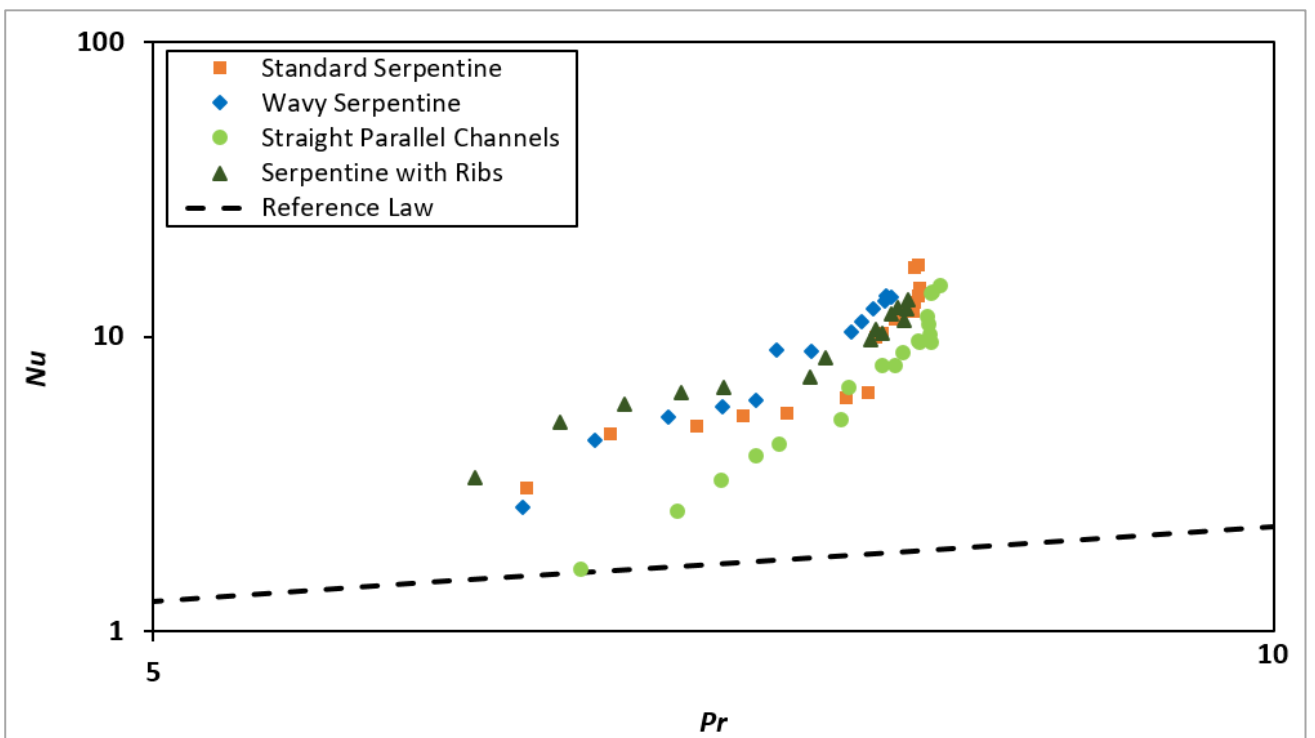


Figure 77: Comparison of the average Nusselt numbers as a function of the Prandtl number obtained for the four micro-cells tested with water together with the reference law for a laminar flow over a flat isothermal plate [2]. Hot source temperature equal to 70 °C.

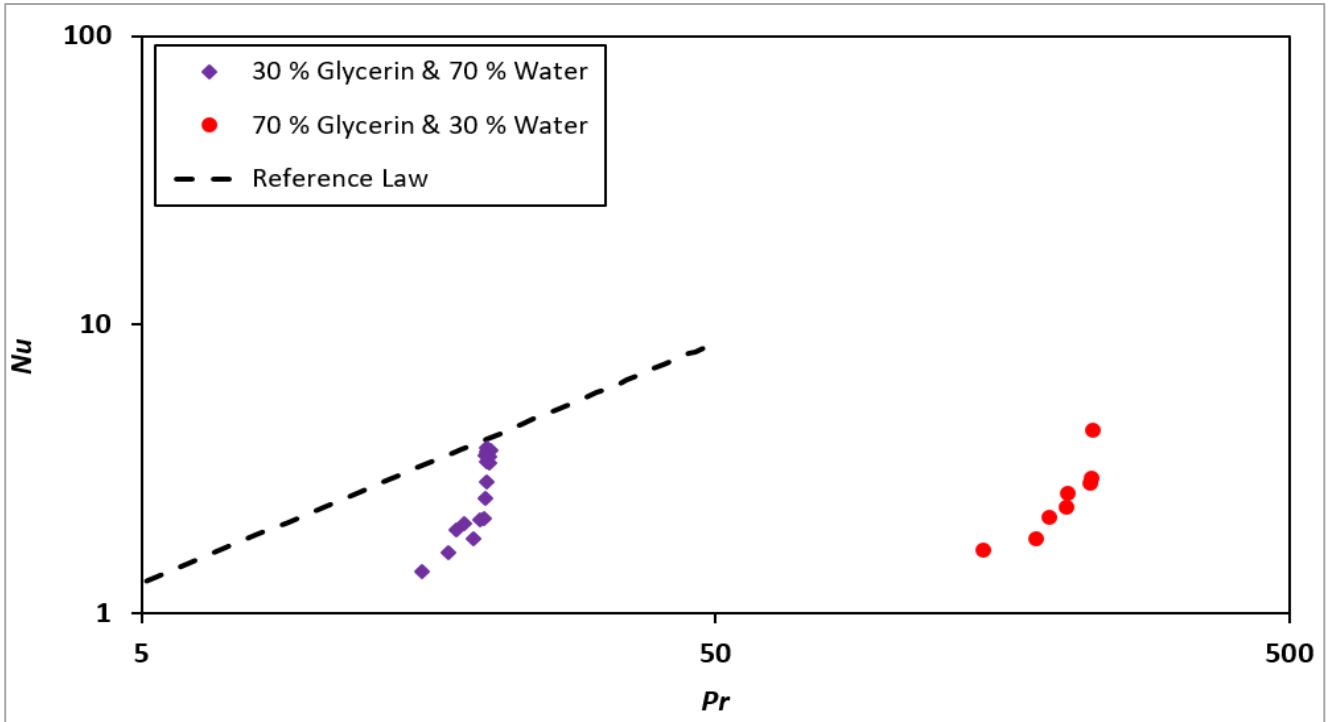


Figure 78: Comparison of the average Nusselt numbers as a function of the Prandtl number obtained for the two micro-cells tested with water/glycerin solutions together with the reference law for a laminar flow over a flat isothermal plate [2]. Hot source temperature equal to 70 °C.

The trends shown in Figure 75, Figure 76, Figure 77 and Figure 78 are far from *Nusselt* values encountered for a flat plate (this is reported in dotted line), presumably also in this case, as for *Nusselt-Reynolds* curves, the main cause could be a non-classical channel shape that induces turbulent motion also in laminar conditions. However, with regards to cells tested with water and to a source temperature of 70 °C (Figure 77), it is possible to notice a compliance between the serpentine configurations trend and the reference law. In fact, in a range of *Prandtl number* from 6.5 to 7 for all cells with serpentine *Nusselt number* increases with *Prandtl number* with a linear-law with angular coefficient close to the reference law. Also in case of water/glycerin solutions, for both hot source temperatures (Figure 76 and Figure 78) is possible to observe a fair agreement between trends for the lowest values of *Nusselt number*. On the other hand, for all configurations and temperature conditions, a net change in slope of curves is noticeable, whose reduces the differences among the tested geometries in term of trend and values of *Prandtl number* in case of cells tested with water.

A.7 Efficiency parameters

Two other performance factors have been computed, whose formulation is in agreement with the correlation proposed in several studies of micro heat exchangers [58], [59]:

$$\varepsilon' = \frac{Nu}{f^{\frac{1}{3}}} \quad (57)$$

$$\varepsilon'' = \frac{Nu/Nu_L}{(f/f_L)} \quad (58)$$

where Nu_L is the exact solution for the *Nusselt number* obtained for a laminar flow over a flat isothermal plate [2]:

$$Nu = 0.3 \cdot Re^{\frac{1}{2}} \cdot Pr^{\frac{1}{3}} \quad (59)$$

and f_L is the exact solution for the *Fanning friction factor* also obtained in laminar conditions [46]:

$$f_L = \frac{64}{Re} \quad (60)$$

The main results are confirmed also by these two other performance factors, ε' and ε'' , obtained according to definition given above as reported in Figure 79, Figure 80, Figure 81, Figure 82. Overall, for both hot source temperatures, there is a remarkable agreement between the relevance of each cell among the different evaluations of the cell efficiency (ε (section 2), ε' and ε''), thus confirming improvements when using the standard serpentine. For example, this can

be quantified from Figure 81 around 50 % in comparison to the wavy serpentine and even more in comparison to the straight configuration. The different behaviors of efficiency parameters ε (section 2) and ε' as functions of *Reynolds number*, in comparison to ε'' can be explained as follows. The increases of the first two depend on the simultaneous increase of *Nusselt number* and decrease of *Fanning factor* with *Reynolds number*. On the other hand, ε'' is decreasing because the measured *Fanning factor* decreases much slowly than the laminar prediction.

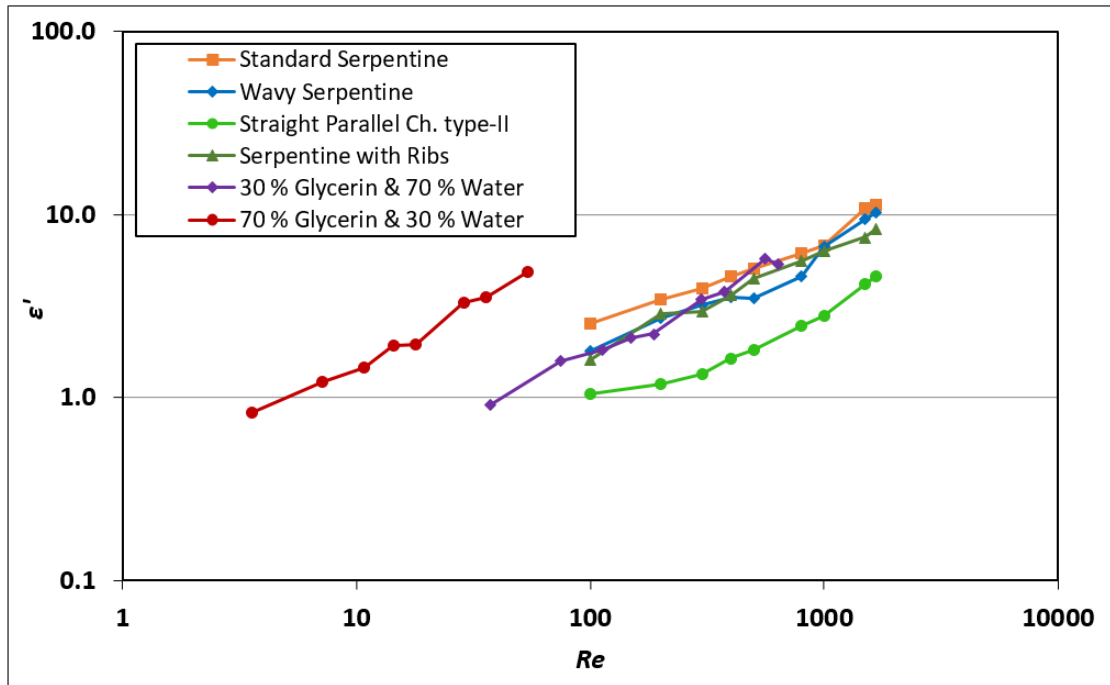


Figure 79: Comparison of the efficiency parameters ε' as a function of *Reynolds number* for the tested cells at 50 °C.

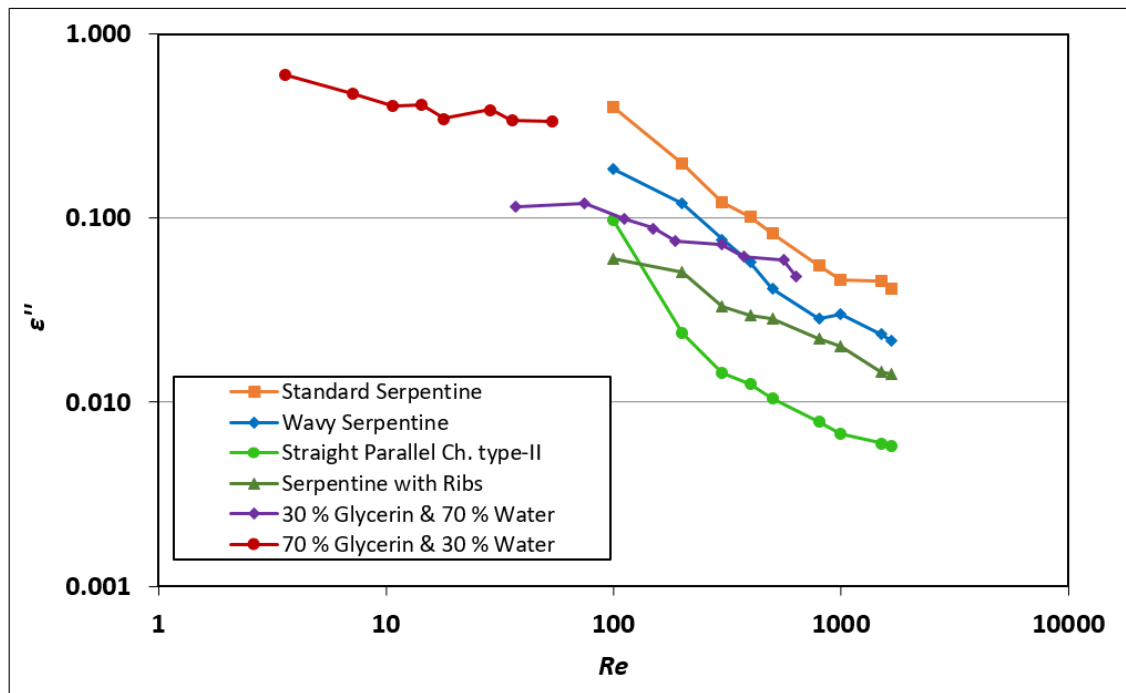


Figure 80: Comparison of the efficiency parameters ε'' as a function of Reynolds number for the tested cells at 50 °C.

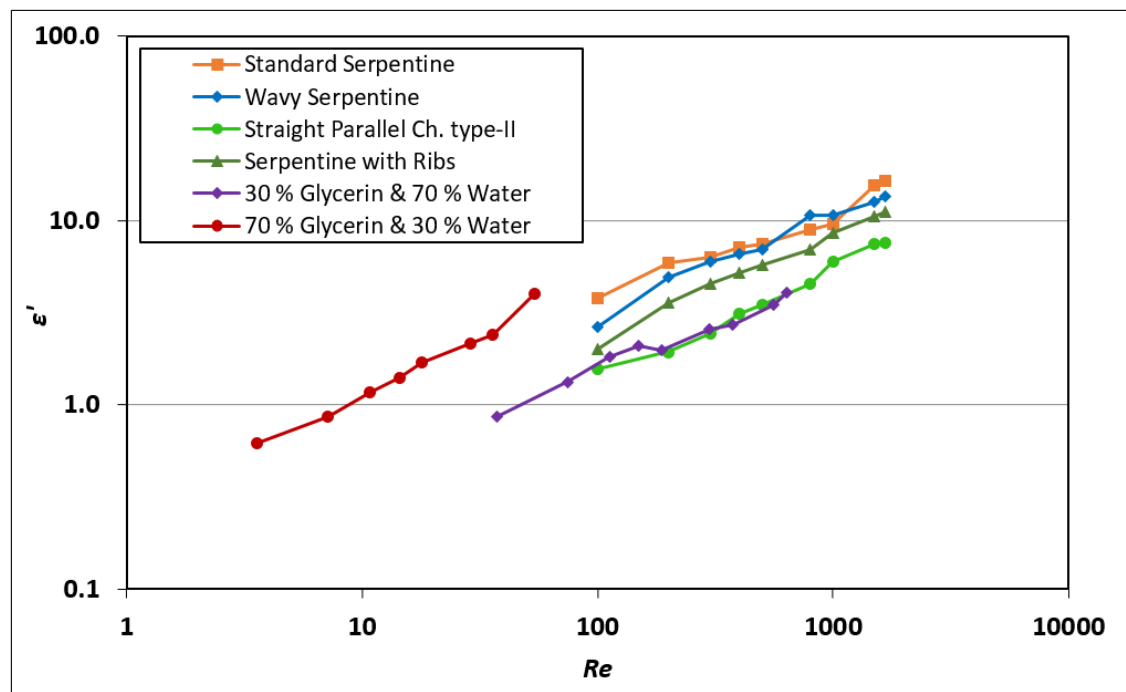


Figure 81: Comparison of the efficiency parameters ε' as a function of Reynolds number for the tested cells at 70 °C.

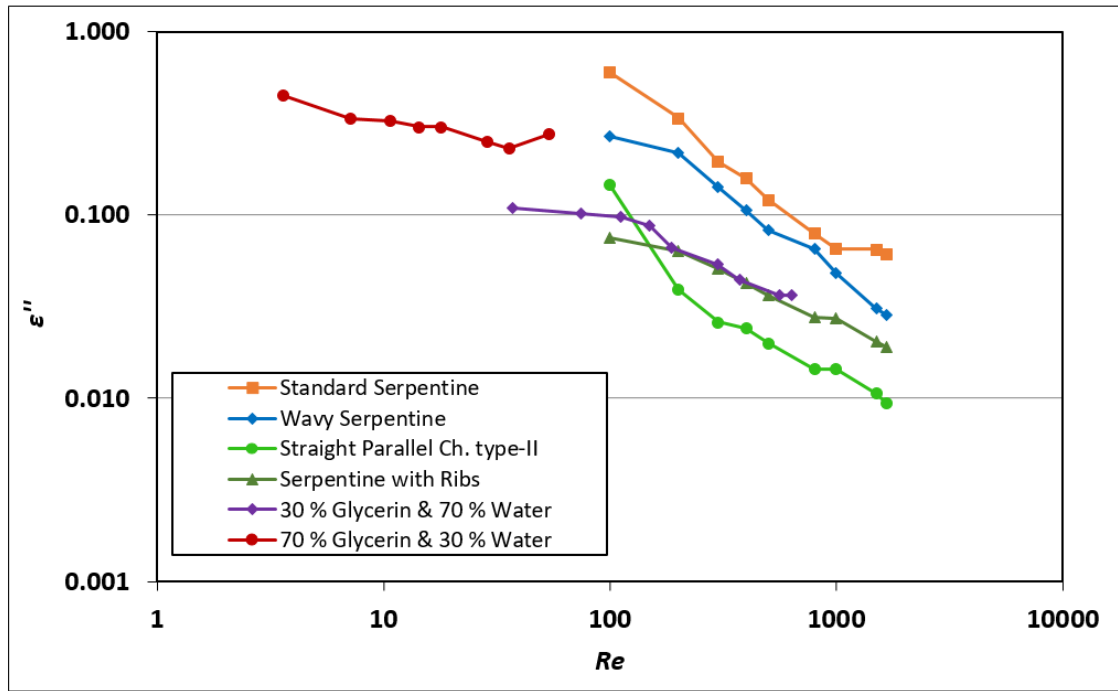


Figure 82: Comparison of the efficiency parameters ε'' as a function of Reynolds number for the tested cells at 70 °C.

Acknowledgements

Firstly, I would like to express my gratitude to my advisor Prof. Giovanni Paolo Romano for the continuous support of my Ph.D study and related research, for his motivation and to have been a reference point in all these years spent together.

Besides my advisor, I would like to thank Prof. Christian J. Kähler, Prof. Gianfranco Caruso and Prof. Alberto Boschetto for their precious support, discussions and suggestions to this research work. My sincere thanks also goes to Domenico Pietrogiacomì, Maximo Orlando Capponi, Antonello Binni, and Alessandro Caterina for the help in cell manufacturing and especially because without their precious support it would not have been possible to conduct this research.

Lastly, the greatest thanks goes to my co-workers Manuela Sisti, Jais Mohamed, Aurora Sisti, Oana Lorena Ciubotaro, Camilla Cecchini and Alireza Hassani Sorkhani. For the collaboration in experimental tests, but above all for the beautiful memories that have made these three years a unique experience that I will carry with me forever.

References

- [1] M. Eshani, Y. Gao, E.S. Gay, A. Emadi, Modern Electric, Hybrid Electric, and Fuel Cell Vehicles, third ed., CRC Press, Boca Raton, 2005, pp.98.
- [2] M. Mahmoud, Engineering Thermofluids-Thermodynamics, Fluid Mechanics and Heat Transfer, first ed., Springer, Berlin, 2005, pp. 518-520.
- [3] S.G. Kandlikar, S. Colin, Y. Peles, S. Garimella, R.F. Pease, J.J. Brandner, D.B. Tuckerman, Heat Transfer in Microchannels 2012 Status and Research Needs, Journal of Heat Transfer 135 (2013) 091001.
- [4] S.G. Kandlikar, History, Advances, and Challenges in Liquid Flow and Flow Boiling Heat Transfer in Microchannels: A Critical Review, Journal of Heat Transfer 134 (2012) 034001-034015.
- [5] A.F. Al-Neama, N. Kapur, J. Summers, H.M. Thompson, An experimental and numerical investigation of the use of liquid flow in serpentine microchannels for microelectronics cooling, Applied Thermal Engineering 116 (2017) 709-723.
- [6] Y. Asako, H. Nakamura, M. Faghri, Heat transfer and pressure drop characteristics in a corrugated duct with rounded corners, International Journal of Heat and Mass Transfer 31 (1988)1237-1245.
- [7] F. Mayinger, J. Klas, Compact Heat Exchangers, Lehrstuhl A für Thermodynamik 21 (1993) 35-46.
- [8] G. Gaiser, V. Kottke, Flow phenomena and local heat and mass transfer in corrugated passages, Chemical and Engineering Technology 12 (1989) 400-405.
- [9] C.V. Herman, F. Mayinger, D.P. Sekulic, Experimental verification of oscillatory phenomena in heat transfer in a communicating channels geometry, Experimental Heat Transfer, Fluid Mechanics and Thermodynamics 1 (1991) 904-911.
- [10] R. Fehle, J. Klas, F. Mayinger, Investigation of local heat transfer in compact heat exchangers by holographic interferometry, Experimental Thermal and Fluid Science 10 (1995) 181-191.
- [11] E. Vásquez-Alvarez, F. T. Degasperri, L. G. Morita, M. R. Gongora-Rubio, R. Giudici, Development of a micro-heat exchanger with stacked plates using LTCC technology, Brazilian Journal of Chemical Engineering 27 (2010) 483-497.
- [12] N.R. Rosaguti, D.F. Fletcher, B.S. Haynes, Laminar flow and heat transfer in a periodic serpentine channel, Chemical and Engineering Technology 28 (2005) 353-361.

- [13] N. Nivedita, P. Ligrani, I. Papautsky, Dean Flow Dynamics in Low-Aspect Ratio Spiral Microchannels, *Scientific Reports* 7 (2017) 1-10.
- [14] Y. Sui, P.S. Lee, C.J. Teo, An experimental study of flow friction and heat transfer in wavy microchannels with rectangular cross section, *International Journal of Thermal Sciences* 50 (2011) 2473-2482.
- [15] L. Lin, J. Zhao, G. Lu, X.D. Wang, W.M. Yan, Heat transfer enhancement in microchannel heat sink by wavy channel with changing wave length/amplitude, *International Journal of Thermal Sciences* 118 (2017) 423-434.
- [16] G. Xia, Z. Chen, L. Cheng, D. Ma, Y. Zhai, Y. Yang, Micro-PIV visualization and numerical simulation of flow and heat transfer in three micro pin-fin heat sinks, *International Journal of Thermal Sciences* 119 (2017) 9-23.
- [17] X. Hao, B. Peng, G. Xie, Y. Chen, Thermal Analysis and Experimental Validation of Laminar Heat Transfer and Pressure Drop in Serpentine Channel Heat Sinks for Electronic Cooling, *Journal of Electronic Packaging* 136 (2014) 031009.
- [18] F.P. Incropera, D.P. Dewitt, T.L. Bergman, A.S. Lavine, *Fundamentals of Heat and Mass Transfer*, sixth ed., John Wiley & Sons, USA, 2006, pp. 7-8.
- [19] M. Bahrami, Lecture note, Course of ENSC388 Engineering Thermodynamics and Heat Transfer, LAEC-Laboratory for alternative energy conversion, Simon Fraser University, Canada (2011).
- [20] W.M. Abed, R.D. Whalley, D.J.C. Dennis, R.J. Poole, Numerical and experimental investigation of heat transfer and fluid flow characteristics in a micro-scale serpentine channel, *International Journal of Heat and Mass Transfer* 88 (2015) 790-802.
- [21] Y. Xing, T. Zhi, L. Haiwang, T. Yitu, Experimental investigation of surface roughness effects on flow behavior and heat transfer characteristics for circular microchannels, *Chinese Journal of Aeronautics* 29 (2016) 1575-1581.
- [22] Y.A. Cengel, *Introduction To Thermodynamics And Heat Transfer*, third ed., McGraw-Hill, 2009, pp. 553.
- [23] http://www.met.reading.ac.uk/~sws04cdw/viscosity_calc.html;
<https://link.springer.com/article/10.1007/s00348-018-2527-y>
- [24] Z. Dai, D.F. Fletcher, B.S. Haynes, Impact of tortuous geometry on laminar flow heat transfer in microchannels, *International Journal of Heat and Mass Transfer* 83 (2015) 382-398.

- [25] S. Mahmud, R.A. Fraser, The second law analysis in fundamental convective heat transfer problems, *International Journal of Thermal Sciences* 42 (2001) 177-186.
- [26] A. Hashiehbafe, G.P. Romano, An experimental investigation on mixing enhancements in non-circular sharp-edged nozzles using the entropy production concept, *Journal of Turbulence* 15 (2014) 411-428.
- [27] L. Gargaro, Indagine sperimentale del flusso in un sistema di micro canali mediante la tecnica microPIV, 2016.
- [28] T.M. Liou, C.S. Wang, H. Wang, Nusselt number and friction factor correlations for laminar flow in parallelogram serpentine micro heat exchangers, *Applied Thermal Engineering* 143 (2018) 871-882.
- [29] A.D. Rajapakse, A.M. Gole, P. L. Wilson, Electromagnetic Transients Simulation Models for Accurate Representation of Switching Losses and Thermal Performance in Power Electronic Systems, *IEEE Transactions on Power Delivery* 20 (2005) 319-327.
- [30] E.G. Colgan, B. Furman, M. Gaynes, W.S. Graham, N.C. La Bianca, J.H. Magerlein, R.J. Polastre, M.B. Rothwell, R.J. Bezama, R. Choudhary, K.C. Marston, H. Toy, J. Wakil, J.A. Zitz, R.R. Schmidt, A Practical Implementation of Silicon Microchannel Coolers for High Power Chips, *IEEE Transactions on Components and Packaging Technologies* 30 (2007) 218-225.
- [31] <https://it.omega.com/prodinfo/termocoppie.html>
- [32] https://de-de.wika.de/upload/DS_IN0023_it_it_54291.pdf
- [33] P. Lee, S.V. Garimella, D. Liu, Investigation of heat transfer in rectangular microchannels, *International Journal of Heat and Mass Transfer* 48 (2005) 1688-1704.
- [34] G.L. Morini, Y. Yang, Guidelines for the Determination of Single-Phase Forced Convection Coefficients in Microchannels, *Journal of Heat Transfer* 135 (2013) 101004.
- [35] A.A. Imran, N.S. Mahmouda, H.M. Jaffal, Numerical and experimental investigation of heat transfer in liquid cooling serpentine mini-channel heat sink with different new configuration models, *Thermal Science and Engineering Progress* 6 (2018) 128-139.
- [36] T.L. Brown, H.E. LeMay Jr., B.E. Bursten, C.J. Murphy, *Chemistry: the central science*, second ed., EdiSES, 2014, pp. 542-548.
- [37] <http://fisicatecnica.altervista.org/risorse/propfluidi.htm>

- [38] R.S. Subramanian, Heat transfer in Flow Through Conduits, Clarkson University Project, Department of Chemical and Biomolecular Engineering, Potsdam, NY, 2015.
- [39] E.N. Sieder, G.E. Tate, Heat Transfer and Pressure Drop of Liquids in Tubes, *Ind. Eng. Chem.* 28 (1936) 1429-1435.
- [40] A. Dermanis, Adjustment of Observations and Estimation Theory, Volume 1, Edition Ziti, 1986.
- [41] P.S. Lee, S.V. Garimella, D. Liu, Investigation of heat transfer in rectangular microchannels, *International Journal of Heat and Mass Transfer* 48 (2005) 1688-1704.
- [42] P.S. Lee, S.V. Garimella, Thermally developing flow and heat transfer in rectangular microchannels of different aspect ratios, *International Journal of Heat and Mass Transfer* 49 (2006) 3060-3067.
- [43] J.M. Yin, C.W. Bullard, P.S. Hrnjak, Pressure Drop Measurements in Microchannel Heat Exchanger, *Heat Transfer Engineering* 23 (2002) 101080.
- [44] W. Qu, I. Mudawar, Experimental and numerical study of pressure drop and heat transfer in a single-phase micro-channel heat sink, *International Journal of Heat and Mass Transfer* 45 (2002) 2549–2565.
- [45] S. Halelfadl, A.M. Adham, N. Mohd-Ghazali, T. Maré, P. Estellé, R. Ahmad, Optimization of thermal performances and pressure drop of rectangular microchannel heat sink using aqueous carbon nanotubes based nanofluid, *Applied Thermal Engineering* 62 (2014) 492-499.
- [46] J.T. Fanning, Hydraulic Engineering and Manual for Water Supply Engineers , third ed., D. Van Nostrand, New York, 1882.
- [47] M. Raffel, C.E. Willert, F. Scarano, C.J. Kähler, S.T. Wereley, J. Kompenhans, Particle Image Velocimetry A Practical Guide, third ed., Springer, 2018.
- [48] K.S. Breuer, Microscale Diagnostic Techniques, first ed., Springer, 2005.
- [49] A. Schröder, E. Willert, Particle Image Velocimetry-New developments and recent applications, Springer, 2008.
- [50] K. Jiao, B. Zhou, P. Quan, Liquid water transport in straight micro-parallel-channels with manifolds for PEM fuel cell cathode, *Journal of Power Sources* 157 (2006) 226–243.

- [51] M. Hirota, H. Fujita, H. Nakayama, A. Syuhada, Heat (mass) transfer characteristics in serpentine flow passages with a sharp turn, *Memoirs of the School of Engineering, Nagoya University* 52 (2000) 1-52.
- [52] K. Tatsumi, Y. Takeda, K. Suga, K. Nakabe, Turbulence characteristics and mixing performances of viscoelastic fluid flow in a serpentine microchannel, *Journal of Physics: Conference Series* 318 (2011) 092020.
- [53] D. Tarlet, Y. Fan, S. Roux, L. Luo, Entropy generation analysis of a mini heat exchanger for heat transfer intensification, *Experimental Thermal and Fluid Science* 53 (2014) 119-126.
- [54] <https://www.solver.com/excel-solver-algorithms-and-methods-used>
- [55] M.M. Mielnik, R.L. Saeiran, Micro particle Image velocimetry – an overview, *International Workshop on Size Effects in Microfluidics and Micro Heat Transfer – Fundamental and Practical Aspects, Kielce, Poland* (2004) 83-90.
- [56] C.J. Kähler, T. Astarita, P.P. Vlachos, J. Sakakibara, R. Hain, S. Discetti, R. La Foy, C. Cierpka, Main results of the 4th International PIV Challenge, *Experiments in Fluids* (2016) 57:97.
- [57] W. Thielicke, E.J. Stamhuis, PIVlab – Towards User-friendly, Affordable and Accurate Digital Particle Image Velocimetry in MATLAB, *Journal of Open Research Software* 2 (2014).
- [58] P. Promvonge, Thermal augmentation in circular tube with twisted tape and wire coil turbulators, *Energy Conversion and Management* 49 (2008) 2949–2955.
- [59] A. Kumar, M. Kumar, S. Chamoli, Comparative study for thermal-hydraulic performance of circular tube with inserts, *Alexandria Engineering Journal* 55 (2016), 343–349.